Characterization of the new DiRICH readout chain for the CBM/HADES RICH detectors

Dissertation
zur Erlangung des akademischen Grades eines
Doktors der Naturwissenschaften (Dr. rer. nat.)

der Fakultät Mathematik und Naturwissenschaften
Fachgruppe Physik
der Bergischen Universität Wuppertal

vorgelegt von
Vivek Patel
Wuppertal

Defended
April, 2024

1. Gutachter:
Prof. Dr. Karl-Heinz Kampert
Bergische Universität Wuppertal

2. Gutachter
Prof. Dr. Frank Goldenbaum
Bergische Universität Wuppertal
& Forschungszentrum Jülich

Contents

List of Figures

List of Tables

Abstract

The Gesellschaft für Schwerionenforschung(GSI) is the largest facility studying heavy ion collisions in Western Europe. It has many experiments for studying nuclear matter. One of these experiments is the High Acceptance Di-Lepton Spectrometer (HADES), which studies the physics of rare probes produced in heavy ion collision. This thesis will explore the instrumentation project for HADES and its upgrade. Lepton detection in HADES is done using the Ring Imaging Cherenkov Counter (RICH). It uses the phenomenon of Cherenkov radiation to identify and detect electrons and positrons and separate pions. HADES has been operational since the early 2000s and is now upgraded using Multi-Anode Photomultiplier Tubes (MAPMT) and dedicated readout electronics specifically designed to focus on the physics goals of all future experiments of GSI. This new readout concept is called DiRICH, an FPGA-based readout that enables excellent time resolution. This thesis will discuss the performance tests done on the photon sensors and the readout electronics. The tests ensured the quality control of the sensors and readout electronics during the delivery phase and their eligibility to be used in the final upgrade of the HADES-RICH detector.

1 Introduction

This chapter provides an overview of the Quark Gluon Plasma (QGP), including its history, experimental discovery, and significance in particle physics and astroparticle physics. A general outline of the thesis is then presented.

1.1 What is a QGP?

Nuclear Science is the study of the physics of subatomic particles. It developed in the later half of the 19th century and is considered one of the more recent branches. The timeline below highlights several significant events in the history of nuclear science [Wik23].

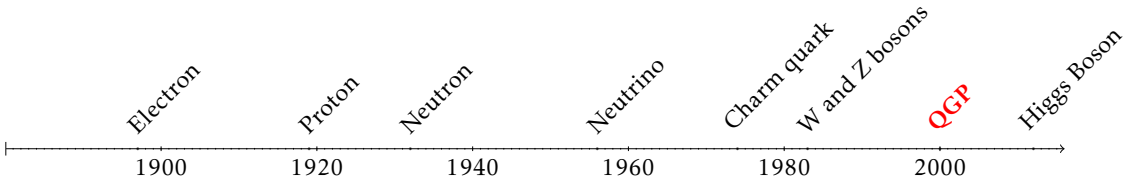

One of the latest discoveries in nuclear science is the Quark-Gluon Plasma (QGP). Heavy Ion Collisions are the primary methods for investigating the QGP phase, and various experimental facilities throughout the world are now altering their accelerators for this purpose. Understanding several phenomena, such as neutron star density and the history of the cosmos following the Big Bang, particularly during the first few seconds, is impossible without QGP [Sin13]. To explain the significance of the QGP in the evolution of the universe following the Big bang, one must comprehend the nuclear phase diagram [Hor17] (Fig. 1.1). The nuclear phase diagram is comparable to the phase diagram of water, which illustrates how the state of water changes in response to variations in the temperature and pressure. At a critical point on the phase diagram, the physical properties of water undergo a significant change.

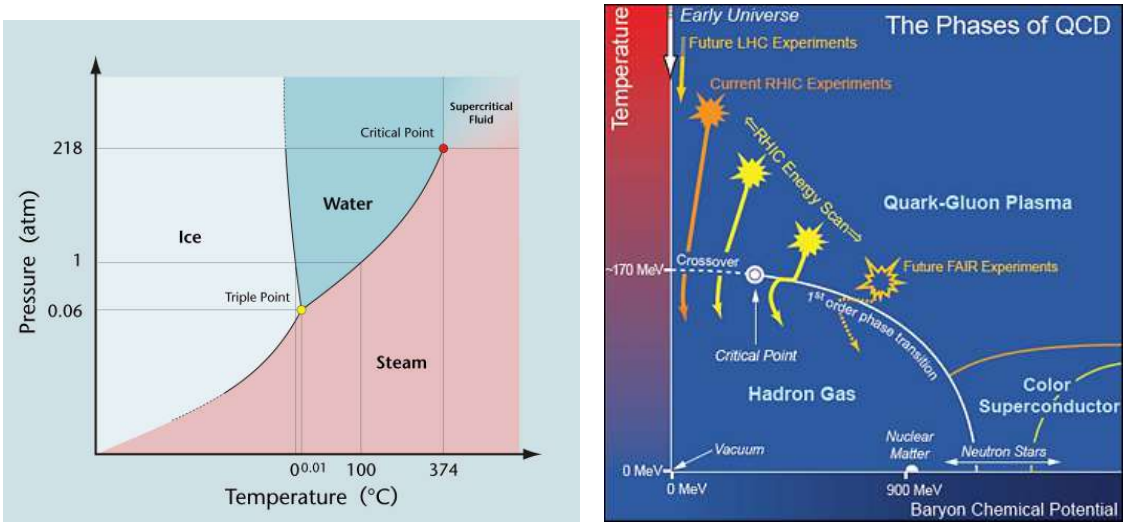

Figure 1.1: Comparision of phase diagrams: Phase diagram of water showing all the states and triple point of water where all the phases co-exist (left) and Nuclear Phase diagram showing evolution of matter as a function of Temperature. The phase diagram also shows the experiments that are probing different regions of density or temperature scale to study the behaviour of nulcear matter.

Likewise, the nuclear phase diagram depicts the evolution of the early universe after the Big Bang. The density of nuclear matter, also known as chemical baryon potential, is plotted along the x-axis. The y-axis represents temperature in natural units (eV scale) (Fig. 1.1). During the Big Bang, the universe was extremely dense and approximately 10^{32} K in temperature ($10^{-42}s$). Soon after that, quarks and gluons formed a dense, hot soup-like state of matter called quark-gluon plasma (QGP), at around 10 microseconds ≈200 MeV after the big bang [RB14]. Due to these high temperatures, gluons and quarks could escape the confinement state. After about a microsecond when and the temperature of the universe dropped to 10^{11} K, the first neutrinos and electrons were created. However, the temperature was still too high for an atom to form. For high-energy physicists, the regime where nuclear matter was formed is interesting. The universe's temperature dropped further, resulting in a freezeout; hence, quarks were confined to form baryons and mesons. The transition from deconfinement (of quarks) to confinement(to hadrons) is NOT a smooth transition governed by critical points, as we observe with the phase change of water. The articles [lbl][enc] contain all the introductory information regarding QGP and the experimental advancements in the field.

RHIC confirmed the existence of QGP for the first time in the early 2000s[Gyu04]. Almost all large facilities, including CERN, GSI-FAIR, and NICA, investigate various temperature/net baryon density regimes of the nuclear phase diagram (Fig. 1.1).

1.2 GSI-FAIR facility

The Gesellschaft für Schwerionenforschung (GSI) is one of the leading research centers in heavy ion physics located near Darmstadt, Germany. The research activities are a broad area of science covering the topics of nuclear and particle physics, atomic physics, Biophysics and Medical science, and Material research. Currently, 1520 people are working for GSI, accompanied by 1,000 researchers worldwide using GSI facilities for cutting-edge research. At GSI, one of the largest accelerator complexes is under construction called Future Antiproton and Ion Research (FAIR). All the research mentioned above will fall under the umbrella of the GSI-FAIR consortium. The four scientific pillars of FAIR mentioned below will cover all the research of GSI-FAIR.

- APPA - Atomic, Plasma Physics and Applications [APP22].
- CBM - Compressed Baryonic Matter.
- NUSTAR - Nuclear Structure, Astrophysics and Reactions [NUS22].
- PANDA - antiProton ANihilation at DArmstadt[PAN23].

The image in the figure 1.2shows the GSI-FAIR complex. The grey area is the buildings for administration, offices for the staff, and other required infrastructure. The blue lines show the existing experimental facilities with a storage ring called SIS18. SIS18 is a synchrotron that provides beams of Uranium: 50-1000 MeV/u, Neon: 50-2000 MeV/u, Protons: 4,5 GeV for the users. As part of the FAIR program, these facilities are getting a significant upgrade, and new facilities will be installed adjacent to the current facility. extending the current facilty as shown in figure 1.2 in red.

A new accelerator called SIS100 is under construction to accommodate the requirements for variety of experimental use cases. It is explicitly designed to provide high-intensity ions. When completed, SIS100 will provide beams from Protons to Uranium. To facilitate each of these experiments with high-quality beams, SIS100 will use super conducting magnets[FBV+17], which provide high flexibility in cycling the beam quality [SBB+20].

This thesis addresses the physics objectives of the GSI-FAIR program for heavy ion collisions . Two GSI experiments are dedicated to accomplishing these objectives. The first is the High Acceptance DiElectron Spectrometer (HADES) [MC+99][ZEF+99], and the second is a future experiment called Compressed Baryonic Matter (CBM)[Sen20]. Both of these fixed-target experiments use a solid target (Ca, Au, or Ag) or in some special applications such as HADES experiment, it can also use liquid hydrogen. An array of different detector-subsystems later help to investigate different particles produced as a result of the collisions.

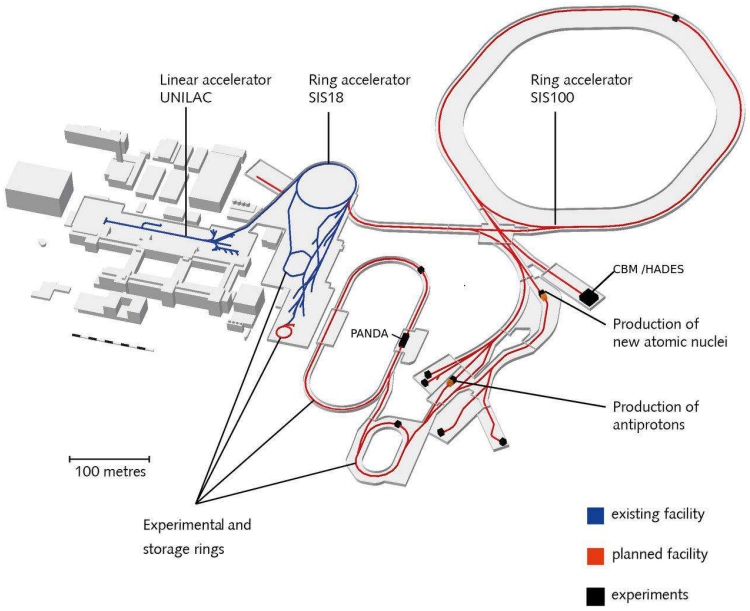

Figure 1.2: GSI-FAIR facility for heavy ion research.

1.3 Outline of the Thesis

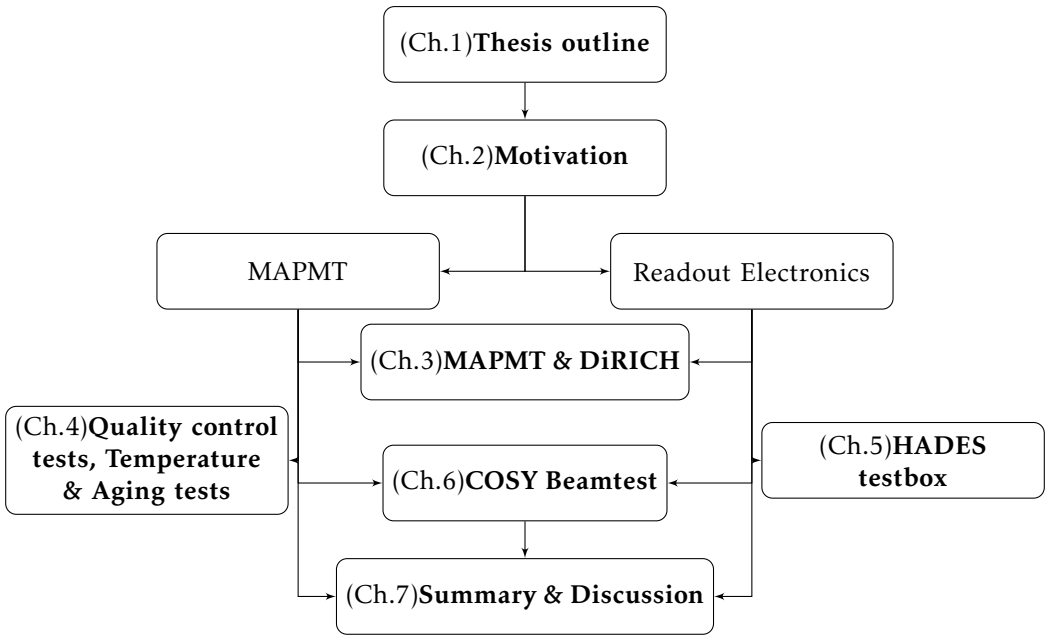

This thesis presents the instrumentation work done on the photosensor and readout electronics of the lepton detector for HADES-CBM experiments. The thesis can be divided into three sections. The first section describes the quality assurance and performance tests done on the photon sensor in the laboratory at Wuppertal. The second section describes the quality assurance and performance tests done on the newly developed readout chain specifically for HADES-CBM-PANDA RICH detectors at laboratories in Wuppertal and GSI. The third and most crucial section describes the results of both the photon sensor and the readout electronics tested under the real beam at COSY accelerator Jülich.

2 HADES & CBM EXPERIMENTS

Investigating the interactions of di-lepton pairs is one method for investigating QGP [CB99]. HADES and CBM will identify these di-lepton pairs using a RICH detector. This thesis discusses the photon sensor and readout electronics used in the RICH detectors of both experiments. Initially, the photon sensors were obtained for CBM-RICH, but it was subsequently decided to utilize the same sensors for the HADES-RICH upgrade. This chapter also provides a quick introduction to the CBM experiment before delving into the HADES experiment and its RICH detector.

2.1 CBM experiment

The Compressed Baryonic Matter (CBM) experiment is one of the main GSI-FAIR projects. CBM will measure the observables created during high-energy nuclear-nuclear collisions once it is operational. The physics objectives include, but are not limited to, determining the critical point at high baryon densities, solving the hyperon puzzle in neutron stars via the study of double lambda hyper-nuclei, and measuring the equation of state of nuclear matter[Sen20]. A detailed study describes all FAIR initiatives and their physics-related objectives[FAI].

The figure 2.1 depicts a CBM experiment's detectors in a schematic representation. Jan Kopfer's work on "Development of a prototype camera and Monte Carlo studies for the optimisation of the CBM-RICH detector" [Kop14] and Sascha Reinecke's work on "Characterisation of photon sensors for the CBM-RICH and its use for the reconstruction of neutral mesons via conversion" [Rei16]described all the technical and physics aspects of the CBM experiment. These works provide an outstanding introduction to CBM and its technical specification details. In comparison, the HADES-RICH detector upgraded in 2019, employs the same photon sensors and readout electronics as the CBM-RICH. The research presented in this dissertation focuses on the HADES-RICH upgrade and the instrumentation of its Ring Imaging Cherenkov Detector (RICH).

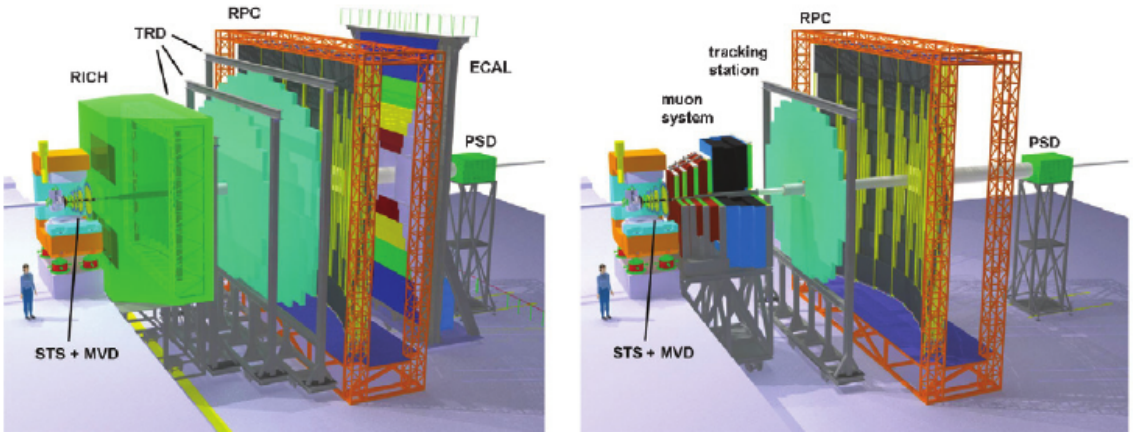

Figure 2.1: CBM experiments with different lepton detectors. Ring Imaging Cherenkov Counter (RICH) for electron/positron identification (left) and Muon Chamber (MUCH) for muon detection (right).

2.2 HADES experiment

2.2.1 Background

The HADES experiment is a collaboration involving 18 scientific institutions from nine European states figure 2.2. In 1995, the initiative began to take form, and six years later, it collected its

first scientific data in 2001[SAA+04]. The detector was operational until 2009, and its electronics were modified between 2009 and 2011. This modification improved HADES to collect data online, hence upgrading its ability to collect data at higher beam intensities and with heavier ions, such as gold and silver.

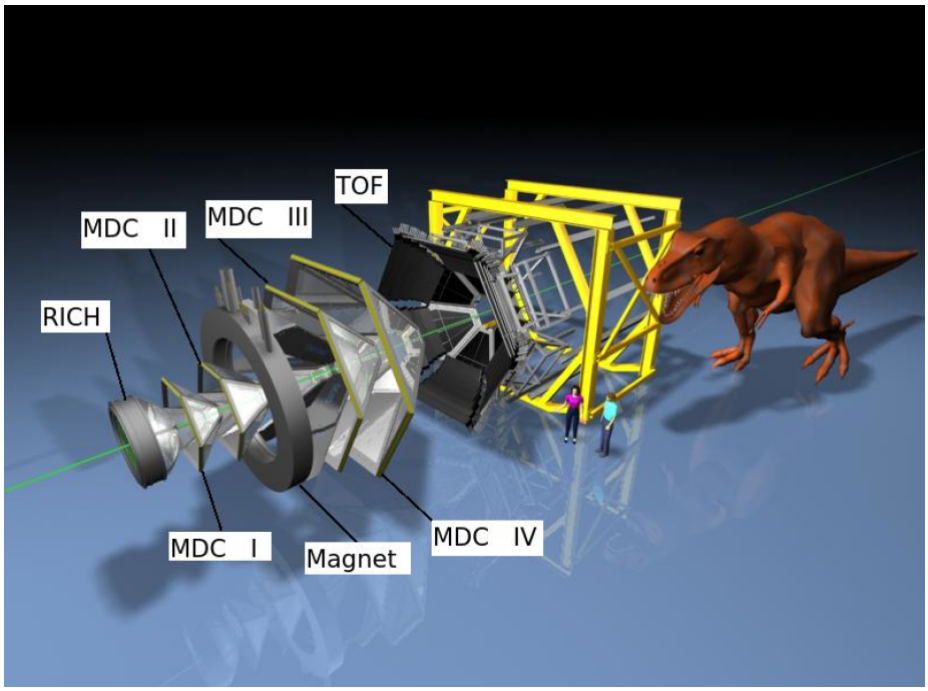

Figure 2.2: A diagrammatic representation of the HADES detector, illustrating all of its primary components along with a comparison of their size to that of a human being.

The RICH detector started its update in 2017 with new H12700 Multi Anode Photomultiplier Tubes (MAPMT) and a new readout system named DiRICH [PT18]. HADES took first data with the upgraded RICH in 2019.

2.2.2 Physics Goals

Recently, research into the hadronic matter has emerged as one of the most important areas of interest in the field of high-energy physics. In a heavily interacting medium, the characteristics of hadronic matter are expected to change, as predicted by the theoretical calculations based on non-perturbative quantum chromodynamics [RW00]. The HADES experiment at GSI was explicitly developed to research interactions of this kind. The primary objective of the HADES experiment is to investigate the in-medium modifications, in-medium masses, and widths of light vector mesons such as $\rho, \omega, and \psi$ [SBG+96]. Experimental research into these light vector mesons is being conducted for two main reasons:

1. These mesons have a very short lifespan when compared to the compression phase of heavy-ion collisions, which takes place at center of mass energies between 1-2.5 GeV.

2. Their electromagnetic decay channel into $e^+/e^- \rightarrow \gamma$ is uninterrupted by the other in medium interactions. Hence, they carry valuable information about the fireball.

HADES operates at center of mass energies between 1-2 GeV; above 0.7 GeV, the nucleus-nucleus reaction gets even more complicated. The generation of new particles, primarily mesons, increases substantially. Also, not all of these interactions are well known or well understood[SAA+04]. Consequently, it becomes intriguing to investigate the source of these particles at these energies.

Future HADES will investigate a specialized physics program for heavy ions, deuterons, protons, and pion beams [FC+99].

Di-Lepton decays are scarce at energies between 1-2 GeV. To detect these events with the maximum success, HADES-RICH was constructed with a hadron blind, which means that the active material of the Cherenkov detector was selected such that hadrons pass through it without generating Cherenkov photons [Mün07]. In addition, the Cherenkov counter is fitted with a trigger system and an electron trigger array with multiplicity. The HADES-RICH's two-stage trigger mechanism allows the selection of electron candidates from an event in real time. HADES-RICH was able to complete the physics program pioneered by the Di-Lepton Spectrometer (DLS) at BEVALAC [YBB+90]due to its large solid angle for acceptance and improved resolution [BHM98] . In 2019, the results of Au-Au collision data were published in Nature physics [AMAB+19]. Another noteworthy contribution of this experiment is searching for dark photons via di-lepton studies [ABB+14].

After its HADES-RICH upgrade in 2019, the first data was taken with silver-silver collision. The beamtime was successful, and the detector performed as expected. The physics analysis was performed by respective groups involved in the beam test [HC+21]. The future goals for HADES in the coming years can be found in [GSI].

2.2.3 Technical aspects

The HADES is a fix target experiment. All the detector subsystem are divided into a circle with six sectors sharing the same phase space around the beam pipe symmetrically. The figure below shows the transverse section of the detector. The main components which make up the HADES are:

- **START detector:** The START detector is used to determine reaction time - T_0 of collisions.It is a Monocrystalline diamond material (CVD diamond) of size 50 μm. This serves best compromise of radiation hardeness and the material budget (0.26%) [Sta].
- **RICH:** The Ring Imaging Cherenkov Detector is the main component of HADES. The RICH is upgraded and will be discussed in detail in the next section.

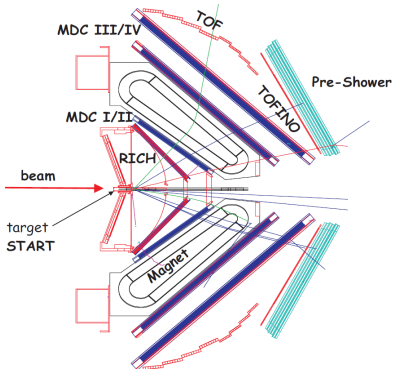

Figure 2.3: Transverse section of HADES with all detector systems.

- **MDC:** Micro(wire) Drift Chamber or MDC are the tracking detectors of the HADES. They have six trapezoid sections. Each section is a chamber of multiple layers of crisscrossed wires. The whole chamber is filled with helium and butane gas. The wires serve as an anode. As the charged particle passes through the chamber, they ionize the gas atoms, triggering the signal at the adjacent anode wire. As shown in the schematics of figure 2.3, two MDCs are located in front of the magnet (MDC I/II), and two are behind the magnet (MDC III/IV) for better precision of tracks[TFK+08].
- **Magnet:** HADES has a superconducting magnet (3.6T) producing a toroidal field. The idea behind this is to give the charged particles a transverse kick to amplify the momentum resolution ($\sigma_{p/p}$ = 1.5–2% for electrons). The location of the magnet is behind the RICH because the RICH requires a field-free region around the target and in the active volume[Mag].
- **Time of Flight detector:** Time of flight detector is made up of 6 sectors making a hexagon. Each sector has 8 cases containing eight scintillating detectors. The scintillating detectors have readouts from PMTs (EMI9133B). This enables the detector to have an accurate time of

flight measurement (100-150 ps) and position resolution of about (1.5-2.3 cm). The main task of TOF is to measure hadron multiplicities and to discriminate electron/hadron signals[BBC+09].

- **Pre-Shower Detectors:** Pre-shower detectors further distinguish electron and positrons from other particles. The pre-shower detectors are two lead convertors between three wire chambers. The shower is detected by comparing the number of particles measured before and after the lead convertors.
- **ECal:** The ECAL allows the HADES to detect photons emitted in rare decays such as neutral Lambda (1405), neutral mesons, or sigma (1385) resonances in elementary and heavy-ion interactions. It also helps in improving electron to pion separation at large momentum values[SBC+14].

Apart from the detectors mentioned above, the other components of the HADES are RPC, Hodoscope WALL, DAQ and trigger system. The description of all of these components such as their role in the experiment, dimensions and other details can be found at [cAA+09] & [Ram09].

2.3 HADES-RICH detector: Old & New

2.3.1 Old RICH detector

Figure 2.4 shows the schematic diagram of the old RICH detector. The beam enters the detector from the left and strikes the target located within the RICH volume. Cherenkov photons are released by particles traveling through a detector chamber filled with radiator gas (C_4F_{10}) (cyan color). These photons are reflected by a reflective carbon mirror (curved blue surface) on to the photon detector plane shown in red. In order to avoid external pair conversion and multiple scattering, the detector components have to have a minimal material budget due to the limited space for particles to move in the detector's radiator volume. The radiator gas was perfluorobutane C_4F_{10}, which has a high transmission at λ = 145 nm and an appropriate Cherenkov threshold to suppress muon and hadron radiation in the specified momentum regime.

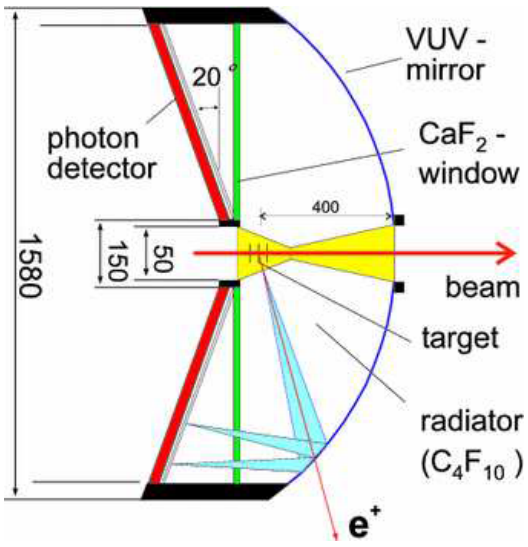

Figure 2.4: Schematic diagram of the RICH detector showing its components.

A thin carbonfibre shell encloses the whole assembly which essentially is a field-free region. There is a CaF_2 window separating the photon detector from the active volume of the radiator gas. The RICH photon detector consists of 6 trapezoidal modules (area 0.25 m^2), forming a hexagonal pyramid to match the curved focal plane of the mirror. The focal plane is arranged in such a way that Cherenkov light emitted from the straight particle trajectories between angles 20° to 80° have path lengths of 36 cm to 65 cm respectively. A thin gap MWPC (d = 5.5 mm) with asymmetric field and a pad cathode readout read each module.

VUV mirror: For high $e^{\pm}$ identification efficiency, RICH requires a large number of photons per Cherenkov ring ($N_{det} \geq 10$). Due to short radiator length and work function of solar-blind CsI photocathode enforces that spectral sensitivity of the RICH is high in vacuum Ultra Violet (VUV)

region. For this purpose, the mirror substrate is coated with MgF_2 protected with aluminium coating and a CaF_2 entrance window. The main parameters of the mirror are shown in table 6.1:

Table 2.1: Technical parameters of the VUV mirror for HADES-RICH (figure 2.5(left))

Parameters	**Value**
Outer diameter D	1440 mm
Radius of curvature R_i	872 mm
Substrate thickness d	$\leq$ 2 mm
Radiation length X_0	$\geq$ 20 mm
Reflectivity R (λ=150 nm)	$\geq$ 70 %
Suface roughness σ (rms)	$\leq$ 3 nm

CaF_2 Window: The CaF_2 window separates radiator gas from the photon detector. The window is made up of sixty-four hexagonal-shaped single crystals of 200 nm in diameter and 5 mm thick each. For each crystal, the CaF_2 raw material was properly selected and then polished individually. The polished crystals are glued together to form a disk of 1500 mm diameter. The central hexagon had a hole to accomodate the beam pipe. Furthermore, six thin spokes support the window on both the side against the pressure differences in the detector (figure 2.5(right).

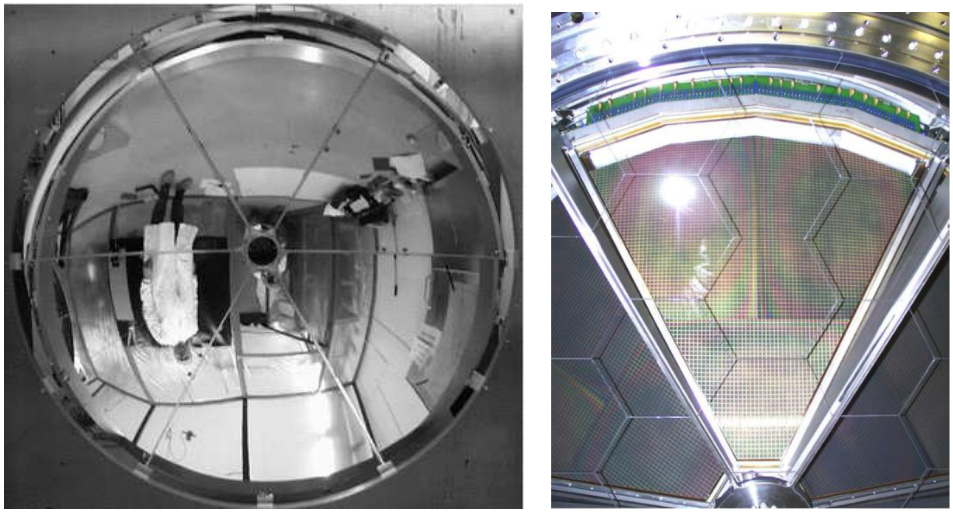

Figure 2.5: HADES-RICH VUV mirror with all six sections (left) and the CaF_2 window showing the hexagonal crystals and the supporting spokes (right).

Radiator gas: The gas volumes for radiator and photon sensor is about 700 litres each and are filled at 1–40 hPa above STP. For photon detector, commercially available methane gas is supplied through an open system with a gas flow of about 300-350 l/h. On the other hand, the radiator volume is filled with a batch of C_4F_{10}. The gas is supplied from a reservoir and recirculated from a closed system via evaporation and compression-liquefaction chain. The flow and the pressure of the gases are monitored by a PLC controlled gas supply system which maintains the pressure difference between MWPC and the radiator below 3 hPa to protect the delicate CaF_2 window.

Performance: The number of Cherenkov photons per ring determines the performance of RICH, which is given by N_{det} . The simulations show that the detector performs best for $10 < N_{det} < 18$ [AMAB+19]. For $N_{det} < 9$, the efficiency of e^+/e^- identification is significantly affected along with online trigger efficiency. The complete system tests showed that the gas amplification of about 3-9 $\times 10^4$ was achieved during the tests and single-photon detection efficiency. This translates into 10-20 % less yield than the calculation from the simulations. In summary, the overall performance

of the RICH detector system, although slightly lower than in the original design, has proven to be sufficient for e^+/e^- identification in nuclear collisions.

The HADES experiment overcame many challenges, by and large contributed to its purpose. It has served the community for 20 years, and with its new upgrade, it is foreseen to be accommodated in future GSI-FAIR programs.

2.4 Upgraded RICH detector

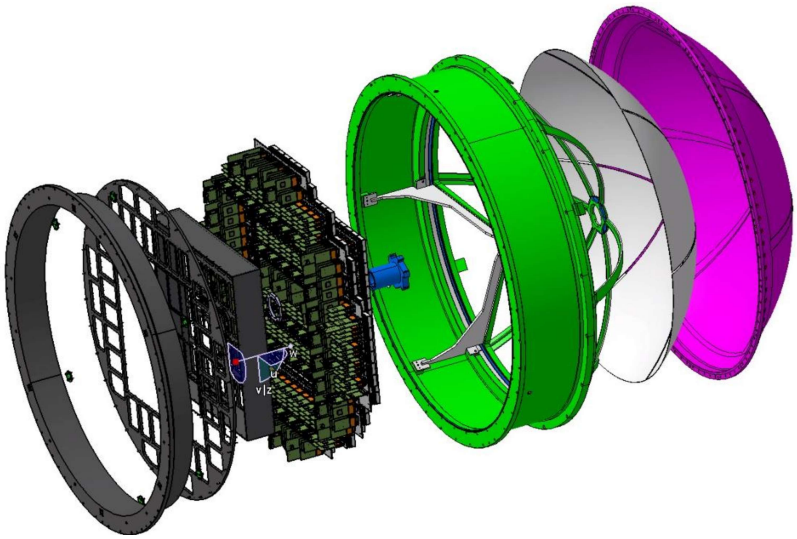

Figure 2.6: HADES-RICH upgrade concept showing the detector shield (pink) the VUV mirror (white), the flange holding the photon detector, the upgraded photon detector with MAPTs in the front (gray) and readout PCBs at the back (dark green).

2.4.1 Motivation for the upgrade

The operation of HADES for 20 years now shows the effect of aging on its performance. The physics analysis of Au+Au run showed the loss in Cherenkov photon statistics, and the response of RICH detector had been degraded by 40-50% over the years. This has hampered the e^+/e^- ring identification owing to low photon statistics and the charged particle-induced background in the pad readouts. As per the FAIR future plans, the HADES will be used together with CBM using ion beams from FAIR SIS 100 accelerator. In its current state, the stable operation of HADES is not possible even with the current SIS 18 accelerator [PEF+17].

2.4.2 Concept

The CBM experiment at FAIR will investigate heavy-ion collisions by 2029 at SIS 100 accelerator [SBB+20]. For its RICH detector, the CBM has ordered 1100 H12700 MAPMTs from Hamamatsu. In a joint effort of both the CBM and the HADES collaborations, it was decided to use 428 of these MAPMTs to replace existing CsI+MWPC readout of HADES-RICH as a photon detector on a short time scale. All other major components of the RICH, i.e. VUV mirror and the CaF_2 window - will be used as it is, while only the photon sensor (and later the radiator gas) will be replaced [PEF+17]. The new flange with MAPMTs and new readout system will replace the old flange carrying the CsI + MWPC readout. Thus, it will be easy to test the MAPMTs and readout in a dedicated test setup before its installation in the main detector. The mechanical design of the new device is shown in the figure 2.6.

The main problem with this upgrade was the plane of the photon sensor. CsI photon detector was curved to match the focal plane of the mirror while the same was not possible for with MAPMT, since the MAPMTs are square and have a planer surface profile. To achieve optimum acceptance and simultaneously match the focal plane of a curved mirror, the circular plane was divided into two parts. The inner rectangular part was elevated by 120 mm in the z-direction (direction of beam axis) hosting 14×14 MAPMTs and the outer part having the remaining MAPMTs in the combination of 3×2 and 2×2 MAPMTs modules as shown in the figure 2.7. The MAPMT and the readout electronics will be discussed extensively in the next chapter.

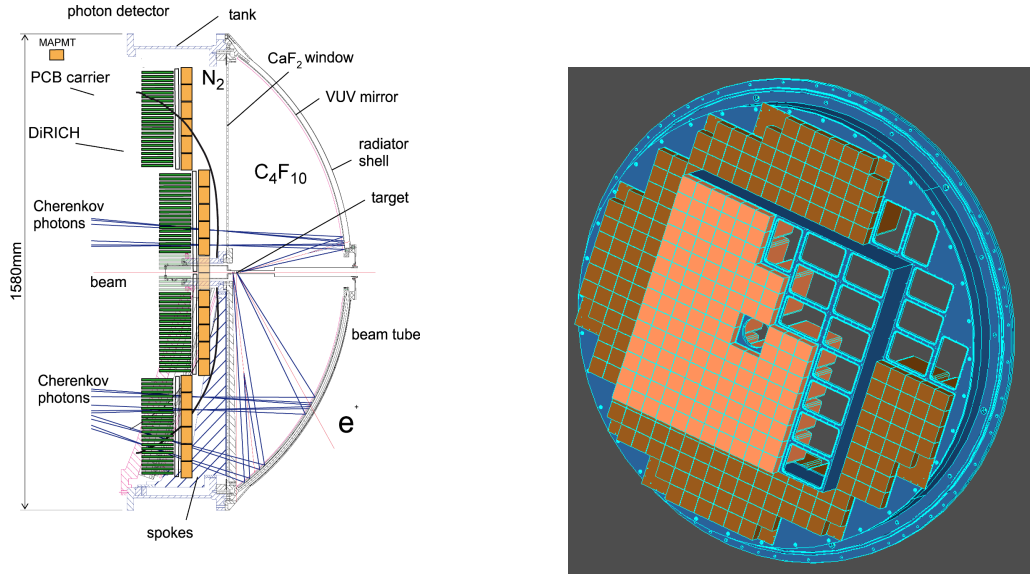

Figure 2.7: HADES-RICH photon detector upgraded with MAPMTs (yellow) and readout electronics (green) (left) and the circular flange showing both the housing of MAPMTs and the elevated section of the detector to match the curved focal plane (right).

2.4.3 Advantages of upgrade

The main motive using a common light sensor and readout electronics for both the HADES and the CBM -RICH detectors was two-fold;
(i) HADES is an existing detector and upgrading it with these MAPMTs will act as a realistic test environment for these new photon sensors and readout chain developed, keeping in mind for all the future experiments at GSI-FAIR.
(ii) The upgrading of the HADES-RICH will improve its efficiency of e^+/e^- identification in particular in close pairs. It will also ensure the stable operation of the detector in SIS 18 accelerator energies in 2020 and even beyond at SIS 100 energies in future along with the CBM experiment.

2.4.4 Simulations

The performance simulation for upgraded RICH was done in HADES HGEANT/HYDRA software framework. The simulation included the spectral quantum efficiency and collection efficiency based on data sheets provided by the manufacturer and the lab measurements to estimate correct Cherenkov photon yield and ring reconstruction efficiencies. The CBM ring finding algorithm has been adopted, which is based on localized Hough transformation, ring fitting, and ring acceptance using neural networks. As per the simulations, the number of detected photons varies from 7 to 15 depending on the e^+/e^- polar emission angles. The photon yield increases on the periphery of the detector owing to increase in path lengths of the Cherenkov photons. The estimated ring radius is about 22 mm roughly the size of one MAPMT (figure 2.8)[LFKH17].

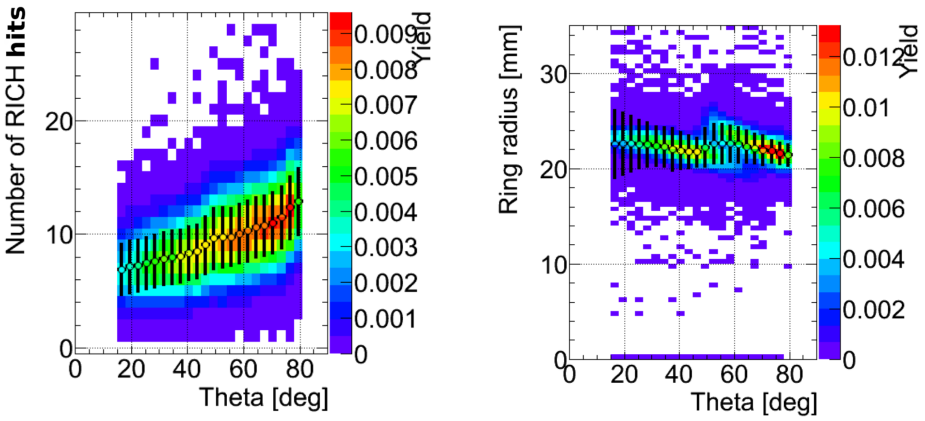

Figure 2.8: The simulations shows higher number of hits for a large angle of emission between 10 to 15 for angles exceeding 60° (left) and the estimated ring radius affected by step profile of upgraded RICH (right).

The new MAPTS are highly sensitive to detect single photons while having minimum crosstalk probability (<15% crosstalk hits depending on the applied threshold) and the improved ring finding algorithm results in an improved reconstruction efficiency of detected e^+/e^- pairs almost by order of magnitude. It also suggests that the overall efficiency of detecting the dilepton candidates, especially those which are separated by small polar angles, will significantly increase as shown in the figure 2.9.

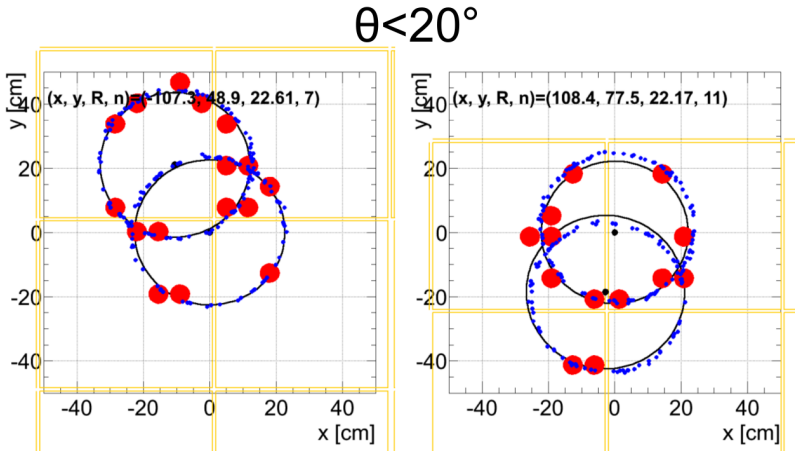

Figure 2.9: The simulations showing two different events of e^+/e^- pairs seperated by very small emission angles yet, were successfully reconstructed with reasonably good number of hits. The blue dots represent the hits in the event and the focussed hits represented by larger red dots are the hits used by the ring finder to reconstruct the respective e^+/e^- pairs with a small opening angle.

The simulations showed promising results, and hence plan for the RICH upgrade was initiated in 2017. In the meantime, the MAPMTs procured for the CBM experiment were already undergoing series-testing for their quality. The first prototypes of readout electronics were also available for the tests. The next chapter introduces the photosensor - H12700 MAPMT from Hamamatsu and DiRICH based readout concept in detail.

3 MAPMT & DiRICH

The delivery of photon sensors for CBM and HADES RICH started in 2015, and the initial shipment of MAPMTs had arrived in Wuppertal. Numerous tests were conducted to see if the MAPMTs matched the selection criteria outlined in Appendix A. During the same year, initial shipments of DiRICH-FEE readouts came to Wuppertal. This chapter introduces the technical details of H12700 MAPMT and the initial laboratory tests conducted on DiRICH front-end boards in Wuppertal.

3.1 What is a MAPMT?

Photomultiplier tubes (PMTs) are widely used in particle physics and astronomy research to detect photons. The Photomultiplier tube operates on the concept of the photoelectric effect, where light from the source strikes the photocathode of the PMT and generates a photoelectron. The subsequent dynode chain multiplies the photoelectron, increasing the photoelectron gain to a detectable level. For a standard PMT, this gain is between 10^6 to 10^8, with a range of 9 to 12 dynodes. Consequently, a PMT is a photon detector with several academic, medicinal, and industrial applications [Pol13]. However, a PMT has one minor limitation: the cathode is often a single piece of photosensitive material that responds to light from any direction. Consequently, using the PMT as a spatial position detector becomes restricted in specific applications. Thus, a conventional PMT is a zero-dimensional detector.

In contrast, the MAPMT can have many anodes based on the configuration, such as 32 or 64 [KSTO85]. A MAPMT has numerous applications, including the measurement of a spatially distributed intensity profile or the spatially resolved measurement of single photons, a spectral response comparable to that of a CCD [MCH$^+$12]. For the HADES (and CBM) experiment, RICH detectors will be used to identify lepton particles[PT18]. The anticipated Cherenkov ring size for HADES is around 5 cm in diameter, with up to 15 photon hits in each detected Cherenkov ring[LFKH17]. In order to generate a Cherenkov ring during analysis, the spatial position of each photoelectron hit must be known. Therefore, Multi-Anode Photomultiplier Tube (MAPT) is a more suitable option for this application.

3.2 H12700 : The photon sensor for the RICH

The primary element of any RICH detector is the photon sensor, which detects Cherenkov radiation. For HADES and CBM RICH detectors, Hamamatsu H12700B Multi-Anode Photomultiplier tubes (MAPMT) were chosen as photon sensors (figure 3.1). This decision was made following a comprehensive review of numerous candidates from different companies. These evaluations comprise tests conducted at the Wuppertal laboratory and a dedicated beam test conducted at CERN in 2012. Previous work from [Rei16, Kop14] describes in-depth study and analysis in numerous situations, as well as the criteria satisfying the scientific requirements of the CBM experiment for these candidates for the photon sensor. The RICH working group and Hamamatsu have agreed upon a set of criteria [App. A] for determining the quality of each MAPMT. The MAPMTs were delivered in batches and checked for quality assurance at the Wuppertal laboratory. Every critical parameter of the provided MAPMTs was measured by a specific test setup. Checking the photocathode's homogeneity and absolute quantum efficiency were amongst the most important aspects. The following chapter explains the characteristics and results of this setup.

3.2.1 H12700 specifications

Some important parameters of H12700 MAPMTs are discussed as follows: All of the above metrics are measured at 1000 V operating voltage. For the HADES and CBM RICH, H12700B MAPMTs are selected as the camera's photonsensor. Figure 3.2 depicts the H12700B MAPMT's complete circuit

Figure 3.1: H12700A with a cable for supplying input voltage (left) and H12700B can be powered directly from a mount (right).

- **Physical dimensions:** 5.2×5.2 cm with an active area of 4.87×4.87 cm.
- **Pixels:** 64 pixels in the combination of 8×8 with each pixel of the size 6×6 mm /anode.
- **Photosensitive material:** Bialkali.
- **Peak quantum efficiency:** 33% @ 380nm (claimed).
- **Wavelength:** 185 - 650 nm.
- **Dynodes:** 10 metal channel dynodes.
- **Gain:** 10^6.

layout. It highlights all the crucial details, like pixel position, High Voltage (HV) connectors, and the dimensions of each component in millimeter.

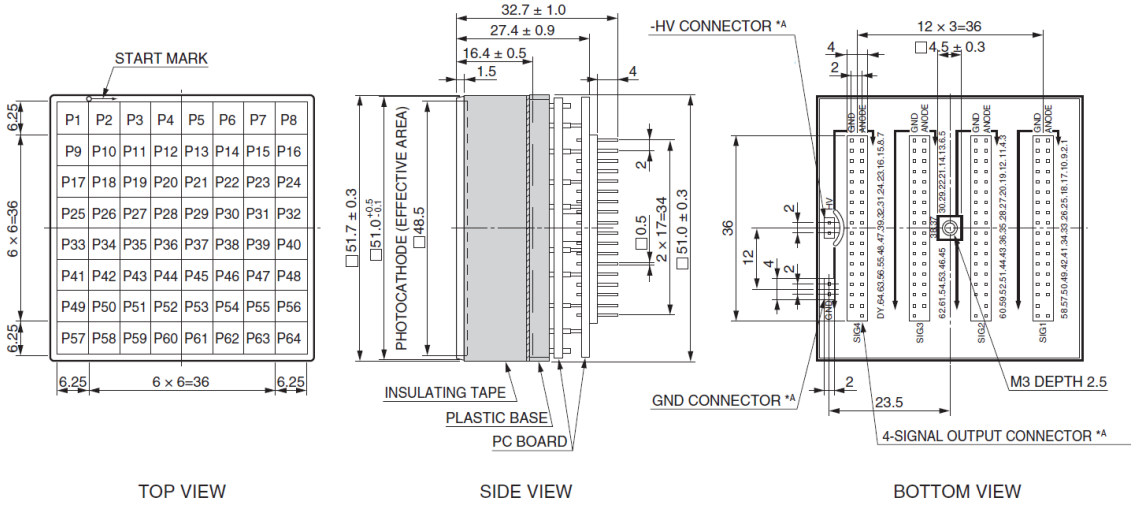

Figure 3.2: H12700B circuit diagram showing all the components [PMT].

3.2.1.1 Photo-Cathode

The photocathode is made of many compounds, and each photocathode has unique properties. The selection of a photocathode is determined by its spectral properties for the wavelength of interest[SN09]. Bialkali is the photocathode utilized in H12700 MAPMTs (Sb-Rb-Cs or Sb-K-Cs). A Bialkali photocathode features low dark noise, outstanding blue sensitivity, and up to 30% quantum efficiency. They are suited for applications involving scintillation or photon counting, which is the primary need for any RICH detector [NHIM10]. The window material is a UV glass that allows radiation transmission from 185 nm to the near-infrared region.

3.2.1.2 Dynode chain

The photoelectron produced by the photocathode is collected by the dynode chain. Each stage multiplies electrons until the final dynode, where the output is high enough to be extracted. Depend-

ing on the application, each photomultiplier tube utilizes a unique dynode design. For the H12700 MAPMTs, the dynode chain consists of a metal channel mesh type design as shown in figure 3.3.

3.2.2 Functioning of a Photomultiplier Tube

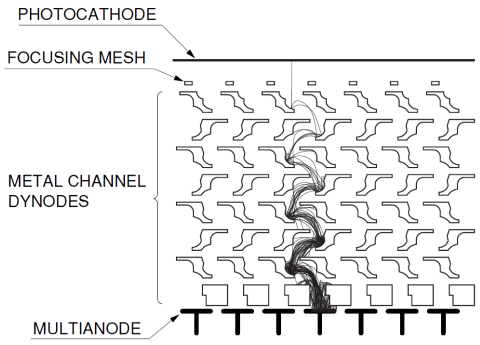

Figure 3.3: The schematic diagram shows the metal channel dynode scheme and the path of electron multiplication towards the anode

A MAPMT circuit diagram is depicted in figure 3.4. Every photomultiplier tube, regardless of brand, has a same circuit configuration. The circuit diagram generally consists of three sections denoted by red, blue, and green circles. Each section of a MAPMT serves a distinct purpose in maximizing its performance. The photocathode K receives incoming photon (or photons) from 64 pixels labeled P1 through P64. The resulting photoelectron is then focused on the dynode chain denoted by DY1 to DY10. Each dynode stage is linked to the next by means of voltage divider resistors R1 through R18. For the proper operation of a PMT, the voltage divider circuits ensure that a consistent inter-stage voltage is maintained at all dynode stages. The basic objective is output linearity with respect to input. Due to the increase in electron density and space charge effects, this state is no longer maintained in the later phases of the PMT. Decoupling capacitors connected to later stages (indicated in the blue circle in figure 3.4) eliminates this issue and is also useful in the pulse-operation mode of MAPMT [PMT].

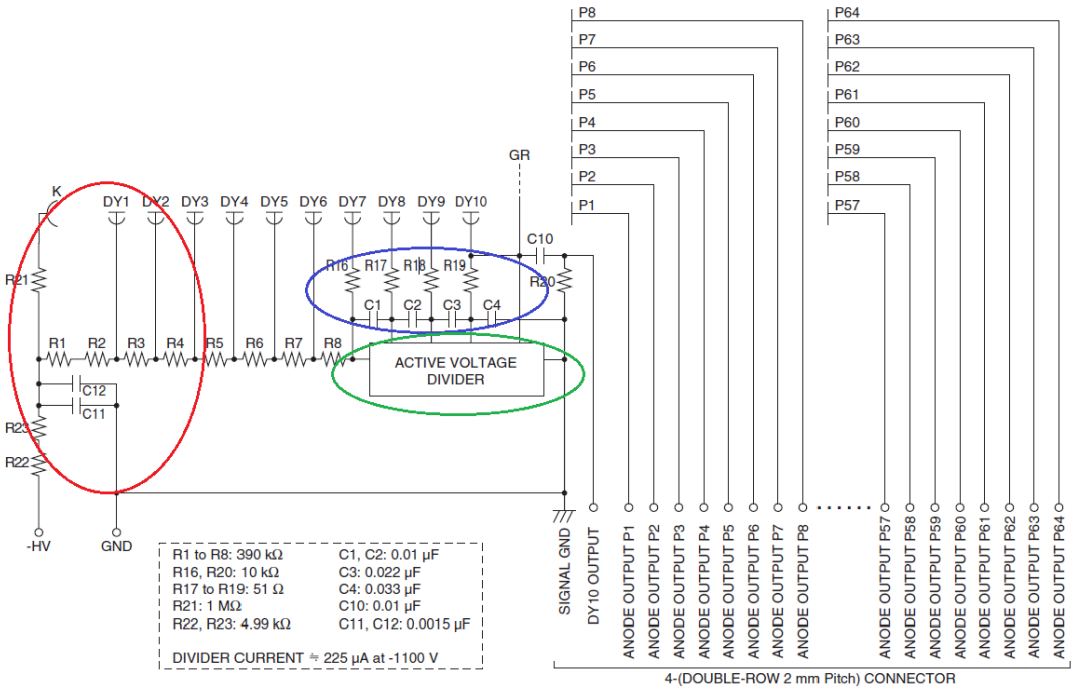

Figure 3.4: The circuit diagram of the MAPMT shows different components contributing to the efficient collection of the signal at the anode(s) [PMT].

In the same way that voltage distribution is vital in later stages for output linearity, proper voltage distribution in the early stages is also essential (shown in the red circle in figure 3.4). The output signal-to-noise ratio, pulse height dispersion of single and multiple photon regions, and transit time spread (TTS) of a PMT are determined by the voltage between the cathode, focusing electrode, and the first dynode [PMT]. Thus, it influences the photoelectron collection efficiency and secondary emission ratio of the first dynode.

Active voltage dividers (shown by the green circle in figure 3.4) typically consist of a series of FETs placed between the dynodes and a high-impedance resistive divider. The FETs maintain the dynodes at constant potentials. This sort of divider guarantees a consistent gain up to 100 uA of anode current. Typical power consumption is 100 mW; therefore, they are ideal for portable instrumentation.

3.3 DiRICH readout concept

Several current and prospective FAIR experiments, including the HADES-RICH upgrade, the CBM-RICH, and the PANDA Barrel DIRC detector, will utilize the same or comparable photon detectors (H12700 MAPMTs for HADES and CBM [MFF+17], Photonis Multianode MCP detectors for PANDA Barrel-DIRC [SAB+18]). The primary objective of this detector's readout chain is to achieve a high detection efficiency, good timing precision, and (in the future) a self-triggered readout scheme for numerous readout channels. To achieve a cost-effective solution for the reading of these PMT- or MCP-sensors, a common electronic readout chain known as DiRICH is developed.

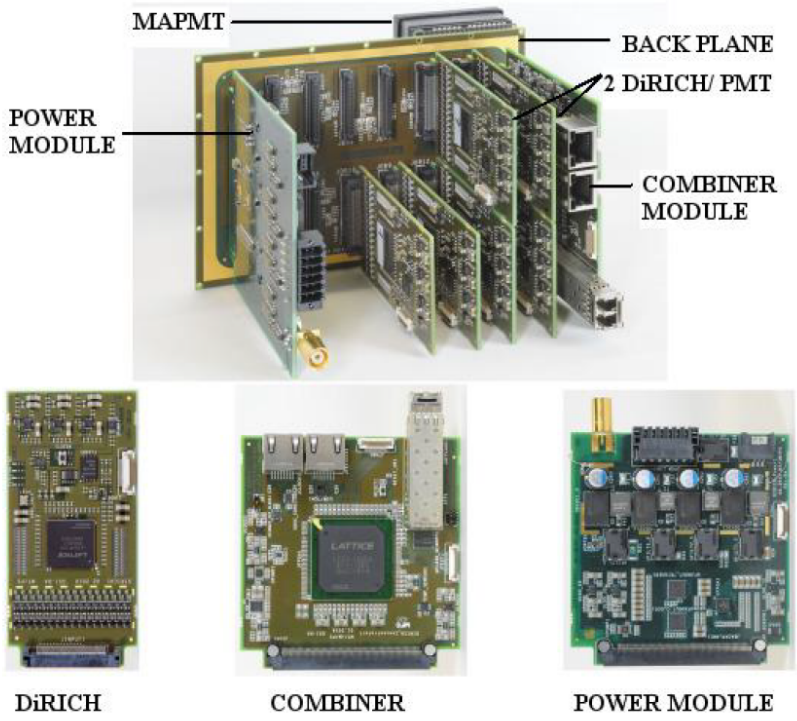

Figure 3.5: The DiRICH readout scheme with all the individual components.

The development of the DiRICH readout chain is the next step in the continuous improvement of the readout electronics utilized in several GSI experiments. for RICH detectors, the DiRICH replaces the previously used n-xyter readout scheme [NAMH+13]. The DiRICH - an FPGA-based readout system is a more adaptable alternative to the n-xyter - an ASIC-based FEE. The development is based on TRB technology, which was developed and is maintained by the TRB collaboration

[FSS+08]. A high-precision, state-of-the-art FPGA-TDC design enables time measurements of digital signals with a 10 ps RMS precision. The system also comprises a high-bandwidth, low-latency data acquisition Network (TRBNet) and control software. Next sections explains the workflow of signal processing and data collecting, as well as the function of each link in the chain.

The 32-channel DiRICH front-end module, based on the Lattice ECP5 FPGA - the same FPGA-TDC technology already developed for the existing modules [NAMH+13], is the core part of the readout development. Following analogue amplification and shaping on the DiRICH front-end module, the differential input line receivers of the FPGA are used to discriminate and digitize the input signals. This strategy enables a highly integrated and cost-effective system with few additional components. The DiRICH readout chain design relies on the accurate time measurement of the leading and trailing edge of the analogue input pulse, and the Timeover-Threshold measurement provides amplitude information for background suppression.

The main components of the DiRICH readout scheme (partially equipped with FEE and MAPMT) is shown in figure 3.5:

- **DiRICH Backplane:** The backplane carries six MAPMTs in a 3x2 configuration and connects them to twelve DiRICH readout modules. Additionally, it supports all digital interconnections between modules as well as LV and HV distribution. The backplane also serves as the detector-volume's gas and light-tight enclosure.
- **Combiner module:** The combiner module combines the digital output links of up to 12 DiRICH readout modules and transmits data from all six PMTs to the DAQ system through a single optical link.
- **Power module:** The power module provides LV distribution and monitoring for all backplane modules and HV power to the sensors. On-board DC/DC converters permit a simple 48 V low-current powering system at the cost of increased switching noise. A low-noise external LV supply can be utilized as an alternative to the DC/DC converters.
- **DiRICH Front-end Board:** The DiRICH front-end board will be mounted directly to the backplane of a MAPMT (figure 3.6). Each module's LVS connection can read 32 channels. Therefore, two DiRICHs are required for one MAPMT (64 channels). The module consists of three sections: an analog amplifier, one FPGAs onboard, and voltage regulators. When the signal reaches the DiRICH, the amplifier amplifies it before sending it to the FPGA, where it is converted into a digital signal and transmitted to the DAQ through a combiner board.

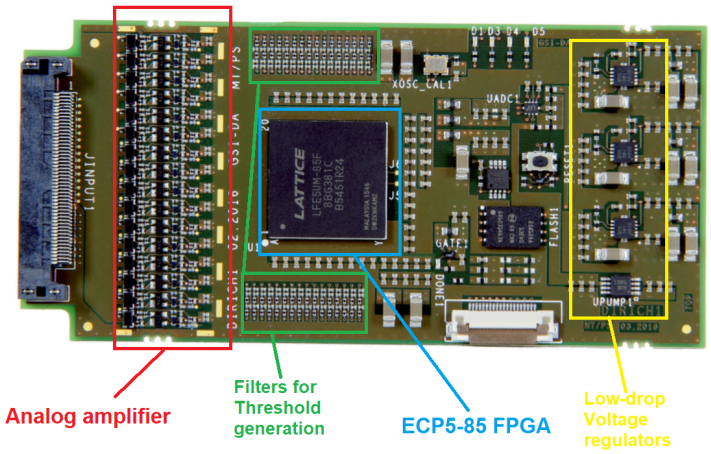

Figure 3.6: DiRICH front-end module's first iteration with location of the analog amplifiers, the FPGA and other components.

Some of the important features of the DiRICH front-end module are:

- → The dimension of the module is 47×100 mm.
- → Onboard linear voltage regulators with ultra-low drop (<40 mV).
- → Galvanically decoupled from the MAPMT(via transformer), 16bit-DAC, discriminator, high precision TDC, DAQ + TrbNet (2Gbit/s SERDES), slow-control and voltage-regulation (figure 3.7).
- → Small component size of 300 μm×600 μm.
- → Operational from -40 °C to 80 °C temperature ranges.

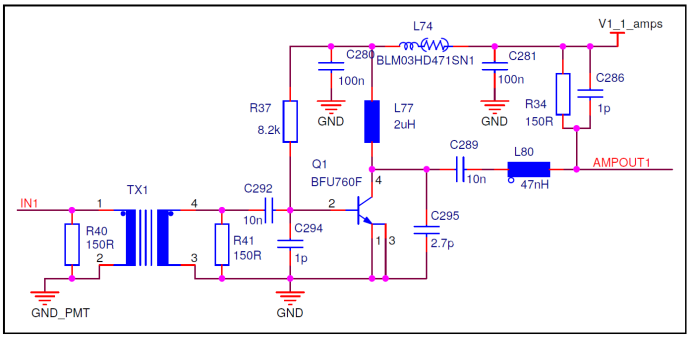

Figure 3.7: Circuit diagram of the analog amplifer on the DiRICH.

The basic features of the analog amplifier are:

- → Small footprint of 12×27 mm^2.
- → 0.6×0.3 mm (0201) component sizes.
- → 12 mV @1.1 V power dissipation.
- → Gain of 20-30 depending on signal amplitude.
- → Noise figure of 3.6dB @950 MHz.
- → No output inductors required.

The basic features of the Lattice-ECP5-85F FPGA are:

- → small size of 17×17 mm^2.
- → 0.6×0.3 mm (0201) component sizes.
- → High precision TDC (≈10 ps RMS).
- → 84k LUTs enough for 32 channel ToT.
- → Onboard discrimination of the signals.
- → 84000 Logic elements.
- → 42000 Adaptive logic modules (ALM).
- → Operating Voltage of 1.1V supply current 212 mA.
- → Data rate of 3.16 Gb/s.
- → Economical to purchase ≈40 euro/piece.

Other details about the FPGA and can be found in [ECP].

3.4 Preliminary tests of DiRICH FEE

The first DiRICH FEE prototypes were tested utilizing a DiRICH test board (Fig. 3.9). The test board is capable of testing two DiRICHs at once. Each DiRICH channel on each side is represented by the SMA connections on both sides. The low voltage necessary to power the DiRICHs is supplied via the center connector. The active/passive probes of an R&S oscilloscope are attached to the DiRICH amplifer channels externally as illustrated in figure 3.9 to measure the output from the DiRICH. Studying analogue amplifier characteristics including gain, noise, amplification, and linearity was the test's top concern.

For the test, an external voltage source provided a pulse via the SMA connector to one of the channels on the DiRICH, and the amplified output from the preamplifier corresponding to that channel was obtained on an oscilloscope using either an active or a passive probe connected to the channel, as depicted in figure 3.8. The following are a few of the most noteworthy results from these tests:

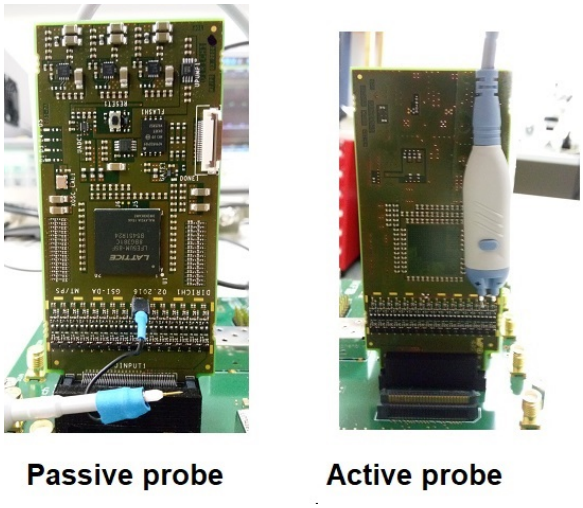

Figure 3.8: DiRICH FEE attached on a backup-board for testing with a passive probe (left) and an active probe (right) attached to analogue amplifier.

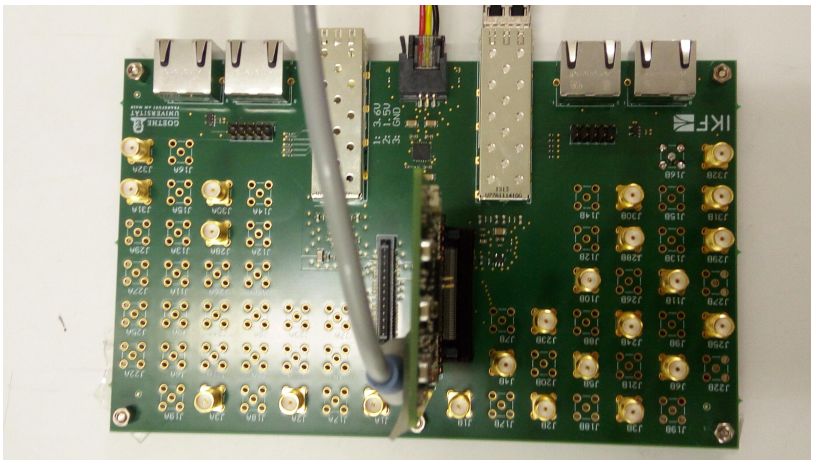

Figure 3.9: DiRICH mounted on the backup board and one of the channel connected with the passive probe (left) or with the active probe (right) of a R&S 4 GHz oscilloscope.

Pulse shape: Figure 3.10 depicts the oscilloscope screen capture for one of the channels. The blue curve represents a 5 mV input pulse, whereas the green curve represents the corresponding output as seen after the preamplification, seen by the discriminator and FPGA-TDC. As shown, the output is a smooth curve devoid of jitter or other fluctuations. The undershoot in the output signal is a characteristic of the amplifier, and it aids in the accurate estimation of the signal's trailing edge and hence the Time over Threshold (ToT) measurement. Since there is no direct amplitude measurement function in DiRICH, the ToT, which will be explored in detail in chapters 5 and 6, is a necessary parameter for DiRICH to obtain pulse information.

Gain characteristics: The DiRICH has 32 channels and it is important to know the channel-to-channel gain. It is vital because if the gain difference between individual channels is too large then

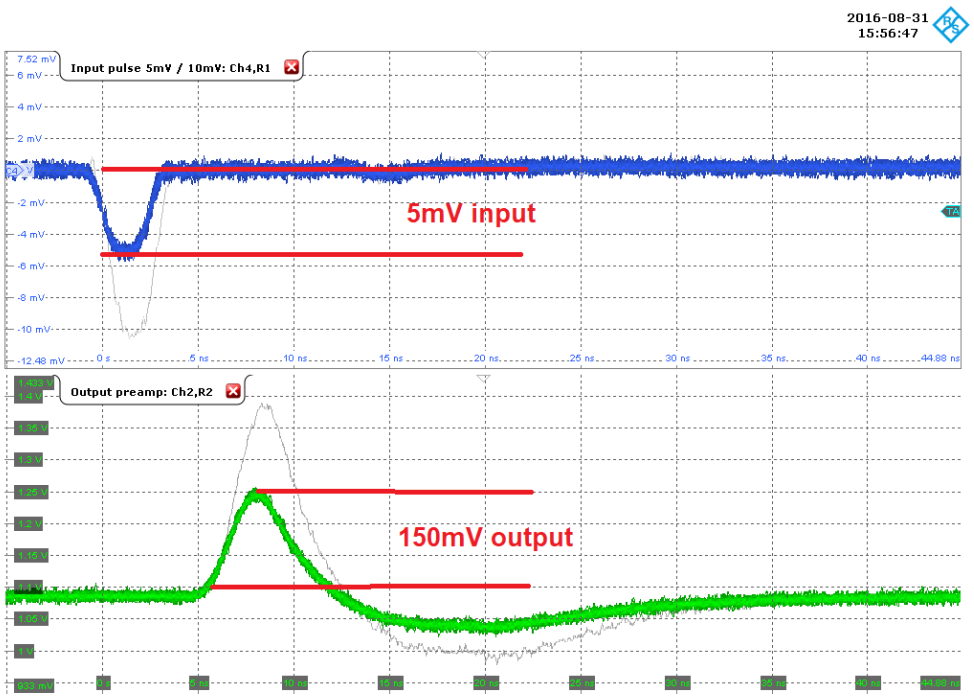

Figure 3.10: The oscilloscope image displays the 5 mV input signal (blue) and the 150 mV amplified output signal from the DiRICH.

threshold adjustment at individual channel level becomes challenging. Thus, the readouts were tested to verify the gain uniformity for all channels.

For the initial measurement, the gain was shown as a function of the channel number for two different signal widths, 1.5 ns and 3.5 ns, with an amplitude of 10 mV. A typical MAPMT signal falls within this range. For the second experiment, the gain was displayed as a function of the amplitude of the input signal for a 1.5 ns and 3.5 ns signal width. The following conclusions can be derived from these graphs:

1. Figure 3.11 demonstrates that the amplifier's gain matches the claimed value of 30, but this was not the case for every channel. As shown in figure 3.11, the gain characteristics were not consistent across all channels.

2. As expected, the gain of the amplifier did not change significantly for either active or passive probes, as shown in figure 3.12. However, the input pulse width has a substantial effect on the gain of the amplifier. The average gain for a signal with a width of 1.5 ns was 24, whereas the average gain for a signal with a width of 3.5 ns was 35. Consequently, for a typical MAPMT signal width of 2 ns, the predicted gain is 30.

3. Figure 3.13 illustrates the link between the gain of the preamplifier and the pulse voltage input. Due to the low input voltage of 1.1 V, the pre-amplifer has limited dynamic range and hence goes into saturation. This is demonstrated by the graph that as the amplitude of the pulse grows, the gain of the amplifier drops. For an input pulse of 60 mV, the gain is reduced to almost half. However, the signal from a MAPMT with an amplitude of 60 mV is seldom. A typical single photon signal from MAPMT has an amplitude of around 10 mV, for which we have good gain characteristics from the DiRICH.

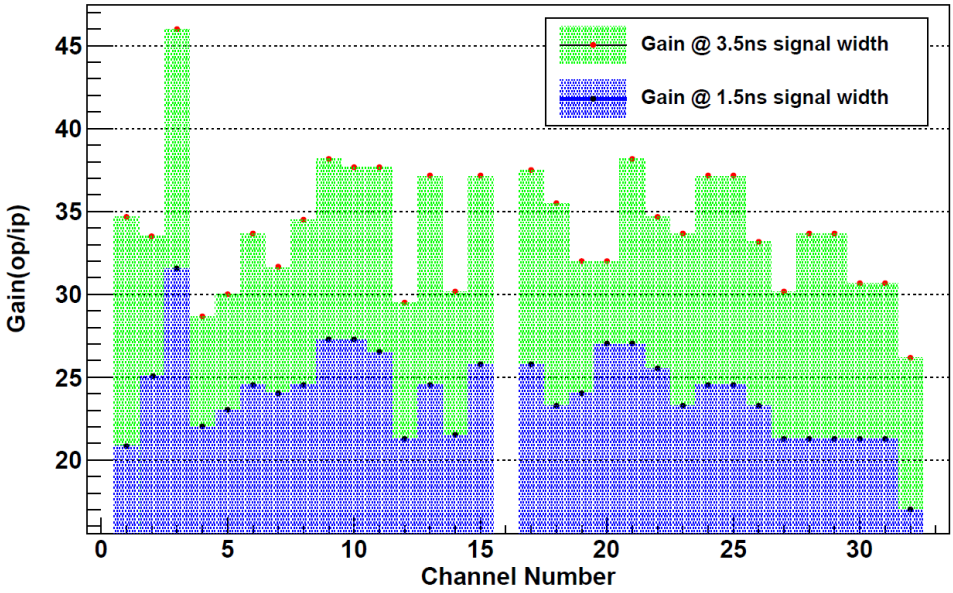

Figure 3.11: Gain (ratio of output(op) to the input(ip)) of the amplifer as a function of channel numbers showing the effect width of the input signal.

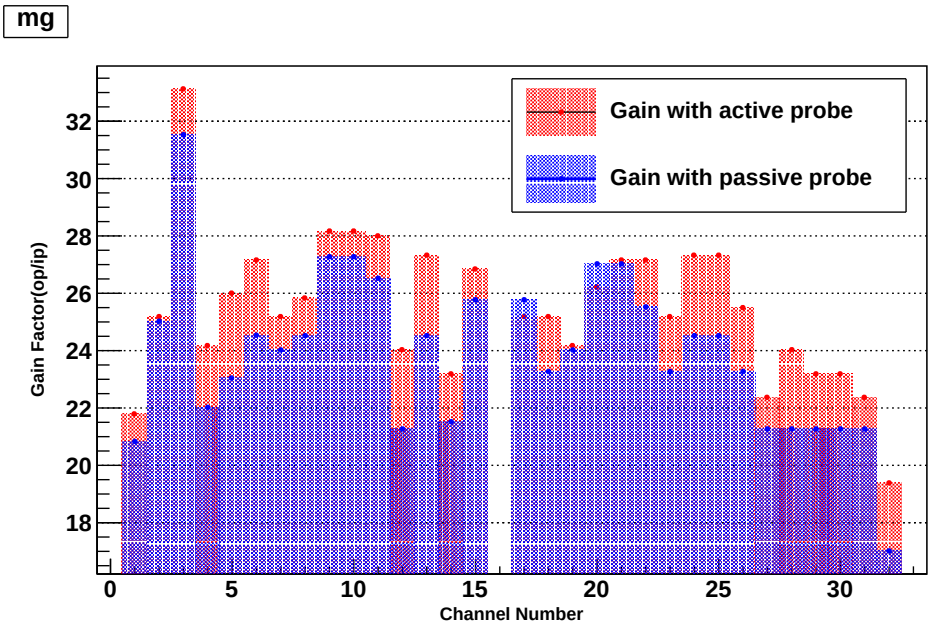

Figure 3.12: Gain (ratio of output(op) to the input(ip)) of the amplifer as a function of channel numbers showing the effect of using active or probe for the measurement.

Noise Characteristics: To examine noise characteristics, no input signal was sent to the DiRICH, and the width of the noise band for each channel was measured using an oscilloscope. The noise characteristics observed in the laboratory in Wuppertal are depicted in figure 3.14, along with similar tests conducted by GSI. It demonstrates that some channels had significant noise levels while the majority of channels were stable; these channels were the region on the PCB where the channels overlapped. The problem was with the DiRICH PCB routing, where some channels were not

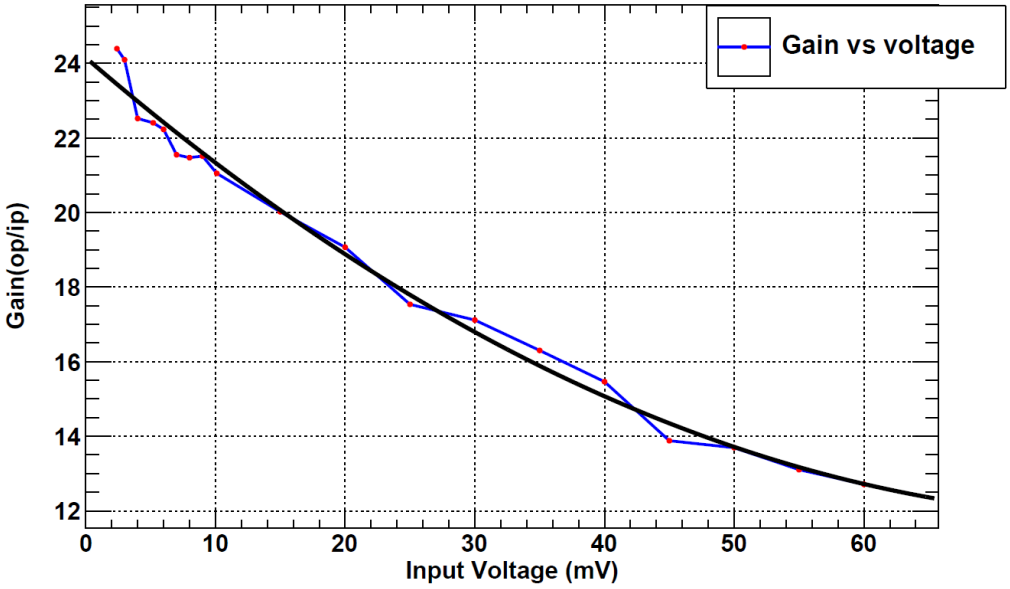

Figure 3.13: Gain (ratio of output to the input) of the preamplifier as a function of the amplitude of the input signal.

adequately isolated; this issue was rectified in second iteration of the DiRICH.

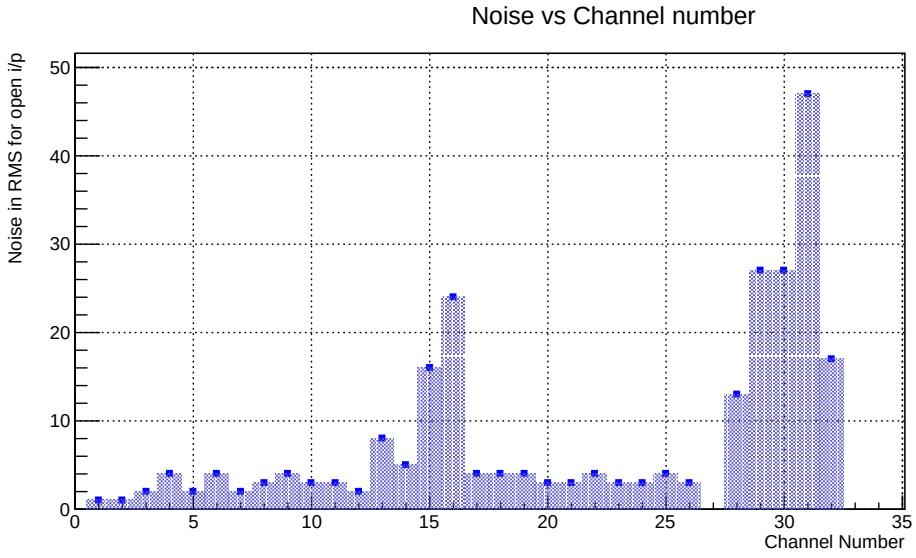

Figure 3.14: Noise response in mV for the preamplifier measured in two different setups.

3.5 Advantages of the DiRICH

DiRICH has several advantages over its predecessors, few of which are:

1. As stated previously, it is compact; one backplane can hold six MAPMTs, offering a great detection surface with minimum dead space. The detection plane for HADES-RICH is a 1.5-meter-diameter circle including 420 MAPMTs, 840 DiRICHs, 74 Power modules, and 74

combiner boards. Consequently, the form factor of the sensor and electronics will significantly influence the number of photons detected, the heat distribution, and the mechanical viability of the installation. The DiRICH readout concept fulfills all of these characteristics.

2. The module features 32 channel amplification, signal discrimination, and TDC, all on the same FEE; this eliminates the need for long cables, which decreases signal distortion. From each backplane, a 2 Gb optical fiber transmits the digitalized output to TRBnet.

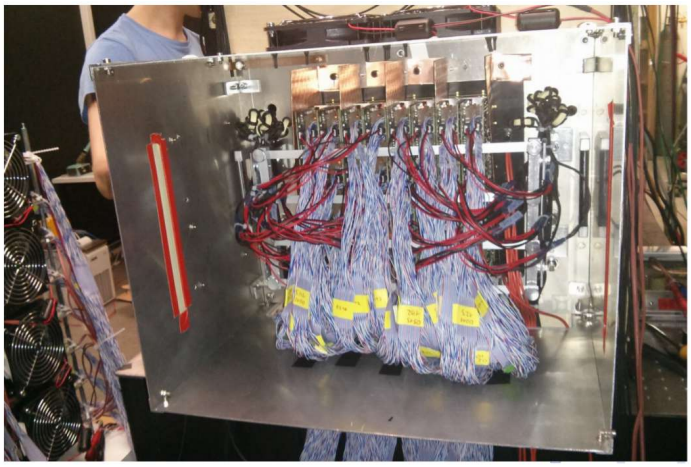

Figure 3.15: Long cable lengths complicate the installation process (left) and also have a detrimental effect on signal quality (right).

3. The MAPMT is directly connected to the DiRICH input (via the intermediate backplane PCB).The same connector that connects the DiRICH to the backplane also links analog input signals from the MAPMT and digital output signals from the FPGA-TDC to the concentrator board. Since no cables are used, there is no possibility of potential deterioration of the signal quality. The effect of longer cable connections can be observed in early beam tests using the padiwa readout electronics. Examples are shown in figure 3.15 and figure 3.16.

4. Since the MAPMTs are galvanically isolated from the FEE by means of transformers, HV-power and supply ground-related issues are minimized.

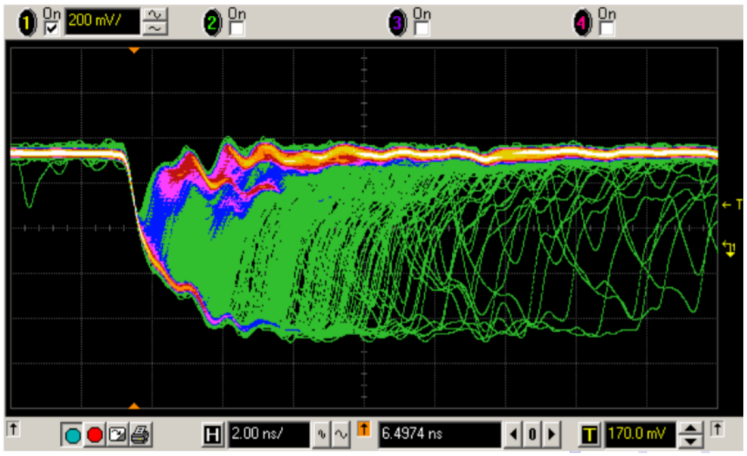

Figure 3.16: Effect on the signal quality due to long cable lenghts (multiple peaks due to different signal arrival time) and ground related issues (distorted baseline) demonstrated on an oscilloscope.

4 Quality assuarnace tests for MAPMTs

Once the MAPMTs arrived, they were subjected to a number of tests. As part of the final installation in HADES, it was decided to coat certain MAPMTs with a wavelength-shifting (WLS) coating. This chapter details the absolute quantum efficiency of these MAPMTs as well as additional tests performed to determine if each MAPMT is suitable for installation in the RICH detectors. These tests include measuring the dark rate as a function of temperature and determining whether iso-butane as a radiator gas has an influence on the photocathode and WLS coating.

4.1 Quantum Efficiency tests

4.1.0.1 Experimental Motivation

As described in the preceding chapter, the HADES detector was to be upgraded using H12700 MAPMTs from Hamamatsu as a photon sensor and the DiRICH readout electronics. As stated in Appendix A, each MAMPMT must have a quantum efficiency of 25% in the visible spectrum, with a maximum efficiency between 350 nm and 400 nm. The spectral response of MAPMTS was tested relative to a calibrated photodiode to confirm this. Following is a discussion of the setup and test procedures of this experiment.

Setup details: The apparatus is mounted on an optical bench to minimize stability-related errors. The test bench is a black-painted box that has been made as light-tight as possible so that no stray light can enter. The mounts for MAPMT and other electronic components are housed within the box. Figure 4.1 depicts all the components of the test setup.

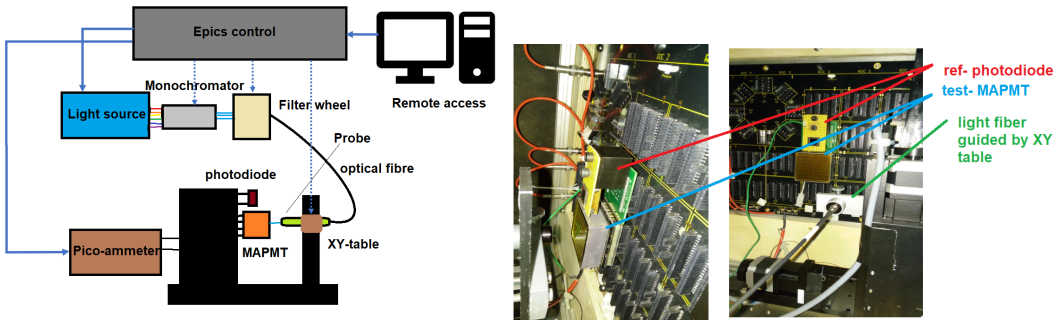

Figure 4.1: The setup for measuring the absolute quantum efficiency of the photon sensor (left) and the actual setup with all the components are depicted in a schematic diagram (right).

- **Light source:** The light source used in this set up provides the spectrum ranging from 180 nm to 800 nm. It uses a deuterium lamp for 180 to 350 nm wavelengths, and from 350 nm onwards, it uses a tungsten filament lamp. The outgoing light is homogeneous and is guided through the setup by a monochromator, a filter wheel, and an optical fibre attached to a probe that collimates the light into 1 mm-diameter circular spot.
- **Monochromator:** The monochromator is a diffraction grating that, when instructed by the user via EPICS, can select a specific wavelength. Thus, it is possible to select a specific wavelength while rejecting all other components of the light source's spectrum.
- **Filter wheel:** The monochromator's output light still contains some higher order wavelengths, which are then blocked by the filter wheel. This two-fold filtering ensures that only one wavelength (400 nm in this case) of light reaches the sensor.

- **Light Fibre:** At the end of the optical fiber is a collimator that creates a small spot on the MAPMT surface. The plan is to expose only one MAMPT pixel to light.
- **XY Table:** The light fiber is mounted on the moving mechanism, which can move it to the desired location on the MAPMT surface. This system can move horizontally and vertically, and its motion can be precisely controlled by a stepper motor.
- **Reference diode:** The PMT mount is equipped with two holders, one for the subject MPAMT and the other for the reference photodiode. This photodiode has already been calibrated. A picoampere meter can be used to measure the current generated by the diode and PMT.
- **EPICS system:** The entire system, including the XY-table, can be controlled remotely via EPICS. Thus, measurements may be easily performed in the darkroom without upsetting the arrangement.

4.1.1 Experimental process

The setup works as follows:

- In order to determine the absolute quantum efficiency of the MAPMT, the direct photocurrent of the MAPMT is measured. To do this, the photocathode -K is separated from the amplification chain (Fig. 4.2). The photocurrent generated by the photocathode is in the nano ampere range. As depicted in figure 4.2, the photocathode is connected to the dynode chain via a resistor (shown as R21), which amplifies the photocurrent. This resistor has a high value of $1M\Omega$, which draws a high current in addition to the small value of the photocurrent. In order to measure the photocurrent, a voltage has to be applied between photocathode K and dynode D1, this voltage causes an additional Current from K via R21, R1 and R2, which is orders of magnitude larger than the actual photo current. Thus, the measured current will not precisely reflect the photocathode's response. To avoid this issue, this high-value resistor (R21) is removed, thereby disconnecting the dynode chain. The image below depicts the circuit diagram and position of the resistor on MAPMT.

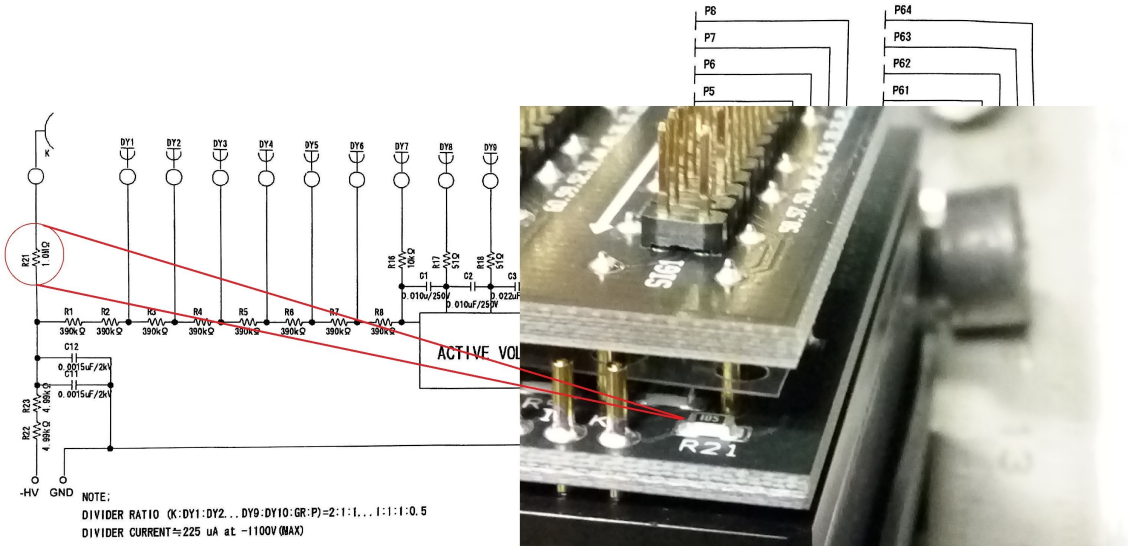

Figure 4.2: Circuit diagram of the dynode chain for H12700 MAPMT and the actual location of same resistor on MAPMT (zoomed image).

- As indicated in the schematics (Fig. 4.1), the MAPMT is attached to the setup alongside the photodiode. The cathode is connected to a high-voltage source, and the ground terminal is

connected to the first three dynodes. -125 V is sufficient to activate the MAPMT-photocathode and generate photocurrent.

- The XY-table guides the light probe to the desired place on the MAPMT or reference diode. First, the photocurrent of the reference diode is measured and saved as the variable I_{diode} in a text file. Next, the photocurrent of the MAPMT is measured and saved as the variable I_{MAPMT}. After measurements, the QE of MAPMT can be determined using the following formula, where $diode_{efficiencyfactor}$ is the manufacturer-provided QE of the photo-diode for a given wavelength.

$$QE_{MAPMT} = \frac{I_{MAPMT}}{I_{diode}} \times diode_{efficiencyfactor}$$

- The setup can perform two types of tests discussed in next sections:
  i) Wavelength scan
  ii) XY-Scan

4.2 Wavelength scan

This scan provides data regarding the MAPMT's response to exposure to different wavelengths. The MAPMTs are exposed to the entire spectrum of wavelengths from 180 nm (minimum) to 800 nm (maximum) in 10 nm increments for this scan. For each scan, three pixels are selected along the diagonal line of the MAPMT (top-right, center, and bottom-left). For each pixel, the fiber is moved to its position by EPICS-controlled XY-table commands (Fig. 4.3).

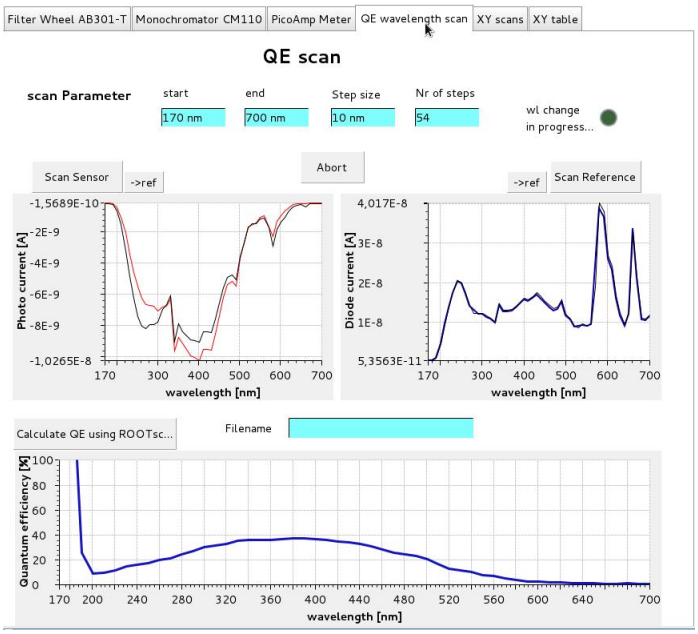

Figure 4.3: EPICS interface showing all the important parameters for the wavelength scan.

The MAPMT and reference diode coordinates are estimated empirically. The light fibre is initially steered onto the reference diode. As demonstrated in figure 4.3, the wavelength values are entered before the scan commences. During each step, the pico-ammeter records the photocurrent from the diode and stores the value in a text file for a specific wavelength value. After the reference diode scan is complete, the light fibre is guided onto the MAPMT, and the same process is repeated for MAPMTs - a pico amperemeter records the photocurrent produced during each scan, and the measurements are stored in a file for subsequent analysis. As depicted in the figure 4.4, this procedure is performed for three distinct MAPMT pixels.

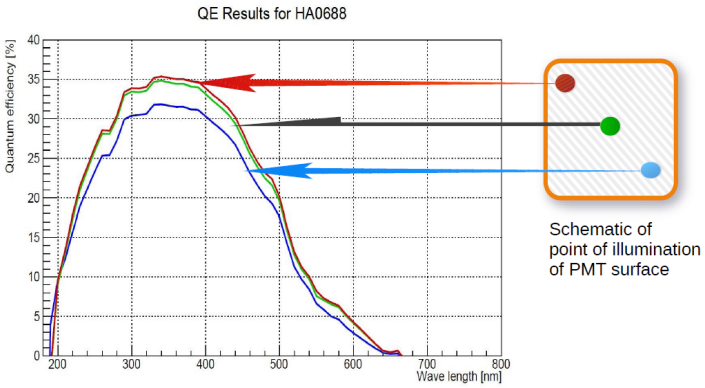

Figure 4.4: A typical plot for wavelength scan showing QE of a sample MAPMT as a function of wavelength. The orange square on the right shows the MAPMT surface with three different points of illumination represented by the three colors in the graph.

4.2.1 Results

Figure 4.5 shows the wavelength scan of four different MAPMTS. The three colours in each plot indicate the three different points of illumination, as discussed above. As one can see from the plots, the distribution of the quantum efficiency is not uniform for each point of illumination for a given wavelength value, indicating a skewness in the photocathode efficiency distribution. The homogeneity of the photocathode along the MAPMT surface should not differ by 25% between the two points [Appendix-A]. Thus the MAPMTs shown in figure 4.5 were good enough to be installed in HADES/CBM since the difference between the red curve and the blue curve is not more than 25%. During the initial time of delivery, a sample of MAPMTs from each delivery batch were examined

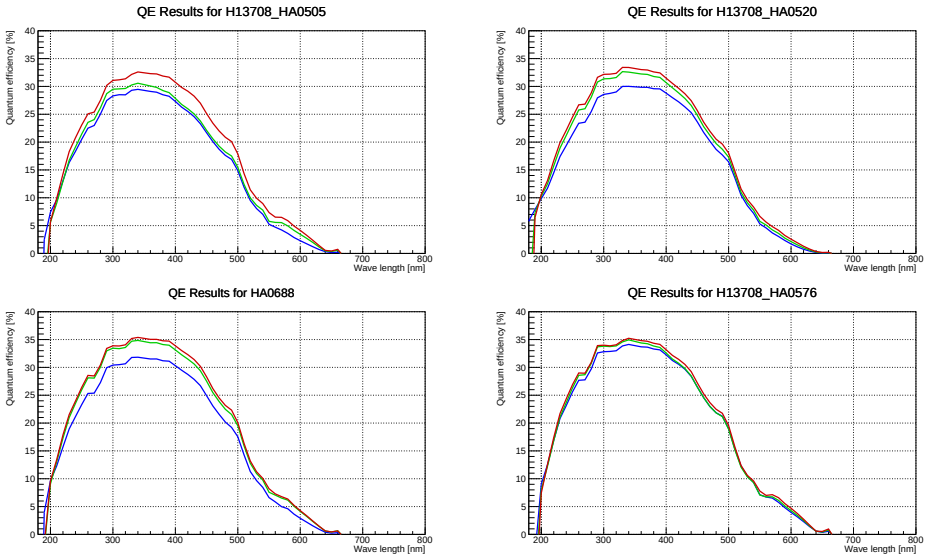

Figure 4.5: Wavelength scan results of 4 different MAPMTs. Red, Green and Blue colors represent different point of illumination.

for wavelength scan and XY scan (discussed in the next section). The graph depicts the wavelength test of all MAPMTs over this time period. One can see that the skewness in the photocathode distribution, while not a deal-breaker, was undoubtedly a characteristic of the MAPMT manufacturing process, which was communicated to Hamamatsu, and subsequent batches had minor issues.

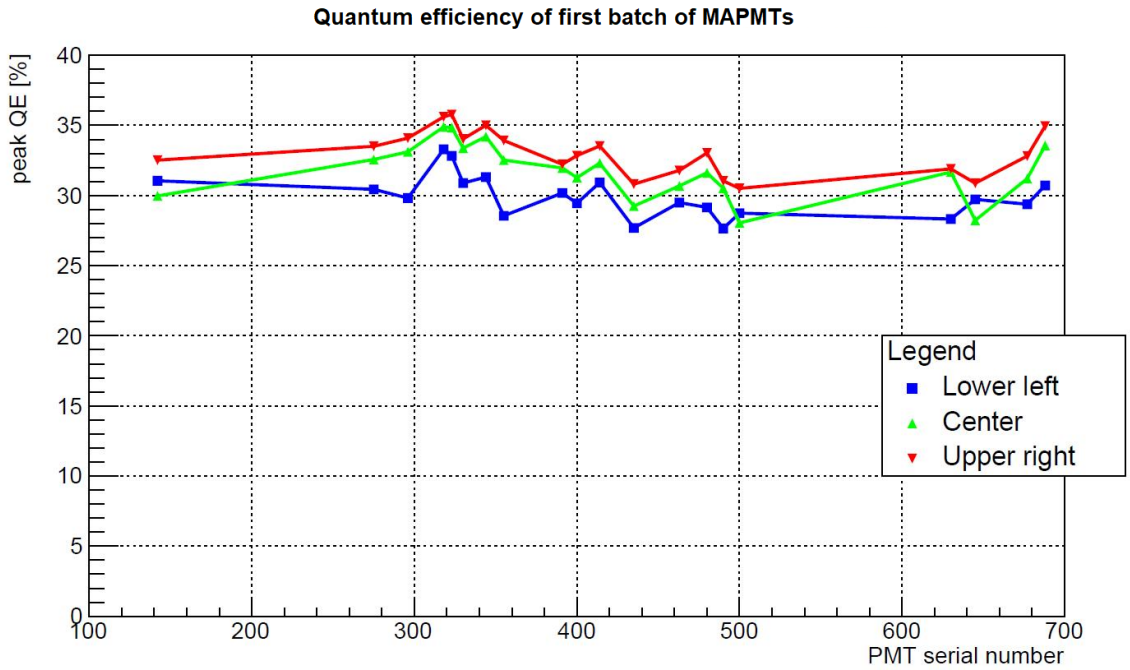

Figure 4.6: Wavelength scan of 20 MAPMTs, randomly selected from each batch of the initial deliveries.

4.2.2 Advantages

This scan provides an overview of the MAPMT response at all wavelengths. The test is simple to do and provides some of the most essential characteristics of the MAPMT, including the peak quantum efficiency for a given wavelength and the skewness of the photocathode distribution on the MAPMT. Along with the XY-scan, this test performed an important part in determining whether the MAPMT is suitable for installation in the main experiment.

4.2.3 XY-Scan

XY-scan helps to determine how uniform the photocathode is across the MAPMT surface. This test can be conducted using the identical equipment as wavelength scans. The primary distinction between the two scans is: In the wavelength scan, QE is measured as a function of wavelength, whereas in the XY scan, QE is measured as a function of illumination position for a particular fixed wavelength. Consequently, XY-scan is a 2D representation of QE over the MAPMT region. This test provides detailed information regarding the photocathode's surface profile, homogeneity in a more quantitative sense, and photocathode imperfections.

For this scan, the MAPMT is illuminated with a wavelength corresponding to its maximum quantum efficiency. In this case, 400 nanometers. First, similar to wavelength scans, the response from the reference diode is measured. The light fiber is steered onto the diode using the EPICS setup depicted in figure 4.7, and the photocurrent is measured and saved in a text file. Next, the light fiber sweeps through the entire MAPMT surface, illuminating one pixel at a time while measuring the photocurrent. In this manner, the entire surface of MAMPT is scanned, the response is recorded in terms of photocurrent measured using a pico ampere-meter, and the coordinates and corresponding QE of each pixel are recorded. It takes approximately 6-7 hours to complete one MAPMT depending on resolution of the scan, which is a time-intensive process.

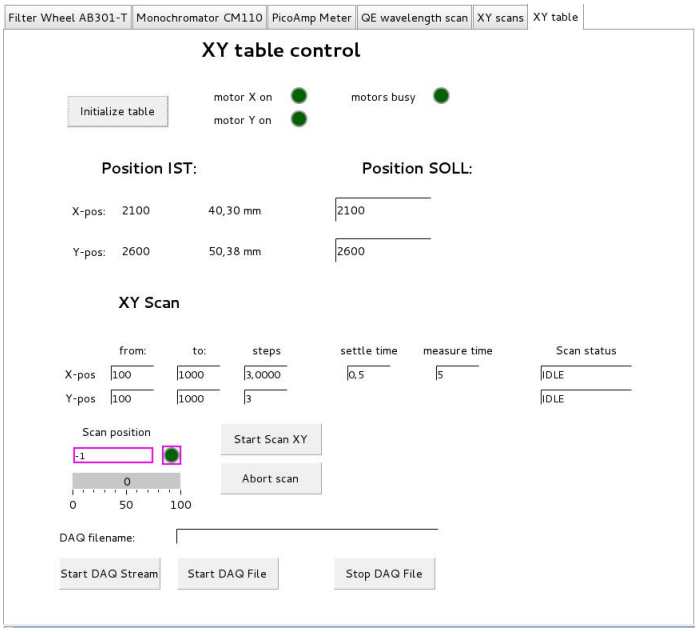

Figure 4.7: EPICS interface showing all important parameters for the XY-scan.

4.2.4 Results

Figure 4.8 illustrates a standard XY-scan plot. It consists of three plots, with the left plot displaying the QE distribution on the MAPMT surface. The two grey plots depict the quantum efficiency in the horizontal and vertical planes as X and Y projections, respectively. The color scale reflects the absolute quantum efficiency value, while X and Y projections reveal the skewness in the photocathode distribution. According to the graph, the MAPMT has a good distribution of QE across its surface and a significantly smaller amount of skewness. Therefore, this MAPMT is appropriate for use in HADES/CBM experiments.

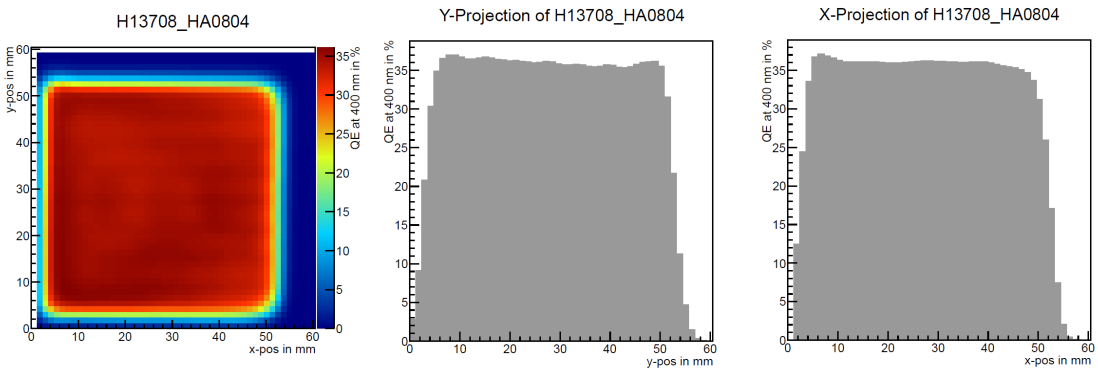

Figure 4.8: A typical plot for XY scan showing QE of a sample MAPMT as a function of position of illumination.

Not all MAPMTs are manufactured with this precision, and by this test, one can easily spot the errors in the manufacturing process in the area of photocathode distribution.

Upon XY scan testing, these MAPMTs displayed a variety of artifacts. The most significant result is depicted in the figure 4.9. It is obvious from these graphs that either the photocathode was damaged or improper material deposition occurred. Regardless, these MAPMTs were replaced

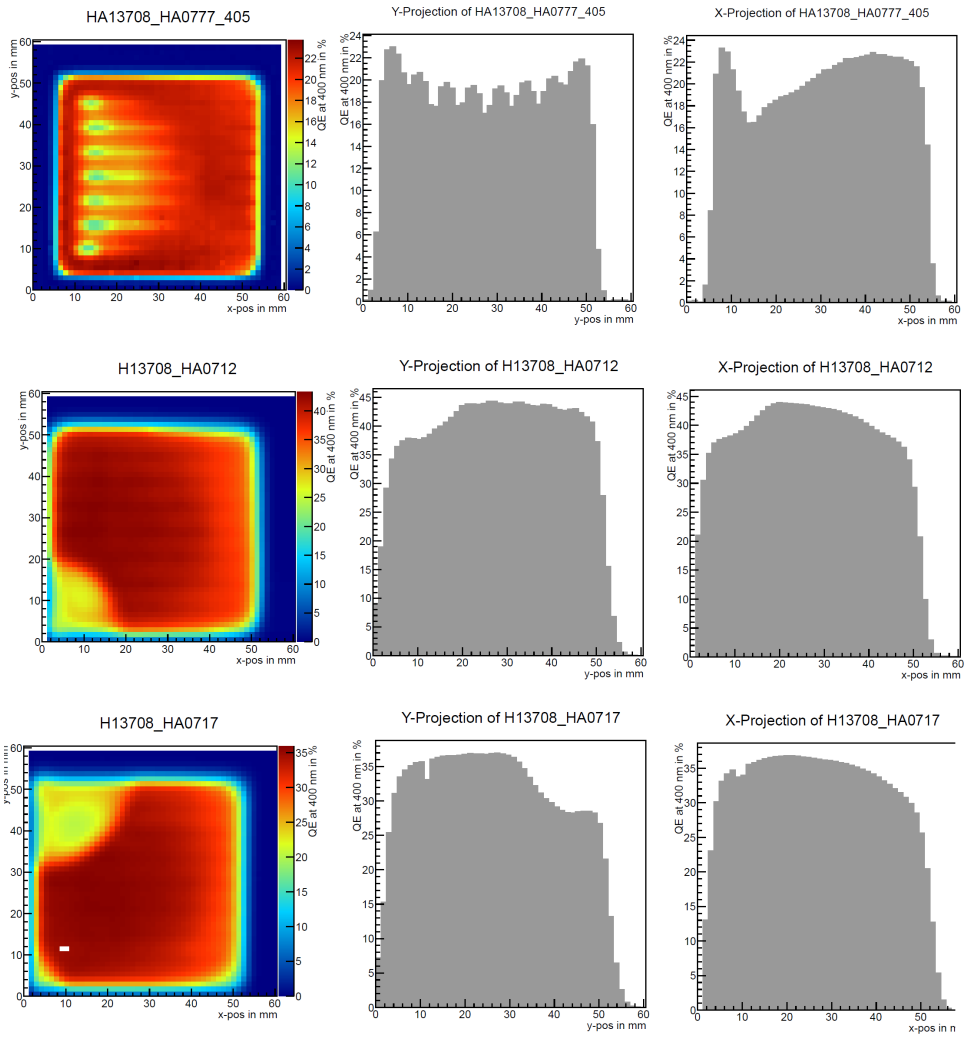

Figure 4.9: XY-scan for the faulty MAMPTs.

since they were unsuitable for the final installation in the main experiment. It is also interesting that these flaws were solely associated with the photocathode, as the dynode chain was disconnected during the tests and the pure photocathode response was recorded. These messages were conveyed to Hamamatsu, and they replaced MAPMTs.

The XY-scan and wavelength scan were essential in improving the MAPMT's quality. These tests are also useful for other applications, as described in the sections that follow.

4.3 Applications of QE tests

4.3.1 Wavelength shifting coating

For a photon sensor to reach its maximum potential, its spectral sensitivity must cover a broad range of wavelengths in the electromagnetic spectrum (preferably from ultraviolet to visible). 200–600 nm is the spectral sensitivity range of the H12700 MAPMTs that will be used in the HADES and CBM experiments. As described in chapter 2, the MAPMTs are equipped with a bialkali photocathode with an extended UV window and a peak quantum efficiency at approxi-

mately 400 nm. The photocathode material restricts its spectrum response for wavelengths >600 nm because the photon energy is insufficient to overcome the work function of the bialkali photocathode. For <200, the entrance window's transparency reduces the number of UV photons, hence affecting the spectral sensitivity (≈300 nm for glass, ≈220 nm for UV-extended glass, and 180 nm for quartz). The low-wavelength region is significant because it improves the Cherenkov photon yield, and acquiring a few additional photons will always be advantageous for the reconstruction of the ring (as long as the loss in spatial resolution due to chromatic dispersion at shorter wavelengths is acceptable). This is paired with the fact that the radiator gas provides a short-wavelength cutoff; in the CBM experiment, the radiator gas is CO_2, which has a cutoff of 185 nm. Coating the outer side of the entrance window with a Wavelength Shifting (WLS) film is one technique to increase the MAPMT's spectral responsiveness in the low-wavelength region [EL79].

WLS films are organic chemical coatings with the ability to absorb UV light and release it back into visible regions, ideally within the spectral sensitivity range of the photocathode material in use. Garwin et al. [EL79] proposed the WLS approach for PMTs with ordinary glass windows used in gaseous Cherenkov detectors in 1973. An earlier work shown that WLS films are likewise applicable to MAPMTs and that the 4π emission of the fluorescence photons has a negligible impact on resolution. In addition, when employing WLS films on MAPMTs with segmented anode and dynode architectures, crosstalk between neighboring pixels due to the isotropic fluorescence of the WLS films must be taken into account. As a WLS molecule, p-terphenyl is well-suited for H12700 MAPMTs. During a test beam at the COSY accelerator, the performance of p-terphenyl-coated H12700 MAPMTs was measured. Chapter 6 discusses this in detail.

4.3.1.1 Results

Several MAPMTs were coated with WLS films and evaluated in wavelength and XY-scan test sets. The objective was to identify any change in quantum efficiency or other effects caused by WLS on the performance of the MAPMT. The wavelength and XY scans were merely preliminary experiments; afterwards, additional tests were conducted with the actual beam at the COSY accelerator. Despite this, QE test scans provided the initial understanding of WLS coating.

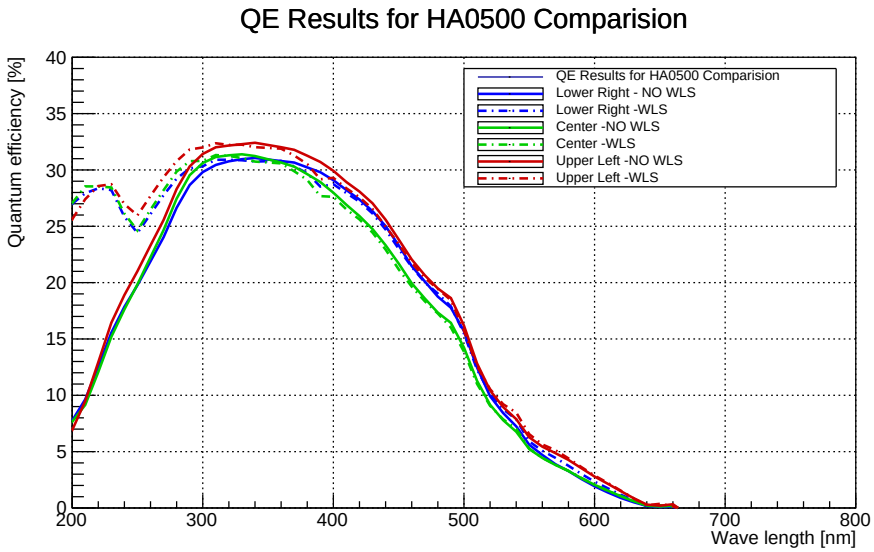

Figure 4.10: Wavelength scan of a MAPMT with WLS coating. The solid lines show the WS before applying WLS film and the dashed lines shows the WS after the coating.

Figure 4.10 represents the wavelength scan of a MAPMT with WLS film coating. The three colors represent the three separate lighting points: red for the upper left pixel, green for the center pixel, and blue for the lower left pixel. In the plot, the solid lines represent the wavelength scan

prior to coating, whereas the dashed lines represent the wavelength scan after coating. WLS coating was used to increase photon yield in the near UV range. Before the WLS was applied, the QE in the low wavelength region, between 200 nm and 250 nm, was below 15% (solid lines). The same MAPMT with WLS coating has a QE of 29% at 220 nm, which is 15% greater than the QE at the same wavelength without WLS coating.

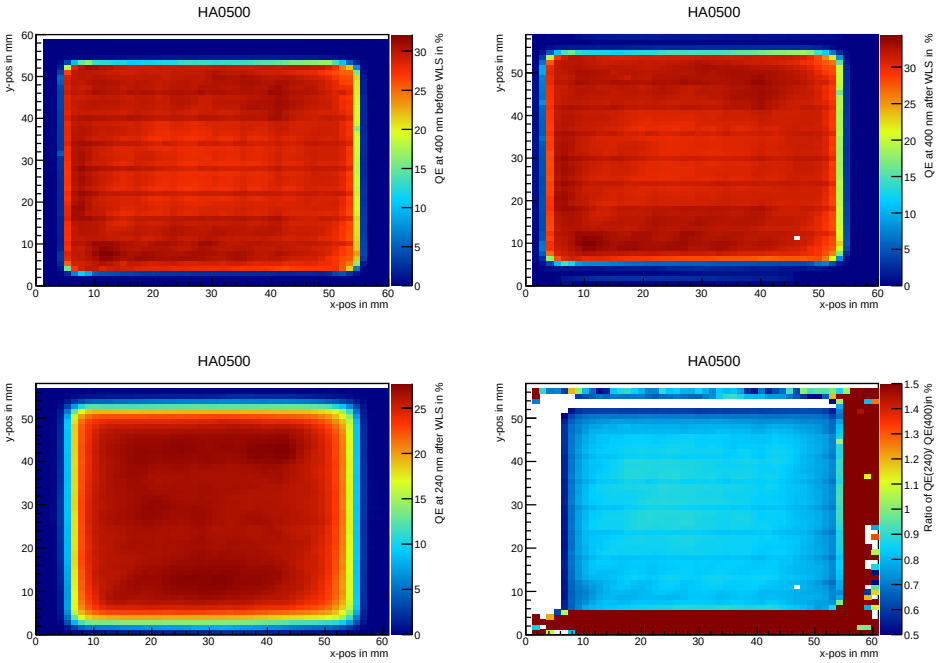

Figure 4.11: XY-scan of a MAPMT for exposure at 240 nm and 400 nm wavelengths. The last plot is the ratio of the QEs at 240 nm and 400 nm showing the possible effect of WLS on the spectral sensitivity of the MAPMT.

Thus, it is validated that applying a WLS coating to the MAPMT improves the QE in the low wavelength region. However, it remains to be determined if the coating layer is sufficiently thin to permit visible light and, consequently, does not affect the QE performance in its normal spectral sensitivity range. To confirm this, the XY scan of the same MAPMT is performed at two distinct wavelengths, 240 nm and 400 nm, and the ratios of these plots are then calculated. Figure 4.11 illustrates the XY scan of HA0500 MAPMT's QE profile.
- The upper-left plot represents QE at 400 nm prior to coating
- The upper-right plot represents QE at 400 nm after the WLS coating.
- QE at 240 nm after WLS coating is shown in the bottom-left plot.
- The bottom-right graph represents the ratio between QE @ 240 nm and QE @ 400nm (second and third plots).

The following conclusions may be drawn from these plots:
- The QE at 400 nm is unaffected by the WLS coating, demonstrating that the WLS has no effect on the visible-range spectral sensitivity of the MAPMT.
- The QE at 240 nm is sufficient and will contribute positively to the photon yield performance of MAPMT.
- The ratio figure illustrates the shift in MAPMT QEs as a result of WLS. Again, this demonstrates that the WLS coating has no negative impact on the MAPMT's spectrum sensitivity range.

4.3.2 Beam test preparation

Once the MAPMTs and readouts were available and tested for manufacturing quality, they were tested under real beam conditions at the COSY accelerator in Julich. The performance of the WLS coating under real beam conditions and its effect on the time resolution was a test parameter. Prior to putting WLS-coated MAPMTs in the COSY beam test setup, they were evaluated for quality assurance utilizing a wavelength test and XY scan. Six MAPMTs were chosen for installation based on the findings of the wavelength scan, which are depicted in the following graphs.

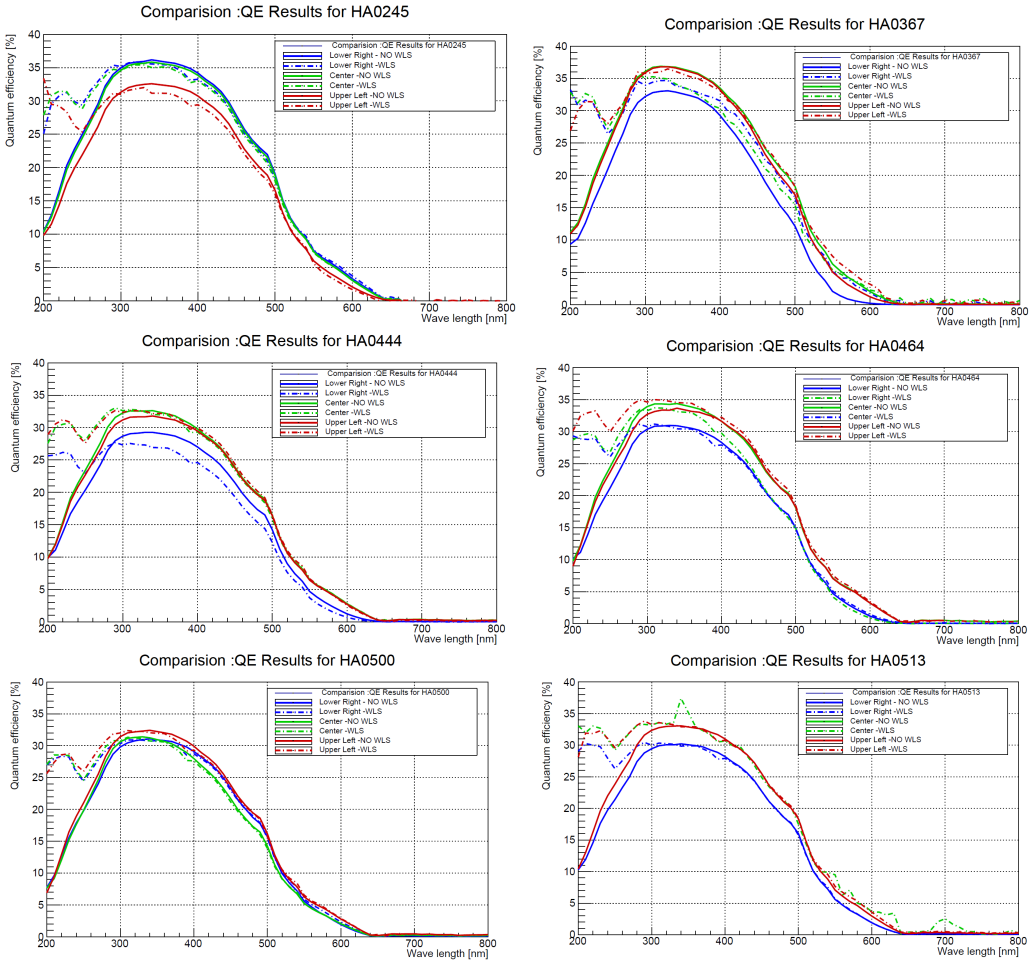

Figure 4.12: Wavelength scan of WLS coated MAPMTs used for beam test at COSY accelerator, Jülich.

4.3.3 Aging tests

The HADES detector was equipped with H12700 MAPMTs and DiRICH readouts in the second half of 2018. In consideration of the new photon sensors, the HADES radiator was changed to iso-butane after initial testing. Before installing MAPMTs, it was required to determine whether the radiator corroded the MAPMTs, particularly the photocathode and WLS coating during long-term exposure. Consequently, three MAPMTs were taken for the iso-butane test. One was the reference MAPMT (HA1051), second was the WLS-coated MAPMT (HA1782), and the third was an uncoated MAPMT (HA0500). The reference MAPMT (HA1051) was not kept in the gas , while the other two MAPMTS (HA0500 & HA1782) were kept in gas for observation. This process ensured that any systematic error in the setup could be rectified if it occurred. Before putting any MAPMT to the

test, wavelength-QE tests were conducted on all MAPMTs. After the tests, they were stored in a vacuum-sealed jar with a steady flow of isobutane for six months before being removed and put through a QE test.

After six months the MAPMTs were taken out, and their quantum efficiency was tested again in the QE-setup; the results of same the are discussed below.

4.3.3.1 Results

Figure 4.13 displays the wavelength scan test results for the reference MAPMT and the test MAPMT. The solid line in each graph represents the QE before flushing the MAPMT with iso-butane, while the dashed line represents the QE six months after maintaining the test MAPMT in iso-butane. Even after six months, the wavelength scan of the reference MAPMT reveals that the QE test setup was functioning properly and that there were no systematic errors. The wavelength scans for the test MAPMT are likewise identical, demonstrating that the radiator gas has no substantial impact on the photocathode properties and WLS coating of HA1782. Similar results were obtained for HA0500 showing no effect of isobutane exposure.

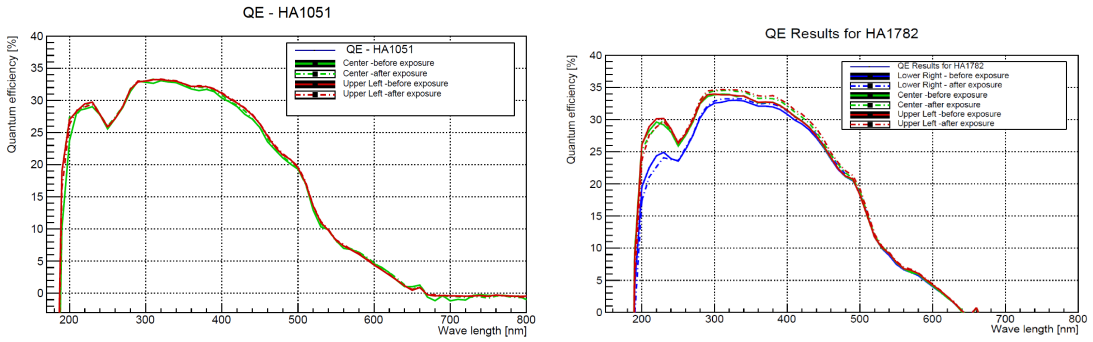

Figure 4.13: Wavelength scan of the reference MAPMT (HA1051) and the test MAPMT flushed with iso-butane (HA1782). Solid line shows the effec before the exposure and dotted line shows the effect after the exposure.

4.4 Temperature tests

One of the prime tasks of the laboratory at the University of Wuppertal is to conduct quality control testing on all MAPMTs supplied by Hamamatsu. Since the fall of 2015, these tests have been performed on each shipment. The measured parameters were compared to Hamamatsu-agreed-upon requirements. The majority of MAPMTs that did not meet the criterion had an unusual dark rate per pixel. According to the specifications, the dark rate per pixel must be lower than 3 kHz per pixel [Appendix A]. The MAPMTs that did not meet these criteria had a dark rate more than 3 kHz, despite the fact that the MAPMTs specification charts indicated a much lower number. Seasonal variations in the laboratory's ambient temperature resulted in varying dark rate results during the experiments. Nevertheless, with active temperature control in our setup, we were able to quantify this effect. Given the requirement for cooling efforts later in the experiment, a thorough comprehension of the PMTs' temperature behavior is essential. The permitted level of dark rate per MAPMT is 6.4 kHz; the MAPMT is returned to the manufacturer if the dark noise exceeds this threshold during the QC tests.

4.4.1 Experimental setup

A climate chamber was utilized to examine the temperature dependence of dark rate. It offers automated temperature regulation for multiple settings. The MAPMT is mounted on a backplane

with n-XYTER readouts such that the MAPMTs were inside the climate chamber and was subject to the temperature settings, while the n-XYTER was outside, attached to a water cooling system that maintained its temperature at 22 °C.The temperature in the climate chamber is maintained at one level for three hours before increasing to the next level in two minutes. This was done to allow MAPMT some time to reach equilibrium with the surrounding temperature. Outside of the climatic chamber, n-XYTER cards were used to monitor the dark rate. This ensured that the n-XYTER does not contribute to noise increase, and only the MAPMT's contribution is recorded. During one set of temperatures, the n-XYTER would collect data at thresholds ranging from 30 to 100 mv in 10-point increments every 15 minutes. This setup can achieve temperatures as low as 10 °C, although the MAPMT data sheet specifies a maximum of 40 °C, which was the upper limit of the temperature in this setup. One MAPMT required between 36 and 40 hours to complete. The complete setup can be operated remotely as the climate chamber could be controlled via a computer (figure 4.14).

4.4.1.1 Results

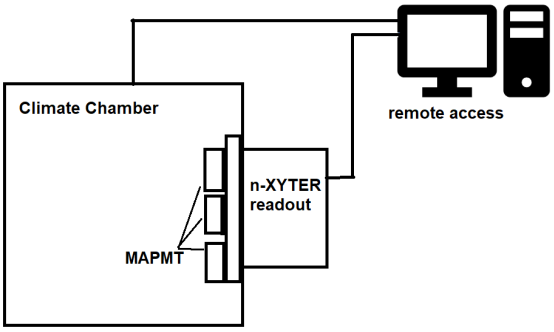

Figure 4.14: Schematic diagram of a MAPMT signal showing main signal (blue) and signal from the second dynode (green).

Figure 4.16 illustrates the exponential growth in the dark rate of a MAPMT as the temperature changes. As the temperature rises above 30°C, this becomes a serious concern. According to the H12700 data sheet, temperatures exceeding 50°C might have a negative impact on performance and harm the MAPMT. The higher dark rate may also have an impact on the performance of the readout electronics, since the detector will emit unwanted noise that will require additional effort to eliminate. The graph in figure 4.16 reveals that the dark rates increase exponentially soon after 30°C. Given the high-rate nature of the experiment in HADES and CBM, these dark rates may pose a significant problem during data collection. Keeping the ambient temperature of the detector as low as possible is beneficial for the HADES (and CBM) experiments.

Figure 4.15 depicts the time evolution of the dark rate at various temperatures and ADC thresholds, with each temperature and threshold represented by a different color. The upper graph depicts the evolution of ambient temperature with respect to time in minutes, while the lower graph depicts the evolution of the dark rate measured in terms of frequency at ADC. The graph demonstrates that the dark rate of a MAPMT has a strong correlation with the change in temperature. Quantifying this correlation was the primary objective of this experiment. Three MAPMTs were evaluated for examining the temperature-dependent behavior of the dark rate.

The derivation of an analytical description of the dark rate for the H12700 MAPMTs is an important outcome of this study. This allows us to extrapolate the dark rate at room temperature (or extrapolate to any temperature). Due to the fact that we examine many other characteristics of these MAPMTs in a separate setting, this relation is implemented there to assert dark rate-related MAPMT failures with sufficient proofs. The dark rate temperature dependency of the PMT is exponential and can be expressed as follows:

$$Darkrate(T) = Darkrate(T0) \times e^{(\lambda \cdot (T - T_0))}$$

where T0 is the reference temperature and (T-T0) is the temperature difference between the dark rate to be extrapolated and the reference temperature. In these studies, λ is the exponential coefficient that has been empirically validated. It has been validated for three distinct MAPMTs and determined to be the same for all MAPMTs, although the dark rate at room temperature differs significantly between MAPMTs.

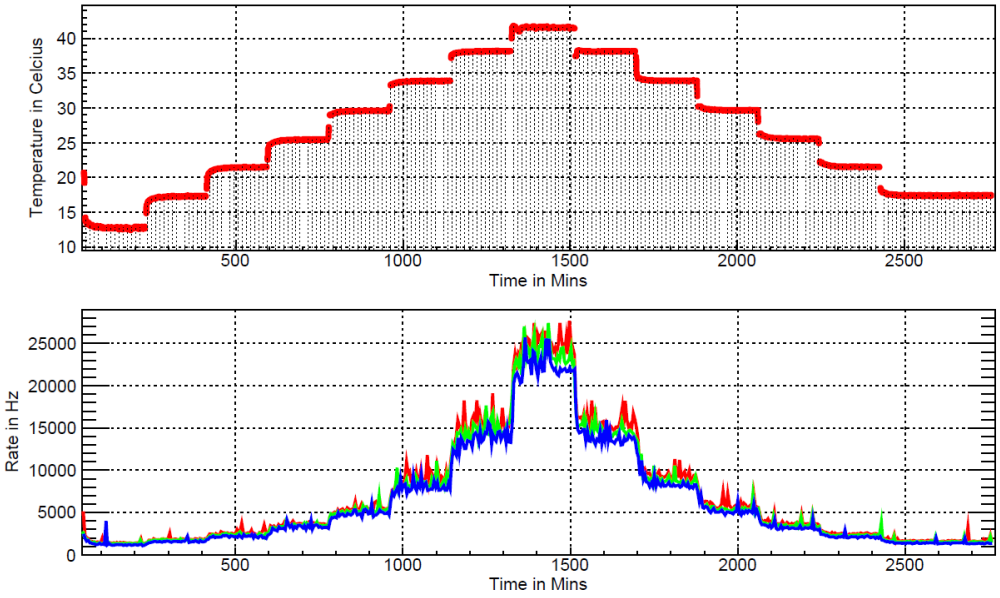

Figure 4.15: Time evolution of the temperature in the climate chamber and corresponding change of dark rate in the MAPMT at three different thresholds at ADC shown in three different colors.

Table 4.1: Comparision of measured and extrapolated rates

PMT Number	**Rate(Hz) @ Temp(°C)**	**Rate(Hz) @ Temp(°C)**	**Decay Const. λ**	**Extrapolated Rate(Hz)**
HA0150	494 @ 22.96	1162 @ 29.10	0.139	1097 @ 29.10
HA0151	353 @ 22.96	637 @ 29.10	0.096	784 @ 29.10
HA1089	816 @ 27.06	1213 @ 30.11	0.129	1213 @ 30.11
HA1215	855 @ 27.06	1744 @ 32.69	0.126	1777 @ 32.69
HA1469	1161 @ 20.82	3332 @ 26.05	0.201	2291 @ 26.05

From our results, we conclude that λ has an average value of 0.13; with this value, one can extrapolate the rate values to any temperature. This rate constant has been implemented to calculate the dark rate of MAPMTs in our primary setup, which investigates various MAPMT characteristics. In our current Quality Control tests, we extrapolate the dark rate to 25 degrees, allowing us to make claims on the PMT's performance with Hamamatsu. This value's veracity has been confirmed in our primary configuration, as indicated in the table below. Table 4.1 displays the measured dark rate (columns 2+3) for various PMTs at two different temperatures. Column 4 displays the projected dark rate extrapolated from the first observation (column 2) to the second measurement's temperature (column 3) using exponential extrapolation with λ equal to 0.13. In column 5, the discrepancy between the measurement of the rate at higher temperatures and extrapolation is displayed, confirming the validity of the analytical description.

These investigations provide a comprehensive understanding of the temperature behavior of H12700 MAPMT, which is crucial for determining the cooling and temperature control efforts required for the final detector design. The principal findings can be summed up as follows:

- Strong increase of dark rate with temperature is observed which puts stringent requirements on the operating conditions in the detector. Temperature above 30°C must be avoided in or-

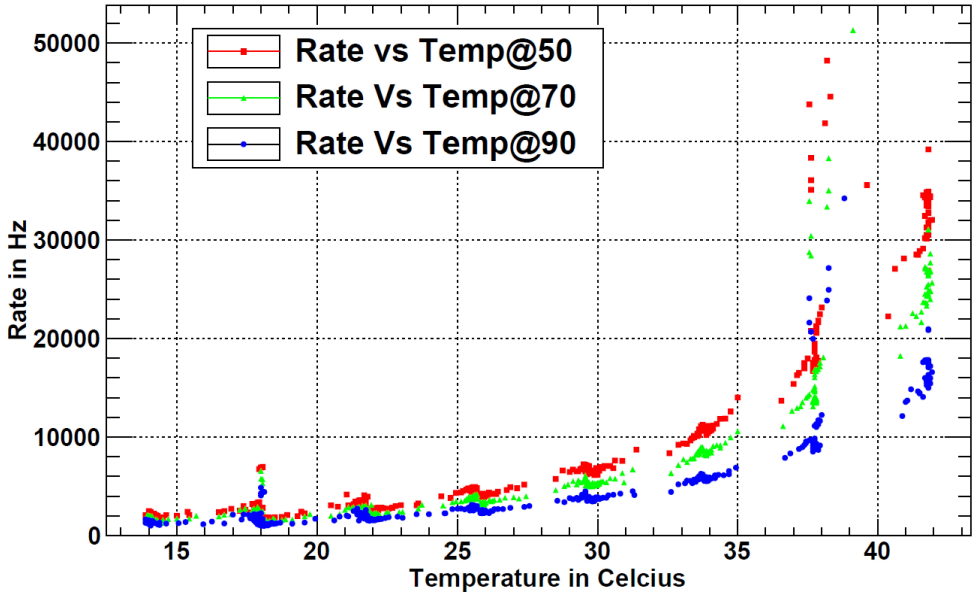

Figure 4.16: Relation between the temperature (°C) and dark rate (Hz) for different thresholds at the ADC (50, 70 and 90 mV) represented in red, green and blue respectively.

der to keep dark rate (and thus data rate of the self-triggered acquisition system) in tolerable levels.

- We reached an agreement with Hamamatsu on a maximum dark rate value of 6 kHz at room (25°C) temperature. To meet this criteria for all PMTs, it is necessary to extrapolate the recorded dark rates to room temperature using the correlation law found in this study. A $\lambda = 0.12$ exponential coefficient may be calculated, allowing for rate extrapolation to room temperature in the PMT QC setup.
- The weak threshold dependency of recorded dark noise rates validates the single-photon character of these noise signals, which cannot be suppressed by merely increasing the threshold. This is also apparent from figure 4.17.

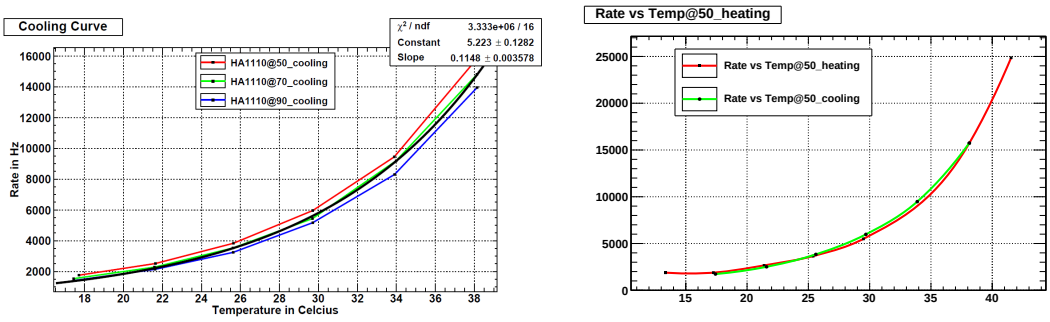

Figure 4.17: Threshold dependence of dark rate (left) and heating and cooling curve showing no evidence of any hysteresis (right).

- Our data in the climate chamber reveal no dark rate hysteresis effects in response to a change in temperature. The dark rate results directly from the actual PMT temperature.

5 DiRICH PERFORMANCE TESTS

This chapter covers the results obtained while testing the DiRICH readout chain in the HADES test box, designed explicitly for DiRICH testing. The testing covers various performance parameters of the DiRICH, such as rate performance, the efficiency of DiRICH, noise parameters and, most importantly, cross-talk suppression and timing precision under laboratory conditions. These tests were done before testing the readout chain under real beam conditions.

The series testing of MAPMTs and the initial prototypes of the DiRICH readout electronics were going without problems. The prototypes were tested in the HADES-test box following the completion of good preliminary testing in Wuppertal. The HADES test box was a cylindrical dark box with the exact dimensions of the HADES-RICH photodetector plane. A diagram of the new HADES-RICH photon detector is depicted in figure 5.1. The detector will consist of about 74 separate readout modules with 6 MAPMTs each. TU Munich constructed a test box to test and commission the new photon detector of the HADES. Thus, the test box facilitates the illumination of individual modules during the testing and, later, will be installed as a fully assembled photon detector. The test setup of the HADES-test box is shown in figure 5.1.

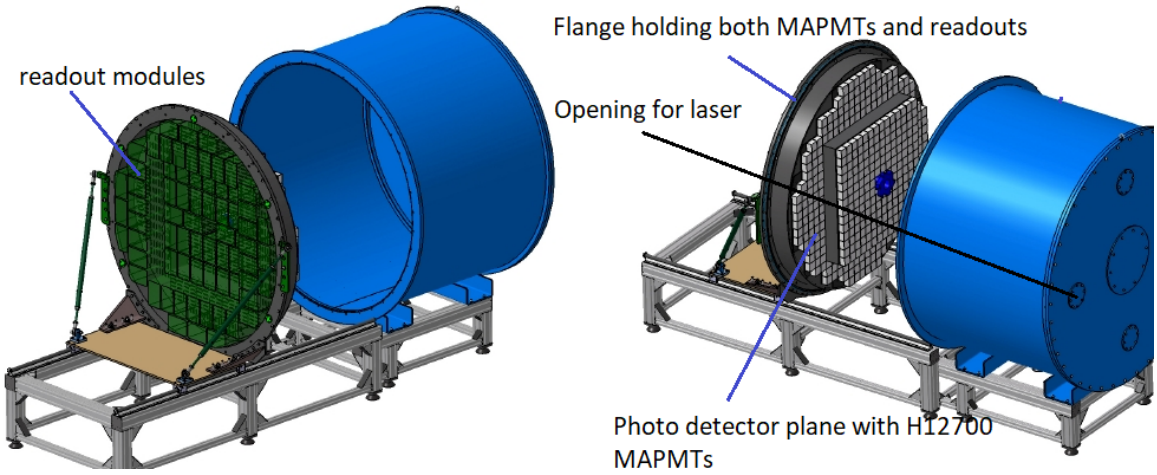

Figure 5.1: Schematic diagram showing all the components of the HADES test box.

5.1 HADES text box

The main components of the HADES test box are:

- **Laser source:** The source is a blue laser (405 nm) capable of producing picosecond long pulses. The intensity and frequency of the laser can be adjusted according to the need.
- **Diffuser:** A light diffuser was attached to the laser output so that a uniform light fell on the MAPMT plane.
- **Photon detection and Readout:** The MAPMT plane is a complete readout module consisting of a backplane with a power module, a combiner module, a DiRICH, and a MAPMT.

The primary objective of HADES test box testing was to investigate the characteristics of the front-end analog input stage of the DiRICH front end module. The parameterization of this input stage has a significant impact on the discrimination and digitization stages, possible efficiency and timing precision. To examine the analog signal portion of the DiRICH front-end module, a digital

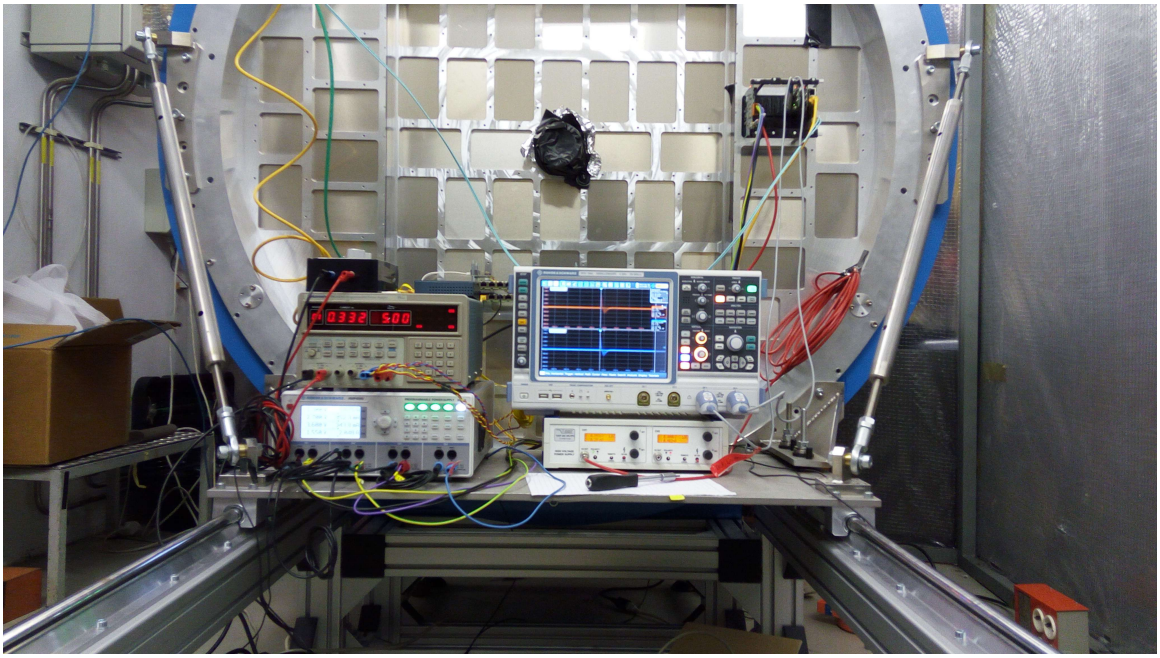

Figure 5.2: Test setup of the HADES test box at GSI with one module installed on right corner of the flange.

oscilloscope with active probes was linked to the output of the two analog amplification stages of the DiRICH front-end module. This simulation of the FPGA TDC functionality was of particular importance, since the actual FPGA design was not yet available at the time of these measurements. Analysis of the digital scope traces allowed to emulate the later TDC (of which the properties were already well defined in terms of timing precision). This configuration allows for the direct visualization of amplified signals prior to their entry into the FPGA for discrimination. In addition, the scope enables continuous sampling of the two channels and storage of the signal trace for offline analysis. Analyzing these data offline allowed us to replicate the FPGA-TDC capabilities with the scope and investigate the impact of the analog component on leading-edge timing precision, time-over-threshold and efficiency, assuming a fully functional FPGA-TDC. However, FPGA architecture was not available when these measurements were conducted. Separating the analog electronic components from the FPGA-TDC aided in comprehending their complex interrelation and optimizing the analog stage settings. The other objectives were as follows:

- To check the signal quality and study its characteristics.
- To test the effect of the intensity of light on the MAPMT and the DiRICH.
- To test the effect of frequency of the laser.
- To test onboard DCDC converters.
- Initial idea on the time resolution of the signal.
- Crosstalk information.
- Feasibility of installation of various components such as voltage crates, grounding, cabling, and cooling in the final assembly.

Photons were generated using a pulsed laser light source (405 nm) at various frequencies up to the megahertz range. Light was diffused to illuminate a broad detector area relatively uniformly using a combination of a unique holographic diffuser and milk glass. The light intensity is reduced to the

single-photon level such that each PMT pixel can only detect a single photon in a small percentage of laser pulses. Therefore, it can be approximated that the light falling on the MAMPT comprises of only single photons.

Figure 5.3 depicts the oscilloscope's image. There are three sections. The first is the laser trigger, the second is the MAPMT signal relative to the laser trigger after preamplification, and the third is the cumulative plot displaying the single photon peak. The huge spike on the left represents noise, while the narrow, broad peak on the right represents the actual single photon peak. One may readily observe that the noise peak and the signal peak are not distinct; they overlap. Therefore, one must understand the overlapping region for optimal noise and signal separation.

Figure 5.3: Screen image on the oscilloscope showing the laser trigger(yellow) in top-left, the signal (green) in top right and the bottom picture showing pulse amplitude spectrum with the narrow noise peak followed by the broad single photon peak (pink).

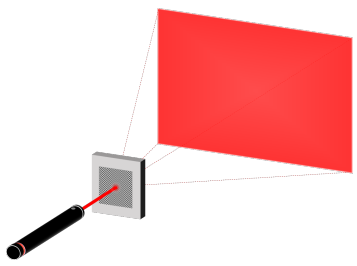

Figure 5.4: Schematic diagram of a laser with a diffuser.

Under realistic conditions, single photons cover the MAPMT in a circular formation within a Cherenkov ring. In the current setup, single photons must be produced to simulate this effect using a laser pulse that is a continuous stream of photons. The laser source used in this test has a hundred-step variable intensity function. It is also possible to use the source as an external trigger. The following method was implemented to receive single photons on MAPMT, simulating the HADES conditions. Figure 5.4 shows schematic diagram of the laser output covered with a calibrated diffuser. This diffuser's dimensions are such that it covers the entire laser beam profile. The diffuser disperses the laser beam over a wide area, ensuring that the laser light illuminates the entire MAPMT area. For the purpose of the tests, the scope was connected to the two channels corresponding to the two pixels of the DiRICH. Thus, for each trigger pulse (yellow curve in figure 5.3), the scope records the number of times a photon hits a pixel under observation (green curve in figure 5.3).

Using this method, it is possible to calculate an approximate number of photons hitting an entire MAPMT plane. Suppose for 100 triggers from the laser; there are 11 detected signals on the CRO. In this setup, at a given time, only one channel (or one pixel) out of 64 channels (or pixels) of the MAPMT is under observation. Thus total hits per pixel per pulse is 0.11. Also, there are 64 pixels in the MAPMT; hence the total number of photons hitting the entire MAPMT surface per pixel per pulse is 64 times 0.11, which is 7.04.

Table 5.1: Single photon counts for different laser intensities.

Intensity Value	**% of Occupancy**	**No. of hits on MAPMT**
100	11%	≈ 7.04
200	12%	≈ 7.68
300	14%	≈ 8.96
400	15%	≈ 9.60
500	17%	≈ 10.88
600	18%	≈ 11.52
700	19%	≈ 12.16
800	20%	≈ 12.80
900	22%	≈ 14.08
1000	24%	≈ 15.36

Thus, for all the values of intensity settings on the laser, table 5.1 summarize all the corresponding number of photons per pixel per pulse for the MAPMT.

5.1.1 Signal Quality

Figure 5.5 shows two diagrams: one is a diagram of a typical MAPMT signal generated by a single MAPMT hit. As described in Chapter 3, the lengthy undershoot is a characteristic of the DiRICH amplification stage. The signal was refined and sent to the discriminator for further analysis based on the applied threshold. Additionally, the applied threshold evaluates the quantity of electronic noise or signal-to-noise ratio. Higher the threshold, lower the noise.

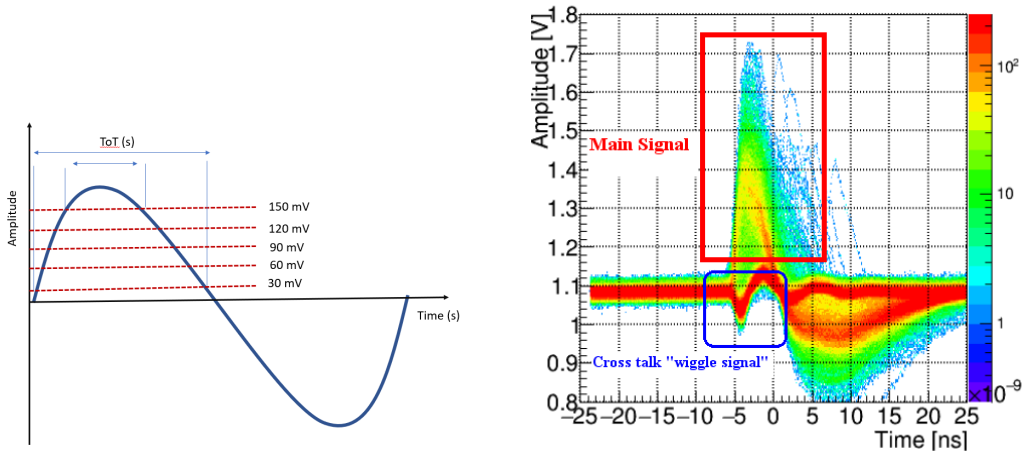

Figure 5.5: Schematic diagram of the output signal after pre-amplification from the DiRICH (left) and the actual image obtained on the scope (right).

The second graph on the right displays the scope signal obtained after pre-amplification and signal shaping. Two different signal shapes can be observed, as shown in the scope traces on the

right. The red box highlights the normal single photon signal shape, whenever a photon hit happened in the very same readout pixel. The second signal type, highlighted by the blue box, is of different nature: this signal shape is observed, whenever a photon hit the MAPMT, but in a different pixel than read out by the scope. This signal is called "crosstalk". Crosstalk, a characteristic of nearly all detectors, contributes to noise and consequently, the signal-to-noise ratio. Therefore, the true signal does not resemble that depicted in the schematic. In H12700 MAPMTs, the crosstalk signal (also referred to as the wiggle in this thesis) depicted in the blue square of figure 5.5 is of utmost importance and must be addressed immediately. Since these "wiggles" are the result of induction caused by the close proximity of channels, they often have smaller amplitudes with opposite polarity and can be mitigated by maintaining higher thresholds. However, maintaining a higher threshold also affects the photon yield, and the number of detected photons is essential for ring reconstruction in RICH detectors. Therefore, the primary objectives of these measurements were to suppress the crosstalks and determine an appropriate operating threshold.

5.2 Performance Tests

The performance study during this tests focuses on two parameters. 1) Time resolution 2) Time over Threshold (ToT) cuts.

- **Time resolution:** The core idea of the DiRICH readout concept revolves around time resolution. This parameter is the focal point of every component and the overall design of the DiRICH. Therefore, the DiRICH must be capable of measuring time resolution with the highest degree of accuracy. By definition, time resolution is the accuracy with which a detector measures the arrival of a signal when a particle traverses the detector. Leading edge time is the quantitative criterion for measuring time resolution (the time at which the signal amplitude crosses the applied threshold).
- **Time over the threshold:** The Time-over-Threshold is, as its name implies, the amount of time that the signal is above the threshold. Consequently, it represents the difference between the leading edge time and the trailing edge time. The width of this time difference corresponds to the signal's width. As explained in the preceding section, the H12700 MAPMT signal consists of two components: the main signal with a width of 4-5 ns and the wiggle signal with a width of 1-2 ns. Therefore, ToT plays a crucial role in crosstalk reduction, particularly when the detector is operated at lower thresholds.

All additional parameters addressed in the subsequent sections are examined for their effect on the signal's time resolution or ToT.

5.2.1 Effect of the laser intensity

After setting up the system, the initial test consisted of analyzing the effect of laser intensity on the performance of the DiRICH. The intensity corresponds to the number of photons per unit area of the detector. It is essential to understand how a detector responds as the number of photons that hit it increases. The variation in the laser intensity simulates this scenario. As described in Chapter 2, the improved RICH photon must have a large photon yield to reconstruct the Cherenkov rings more accurately, particularly for rare probes. In addition, it is crucial that the increased photon flux does not saturate the detector and affects its particle detection capability. The laser used in this test features an external adjustment to control the intensity in 10 stages, with a minimum setting of 1 and a maximum setting of 10. For the initial measurement, the laser intensity was kept at a minimum and the threshold values were measured. The same procedure was performed while the laser intensity was increased to its maximum level. As depicted in the figures 5.6 & 5.7, the effect of laser intensity on leading-edge time measurement is visible.

Figure 5.7 shows the leading-edge time distribution graphs. The X-axis represents time in seconds and the Y-axis represents the number of histogram entries. The three graphs depict three

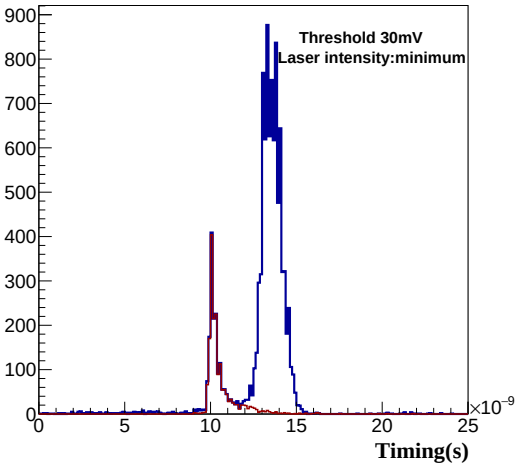

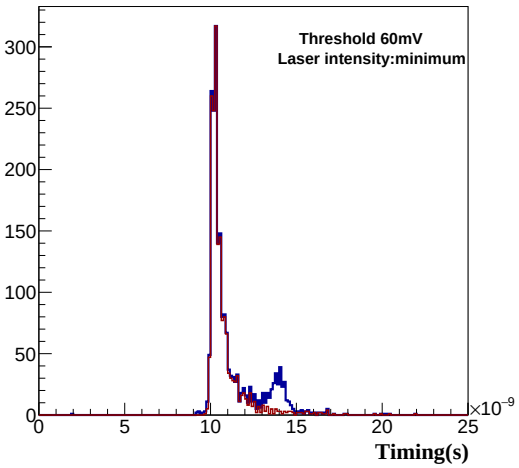

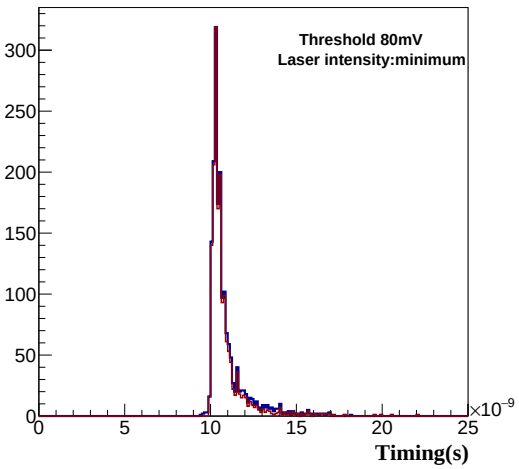

Figure 5.6: Leading-edge time for three different thresholds showing signal peak (red) and the wiggle peak (blue) at ***lowest*** value of laser intensity.

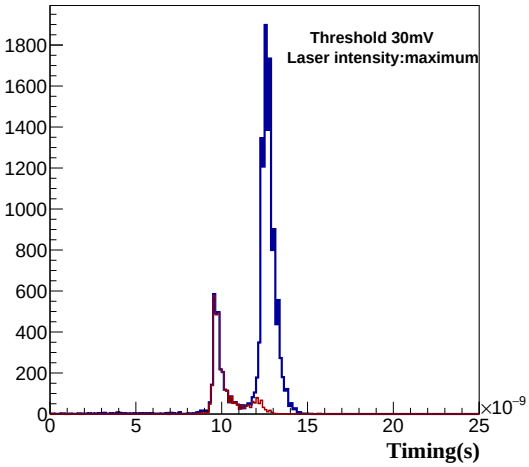

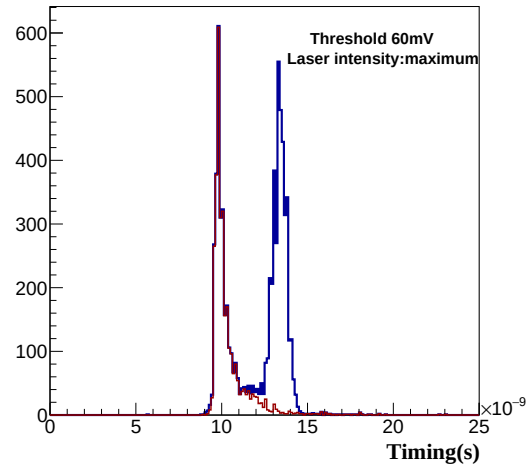

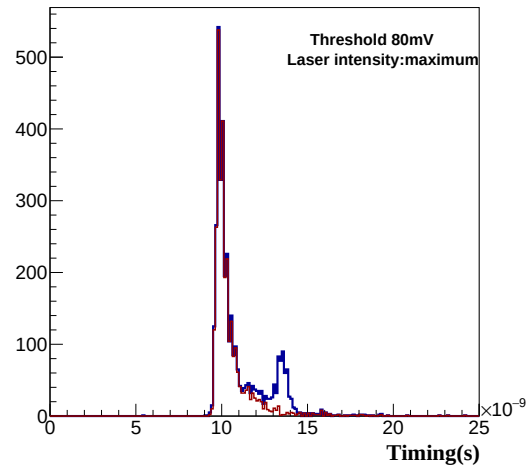

Figure 5.7: Leading-edge time for three different thresholds showing signal peak (red) and the wiggle peak (blue) at ***highest*** value of laser intensity.

distinct threshold settings, with each color representing a signal peak (in red) and a subsequent wiggle (in blue). As explained in the preceding section, the wiggle signal depends on the threshold; as the threshold increases, the signal amplitude decreases. This effect is also dependent on the laser intensity, which can be shown by comparing the plots of individual thresholds for various intensity settings, that is, by comparing figures 5.6 and 5.7 side-by-side.

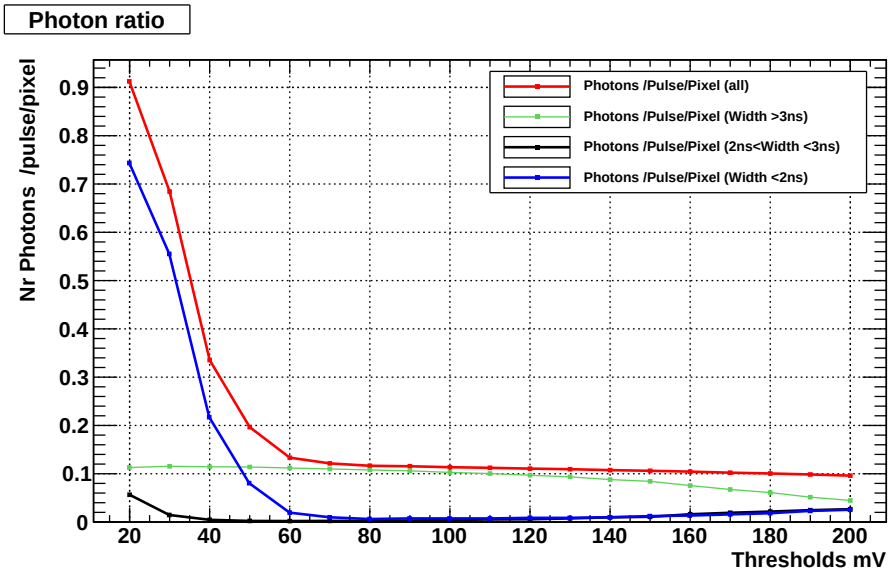

Figure 5.8: Photon fraction per trigger per pixel for minimum laser intensity.

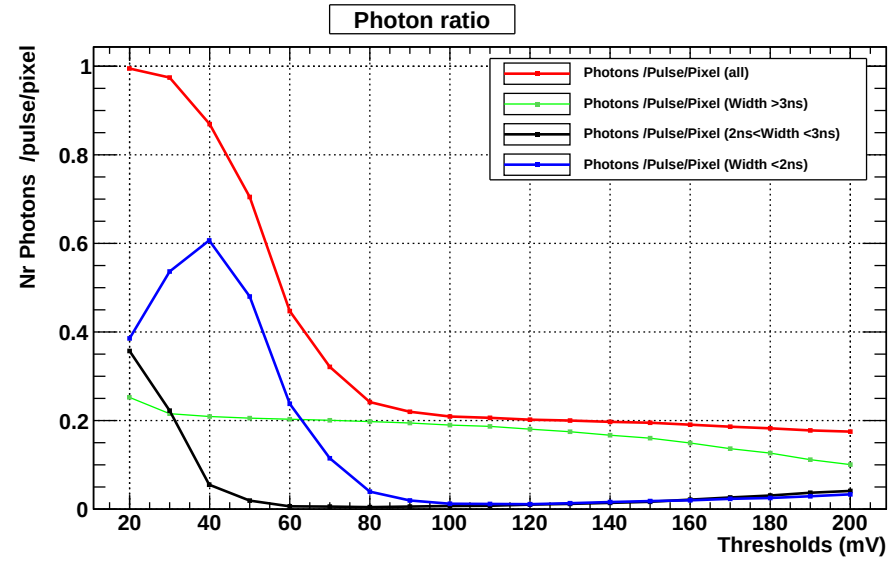

Figure 5.9: Photon fraction per trigger per pixel for the maximum laser intensity.

A comparison of the two numbers reveals that the wiggle depends on the intensity of the laser. As the intensity of the laser increased above a specified limit, the number of entries in both the signal peak and wiggle peak increased. However, the percentage increases in the signal peak and the wiggle peak were distinct. For instance, the number of entries in the signal peak (red curve) for a threshold of 30 mV increased by 50 percent from 400 for the lowest intensity setting (figure

5.6 top-left) to 600 for the highest intensity setting (figure 5.7 top-right) . In contrast, the number of entries in the same plot for the wiggle signal increased by 100 percent, from 900 to 1800 for the same threshold at varying intensities.

Comparing the bottom two plots of figure 5.6 and figure 5.7 reveals that as the laser intensity increases, the wiggle signal becomes dominant even at a higher threshold. Even at a high threshold of 80 mV, the figures indicate that crosstalk is observable (bottom two plots). This scenario is comparable to the high photon flux in HADES, especially in CBM experiments, where the rates are on the order of MHz. If crosstalk is not handled effectively, efficiency must be sacrificed for noise suppression.

Similar conclusions can be drawn from the plot in the figure 5.8, which illustrates the photon fraction per trigger per pixel for MAPMT at the lowest value of the intensity settings. This graph clearly demonstrates the effect of intensity on crosstalk. The red curve represents the total number of photons obtained per trigger per pixel for all MAPMT signal widths. The green, blue, and black curves show the photon fraction of signals with widths > 3 ns and 2 ns, and the overlap region of the signal and crosstalk peaks, respectively. From our comprehension of the signal, we already know that the width of the main signal is greater than that of the crosstalk hit. Based on this information, the following conclusions can be drawn:

- At low thresholds between 20-50 mV, the signal contributes largely by crosstalks as the blue and the black curve has larger values compared to the green curve. On a deeper investigation, comparing the plots of the figure 5.8 at the threshold of 20 and 30 mV, one can see that when laser intensity is low, the most significant contribution is from the blue curve (≈70%). At low intensity, few photons are hitting the MAMPMT so the wiggles are generated only in the neighbouring pixels.

  This condition changes when the intensity is very high, and there is a high chance of photons hitting two neighbouring pixels simultaneously. Thus, the crosstalk in the neighbouring pixel of both of these pixels might have a wiggle generated as a combination of both main signals and might have a higher amplitude, hence resulting in larger width. So, in figure 5.9, the contribution of the blue (signal width < 2 ns) curve seems to go down, but simultaneously the contribution of the black curve (signal width between 2 to 3 ns) increases significantly still contributing more than 70% (black + blue).

- As the threshold increases, the contribution from the wiggle drops and the contribution from the main signal dominates significantly. Further increasing threshold goes against the signal quality since at very high voltages (> 100 mV), even the main signal cannot cross the applied threshold to register as a hit and hence the yield of the detector decreases.

- An important aspect is a black curve (in figure 5.8 & 5.9) representing the overlapping region between the two curves in the figure (5.6 & 5.7). The signals having 2-3 ns width can be both from main hit or crosstalk, and hence there is no way to differentiate them. Fortunately, this problem vanishes once the threshold is increases beyond 60 mV where the threshold is sufficiently high to negate this effect.

After these observations, the role of laser intensity can be understood clearly. It is clear from the figure 5.9 that with an increase in laser intensity, the contribution of the signal having a width between 2-3 ns increases significantly. This represents the overlapping region between the two peaks in the figure 5.6 & 5.7, which is uncertain in determining the real signal or wiggle. Thus, the change in intensity harms the detector's performance and, as discussed earlier, will require a rigorous effort to reduce the noise.

5.2.2 Effect of the laser-trigger frequency

Test Parameters
Intensity: 100 (fixed)
Frequency: 1 kHz to 5 MHz
Trigger: Laser

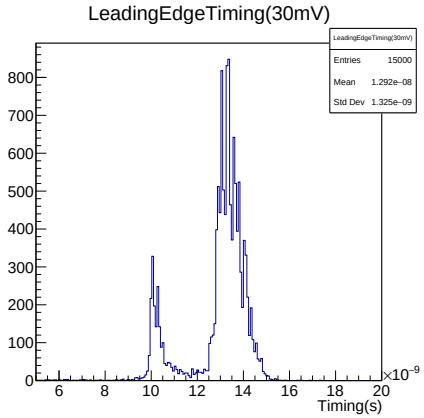

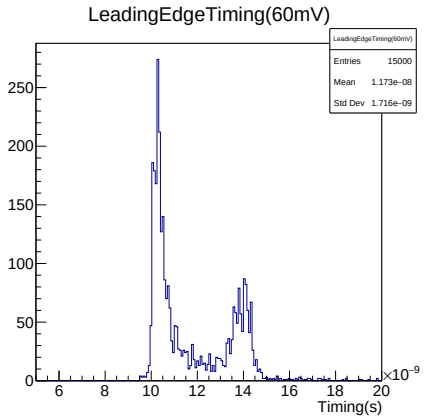

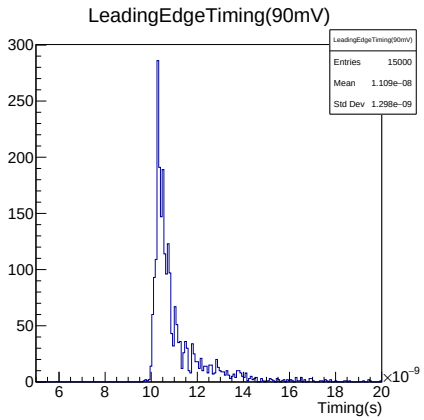

Figure 5.10: Leading-edge time for three different thresholds showing signal peak and the wiggle peak at ***lowest*** value of laser frequency.

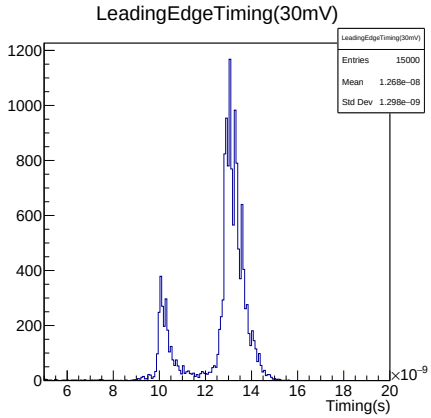

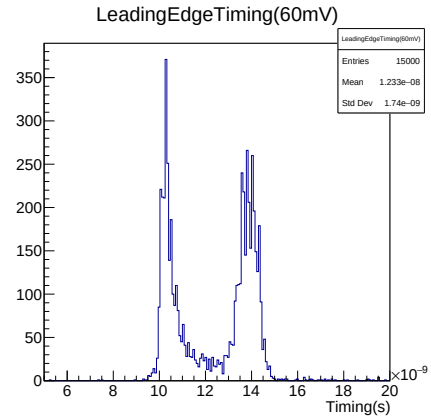

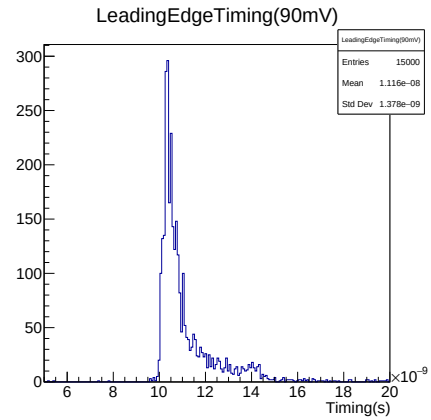

Figure 5.11: Leading-edge time for three different thresholds showing signal peak and the wiggle peak at ***highest*** value of laser intensity.

The preceding section examined the performance of the MAPMT and DiRICH in high and low intensity situations. This section explores the effect of trigger frequency on MAPMT performance. Any sensor or readout must be capable of handling large amounts of incoming data and quickly process that data. The amount of data it can process is limited by the time resolution of the detector. Another element that can effect performance is the rate at which the data is received. Before exiting the readout into DAQ for additional analysis, the detector must process the signal for some time. The time required for the detector to process the exisiting data is called the dead time where the detector is blind to incoming data. Thus, if the frequency of the incoming data is more than the dead time of the detector, then much of the recieved data is not processed by the detector.

The experiment's interaction rates dictate the performance limit of the detector. The higher the interaction rate higher the necessity for the trigger frequency. Before this update, the HADES experiment operated at the interaction rate of 20 kHz. In contrast, the future CBM experiment is expected to run at high interaction rates up to 10 MHz for the observables such as J/ψ at 1-5 MHz for multi-strange hyperons and dileptons, and at 100 kHz without any online event selection.

Figures 5.10 and 5.11 compare the leading-edge time plots for two sets of frequencies - 1 kHz & 5 MHz, at three distinct thresholds. These values cover the complete spectrum of probable interaction rates in the HADES and CBM experiments. In contrast to the plots in figure 5.6 and 5.7, there was no noticeable change in the number of entries, particularly in the signal peak. Even for a wide range of trigger frequencies, from 1 kHz to 5 MHz, this variation is negligible. For instance, with a threshold of 30 mV, the signal peak at 5 MHz had just 100 more entries than that at 1 kHz. Similar to the intensity plots, the wiggle peak(right) in the figures 5.10 and 5.11 exhibits a noticeable increase. Same observations were made for other values of thresholds.

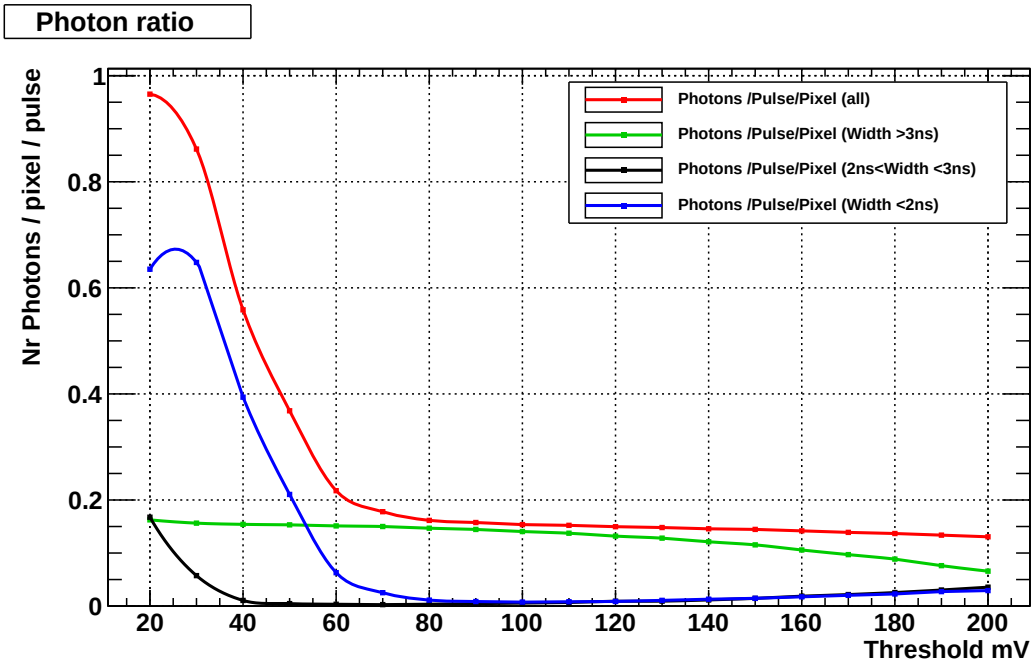

Figure 5.12: Photon fraction per trigger per pixel for minimum (1 kHz) laser frequency.

A better way to understand this effect is by looking at the photon fraction for both the values of frequencies, as shown in figure 5.12 & 5.13. The plots represent the photon fraction for different thresholds at two different frequencies, 1 kHz (Fig. 5.12) and 5 MHz (Fig. 5.13). The red curve represents the total number of photons striking the MAPMT per pixel per pulse, divided into three types of signals: the signal having a width larger than 3 ns (green curve), signals with width between 2-3 ns (black curve) and the signals having a width less than 2 ns.

Comparing the two plots reveals that they share many of the traits highlighted in the preceding

section. At low thresholds, the wiggle is the most important contributor to the photons. As the threshold increased, the contribution from the wiggle diminished, and the contribution from the primary signal increased. At higher frequencies and lower threshold values (50 mV), the signal with a width between 2-3 ns had a greater contribution, indicating an impact similar to that of an increase in laser intensity. As the frequency increases, the contribution to the overlapping region increases. For instance, the contribution of the main signal (green curve) at 40 mV is ≈ 0.16 at 1 kHz (Fig. 5.12), and at 5 MHz (Fig. 5.13), the contribution increases by ≈ 0.2, which represents a 25% increase.

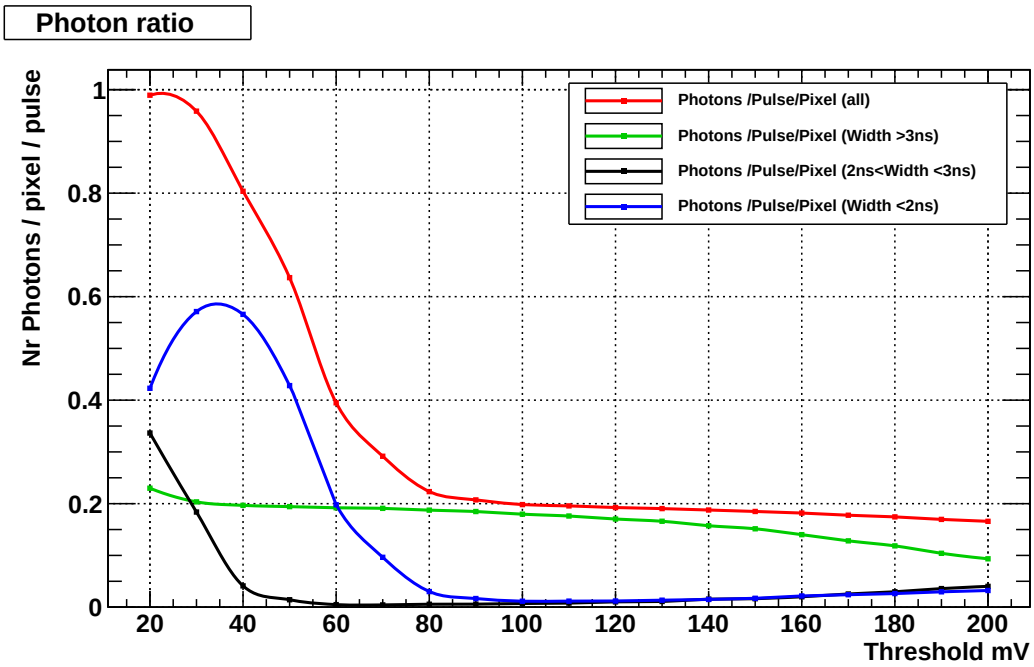

Figure 5.13: Total photon fraction detected per trigger per pixel for maximum laser frequency (5 MHz) (bottom).

In contrast to the intensity plots, a significant frequency variation (from 1 kHz to 5 MHz) is required to observe a change in the plots, demonstrating that the frequency change rarely affects the performance of the DiRICH. This notion is supported by the graph in figure 5.14, which depicts the percentage change in the photon fraction as a function of the applied thresholds. The plot comprises the following elements:

- The percentage change represents the change from the minimum value of the intensity and the frequency to the maximum value of the intensity and frequency respectively.
- The solid lines represent photon fractions for changes in intensity, whereas the dashed lines represent photon fractions for changes in frequency.
- The blue curve (both solid and dashed lines) represents the signal-widths >3ns, the red curve represents the signal-width of 2-3 ns, and the green curve represents the signal-width of <2ns.

From the plot, we can make the following observations:

- **Main signal (width >3ns):** The solid blue line contributes 100% more photons for the change in intensity, while the dashed line contributes <50% more photons for the change in frequency. This percentage increase is constant across all threshold values for both intensity

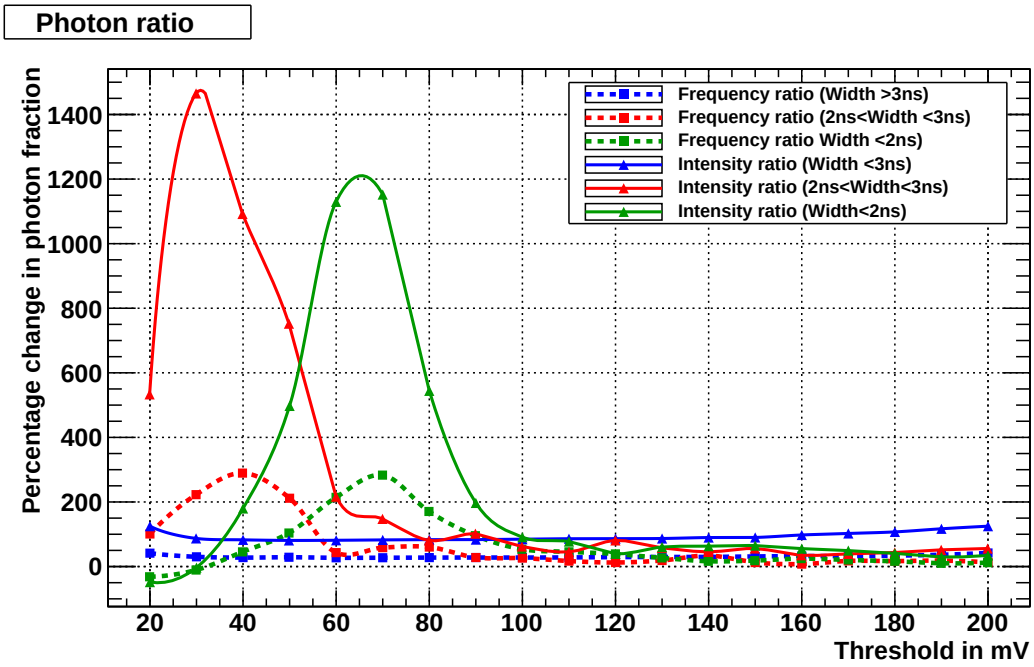

Figure 5.14: Comparision of the increase in the photon fraction for laser intensity change and laser-trigger frequency change.

and frequency changes. This verifies that the primary signal from an actual photon collision has a width greater than 3 ns (after the pre-amplification).

- **Wiggle (width <2ns):** At low thresholds (60 mV), the solid green line increases by 1,200% at its peak. This quantitatively confirms that large intensities have a significant impact on the wiggles. When the frequency was adjusted from 1 kHz to 5 MHz, the same effect was observed; however, the peak wiggle increased by 300%. Thus, at low thresholds, wiggles are a significant problem. Once the threshold is increased (>60 mV), the wiggles diminish exponentially but are still more noticeable at higher thresholds for large intensities than for large frequencies.
- **Overlapping region (2 ns**$< width <$ **3ns):** At low thresholds (<60 mV), the solid red line increases by 1400 % at its peak, indicating that the overlapping region between the signal and wiggle is increased significantly. This becomes a severe issue when cuts are applied to remove the noise since there is no way to distinguish signals from the wiggle by segregating them just based on their ToT (discussed in detail in the next section). The same effect is seen for the dashed lines, albeit, only increased by 300 %. At higher thresholds similar to wiggles, this effect also subsides.

The major purpose of these measurements was to verify the quality assurance of the DiRICH's components. To obtain an optimal signal-to-noise ratio, the detector must be operated at a voltage greater than 60 mV, assuming that there is no loss in photon yield. In addition, because the signal source (laser) does not replicate the conditions of the actual beam, it is futile to comment on the detector's efficiency at this time. To err on the side of caution, the scenario of the detector operating at lower thresholds and suppressing noise was considered. The sixth chapter discusses in depth a comprehensive test conducted under actual beam conditions using a complete module and functional FPGA-TDC.

5.2.3 Time over thresholds and ToT cuts

Time over the threshold is a crucial parameter for the DiRICH electronic readout. As explained in Chapter 3, the DiRICH readout is only intended to measure time information. Therefore, ToT information was incorporated while defining the noise-removal cutoffs. The basic plot of ToT at thresholds of 30, 60, and 90 mV is displayed in figure 5.15. These graphs demonstrate that the influence of wiggles is greatest at lower thresholds, and decreases with increasing thresholds. As previously mentioned, the wiggles have a lower amplitude; hence, they barely surpass the threshold, and have a lower ToT. Because the wiggles-ToT are sufficiently separated from the principal signal, this information can be used to suppress the crosstalk. As seen in 5.15, a cut defining a specified ToT value rejects all signals from the wiggles.

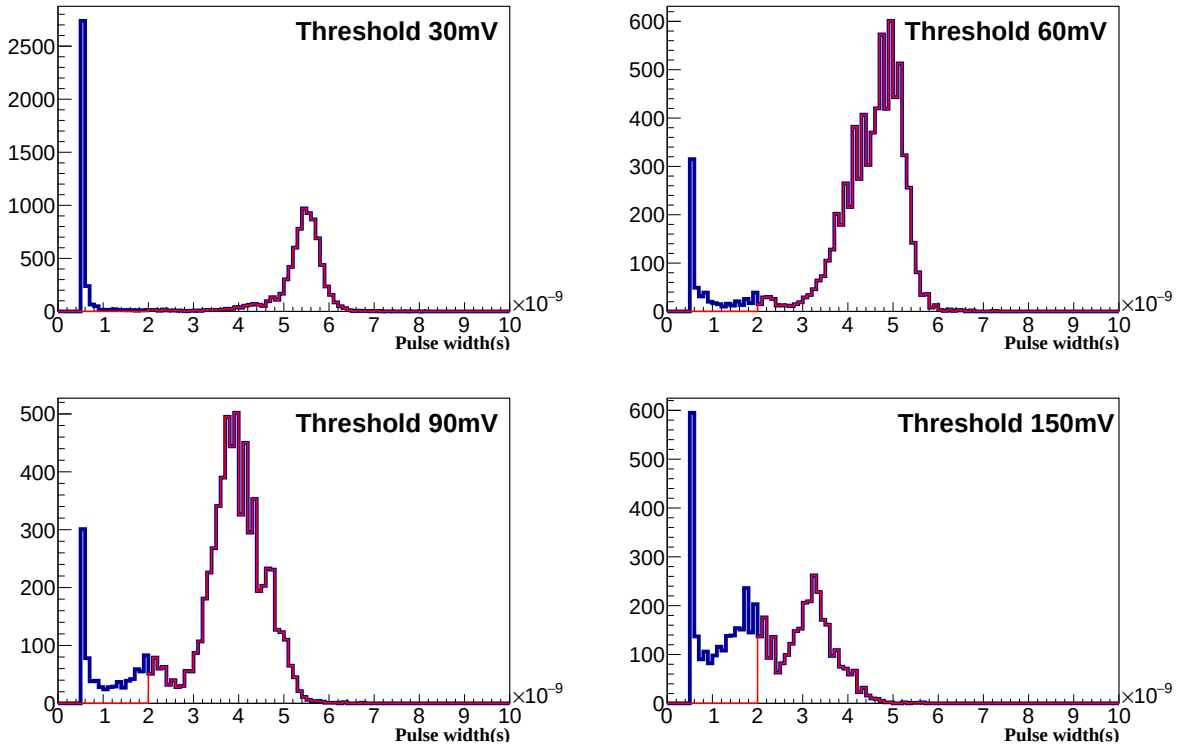

Figure 5.15: Plot showing the nature of the time over threshold measurements for the thresholds of 30 mV, 60 mV, 90 mV, 150 mV.

5.2.3.1 Aspects of ToT and ToT cuts

The ToT of the primary signal and the wiggle are well separated at low thresholds; hence, it can be employed to suppress crosstalks. During these observations, a 3ns cut was identified. All signals above 3ns were regarded authentic, whereas those below 3ns were regarded to be noise or crosstalk. In subsequent measurements, during the COSY beam test, ToT cuts were implemented using a distinct method, as described in detail in chapter 6. As the threshold is raised, the amount of crosstalks decreases, and there is clear seperation between the signa and the crosstalk, as evidenced by the leftward shift of the signal peak with each threshold increment. When the threshold is extremely high, even the primary signal barely exceeds it, and as a result, the ToT of the primary signal is likewise reduced, which explains why the peak shifts. There is no way to distinguish between the signal and any crosstalks (or noise). Consequently, it is likewise not recommended to run the detector at extremely high thresholds.

Another problem at a higher threshold is photon yield. It is evident from figure 5.15 that the

signal peak has a greater number of entries at the lower threshold (30 mV) and only 20% of the same entries at the threshold of 150 mV, which decreases even further when a cut >3 ns is applied (red curve). This becomes critical for the reconstruction of the Cherenkov ring. In the case of the HADES upgrade, the models indicate that 10–15 photons are required. The number of simulated photons considers only the quantum efficiency and 100 % collection efficiency given that the thresholds are ignored. In a plausible scenario, the overall number of hits might differ from the number of simulated photons. To reconstruct a ring, the ring-finding algorithm requires a minimum of four photon hits. Consequently, as the threshold increases, the detector efficiency decreases, and additional reductions in the ToT will have a substantial impact on this trend. Notably, the ToT histogram became unreliable at extremely high thresholds. Consequently, this technique for suppressing crosstalk is only effective at a low-to-medium threshold of operations.

5.2.3.2 ToT anomaly at high thresholds

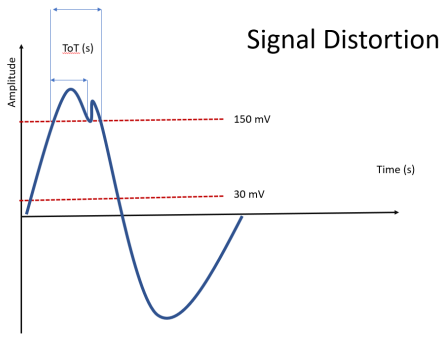

Figure 5.16: Schematic diagram of a MAPMT signal showing distortion in the signal shape.

The anticipated peak of ToT should consist of two peaks: one corresponding to signal and the other to wiggle. At higher thresholds, there should be no crosstalks hence, no wiggling peak in the histograms. Figure 5.15 demonstrates that the ToT histogram degrades as the threshold is raised to exceedingly high values. At 150 mV, there are two peaks, indicating signals of differing lengths from two distinct sources or an artifact that distorts the signal. The explanation of this phenomena is still unclear and under investigation. Few hypotheses can be a possible explanation or reason for this phenomena:

1) **Distorted trailing edge:** Figure 5.16 is a schematic representation of a common signal curve. This schematic shape may not be preserved at all levels of signal processing, and its quality may be affected by a number of variables. These variables may be introduced by the MAPMT or by the readout electronics. Nevertheless, there may be signal distortion at the signal's peak. When the trailing edge is tapped at a lower threshold, this issue is not affecting the ToT, but at the higher threshold when the trailing edge is tapped somewhere near the peak, distortion might affect the ToT. The oscilloscope measures two different instances of trailing edge in the same trigger window at higher thresholds and hence creates two different ToTs. This possibly is one of the reasons for having a double peak histogram of ToT.

2) **Photon signals from second dynode:** For multi-pixel sensors, such as MAPMT, it is possible for photons to completely bypass the first dynode and strike the second dynode that generates the signal. The probability of such occurrences is low, but nevertheless quantifiable. As depicted by the green curve in figure 5.17, the photoelectrons generated at the second dynode underwent less amplification and generated a smaller signal. The pulse width of this signal was shorter, resulting in reduced ToT. This may be an alternative explanation for the two-peak structure of the ToT plots at higher thresholds. Deeper investigation reveals that the leading edge timing of the two signal groups is somewhat different, indicating that the two peaks have two distinct signal sources. Figure 5.18 illustrates the relationship between ToT and the signal's leading edge time. Two different peaks appear in the 2D plots, indicating two signals with a minor shift in leading-edge time. The bottom two figures depict the

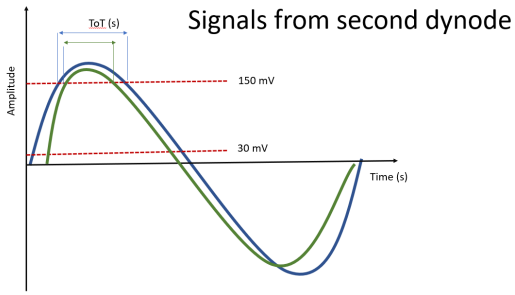

Figure 5.17: Schematic diagram of a MAPMT signal showing main signal (blue) and signal from the second dynode (green).

leading edge time for the signals with a ToT range of 1-2 ns and 3-4 ns. The average leading-edge times of each peak (in yellow) are 0.8 ns and 1 ns, respectively, suggesting that the signals may have different origins. However, as the change is negligible, it cannot be guaranteed.

Even with data from the beam test, the ToT spectrum includes a second peak at higher thresholds, indicating a similar issue. The cause of this anomaly is unclear and remains unknown.

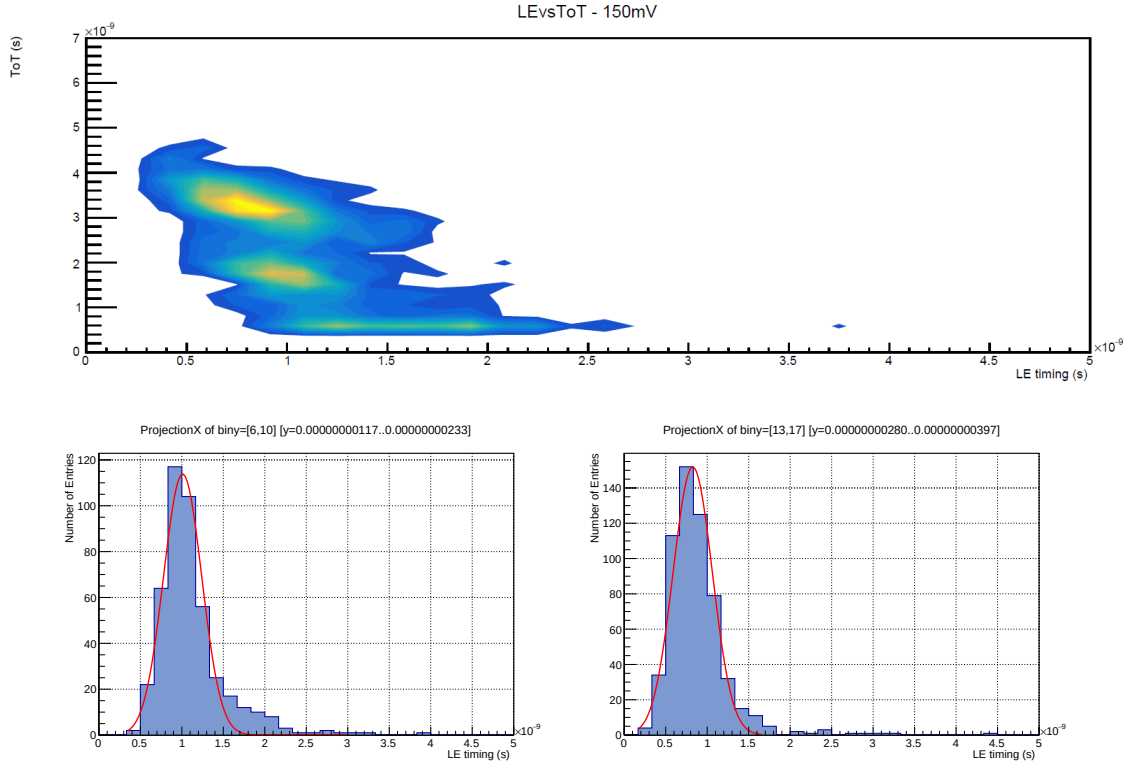

Figure 5.18: ToT vs leading edge plot for the threshold of 150 mV showing LE-time for ToT values ranging between 3-4 ns (bottom-left) and LE-time for ToT values ranging between 1-2.5 ns (bottom-right).

5.2.4 Time resolution

Time resolution is the most critical parameter for DiRICH. The central idea of the DiRICH readout chain is its ability to measure the precise time of arrival of the signal. For measurement of time resolution, two approaches were taken (i) Measuring time with respect to laser trigger and (ii) Measuring time with respect to another channel.

5.2.4.1 Timing with Laser trigger

Test Parameters
Intensity: 100
Frequency: 10 kHz
Trigger: Laser

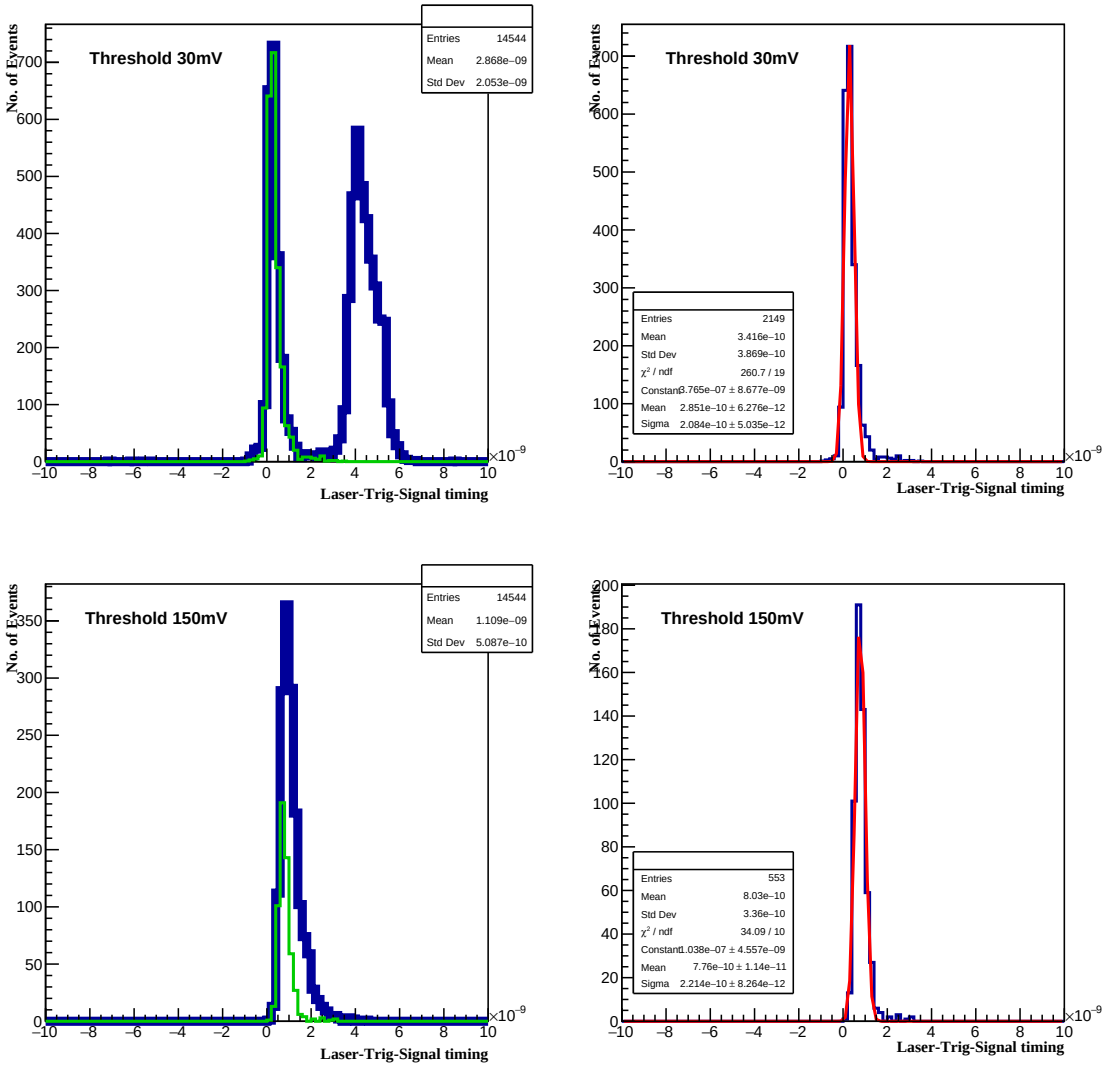

Figure 5.19: Leading edge time measurements for the threshold values of 30 mV and 150 mV (top-left and bottom -left) showing the two peaks. The left peak corresponds to main signal and the peak later is crosstalk signal from the neighboring pixels. The red plots on the right are obtained after applying ToT cuts on the main signal.

Figure 5.19 shows the leading edge time measurement for one channel under consideration. The plot shows two peaks, of which one belongs to the main signal, and the other belongs to the wiggle. The wiggle has an opposite polarity, so it comes later compared to the main signal with reference to trigger. To separate the main signal from the wiggle, we used 3ns -ToT cuts. Thus, in figure 5.19, the green curve represents the signal after applying the ToT cut. The signal peak fitted after removing noise and crosstalk is plotted as the red curve on the right. The sigma (σ) value of this fitted curve gives the time resolution of the signal peak. The exact process is repeated for all the thresholds. Figure 5.19 shows time plots for two extreme values of the thresholds.

The ToT cuts work perfectly at low thresholds, and the signal is nicely separated from the wiggle without losing the statistics. The sigma (σ) value for the fitted curve is 208.4 ps. As per the datasheet of H12700, the value of transit time spread (TTS) is 350 ps (FWHM). Thus, the FWHM of leading-edge time is given by $\sigma \times 2.355 = 490.782$ ps, which which is i reasonable agreement with the measured value, given the fact, that no walk-correction is applied in the measurement.

At higher values of threshold, since the ToT cut is not reliable, the green curve is within the blue curve and is cutting into the detector's efficiency. The fitted curve also had a worse sigma value of 221.4 ps which translates into the FWHM of 521.397 ps. Hence, it again proves that working with low threshold and ToT cuts is an efficient way to operate the detector. Table 5.2.4.1 shows

Threshold (mV)	Timing Sigma (ps)	Timing FWHM (ps)	Number of entries
30	208.401	490.782	2149
40	201.099	473.590	2101
50	210.699	496.198	2041
60	195.499	460.402	1966
70	264.099	621.955	1900
80	231.4	544.947	1774
90	228.6	538.353	1668
100	227	534.585	1460
120	229.4	540.237	1074
150	221.4	521.397	553

Table 5.2: Single photon counts for different laser intensities showing the timing information both in terms of sigma and FWHM. The last column shows how many entries were observed in the signal peak after applying ToT cut.

the time resolution (FWHM) for all the values of thresholds. It also shows the number of entries in the signal peak fitted after the ToT cut of 3 ns. It is evident from the table that as the threshold increase, the time resolution decreases, and so is the efficiency of the detector. The change in the time resolution is about 6.2% for the lowest and the highest value of thresholds, but the number of entries in the peak is reduced by 400%. The low statistics in the signal at higher thresholds also means that the calculated value of time resolution has significant discrepancies.

5.2.4.2 Effect of laser intensity and laser frequency on time resolution

As discussed in section 5.2.1, the intensity has a severe effect on the signal quality. It also affects the time resolution of the detector. Figures 5.20 shows the comparison of leading-edge time at the same threshold of 30 mV for different laser intensities (minimum-maximum). At a glance, increase in statistics due to increased intensity seems beneficial, but it becomes clear that it indeed, is affecting the timing measurements on a closer inspection. The plot shown in figure 5.20 is leading edge time measurement. The left plot on the top and bottom shows the plot both with signal and wiggle peaks, with green curve highlighting the signal peak after applying ToT cut. The plots on the right are zoomed version of signal peak after the ToT cut. The standar deviation of the righ-hand side plots gives us the time resolution of the detector. Comparing both the plots shows that the lower plot (maximum intensity) have a larger tail and a 3 ns cut still captures some part of the wiggle signal and hence increasing the standard deviation and hence the time resolution value for the lower plot and ToT cuts becomes inefficient.

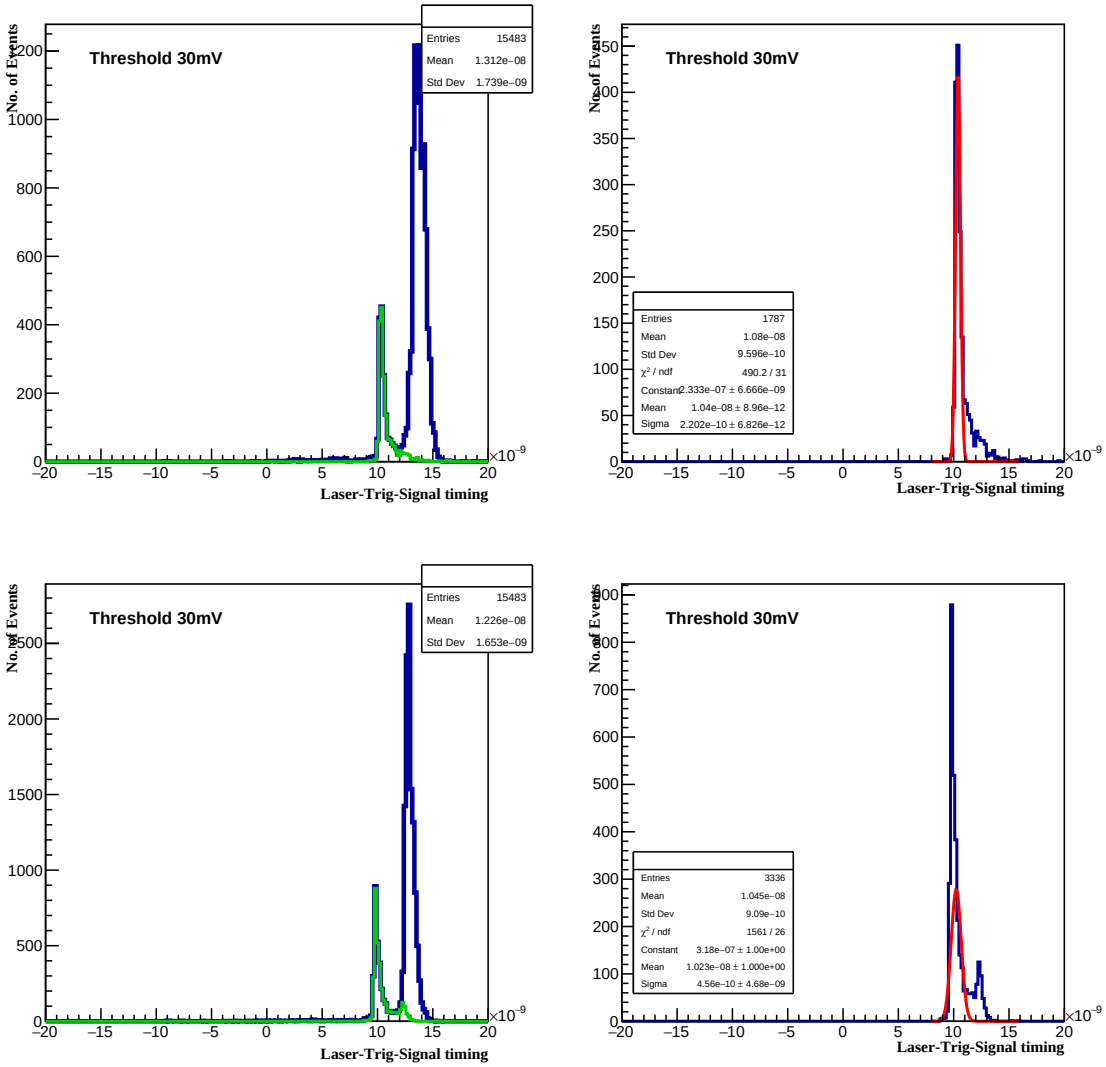

Figure 5.20: Leading edge time measurement for the threshold of 30 mV at minimum laser intensities (top) and maximum laser intensities (bottom). The left plots showing both signal and wiggle peaks with signal peak (green) after applying ToT cut of >3 ns plotted and fitted separately is shown on right hand side.

As the threshold increases, the combination of increased photons due to increased intensity and less noise favours the timing measurements, as seen from the figure 5.21.

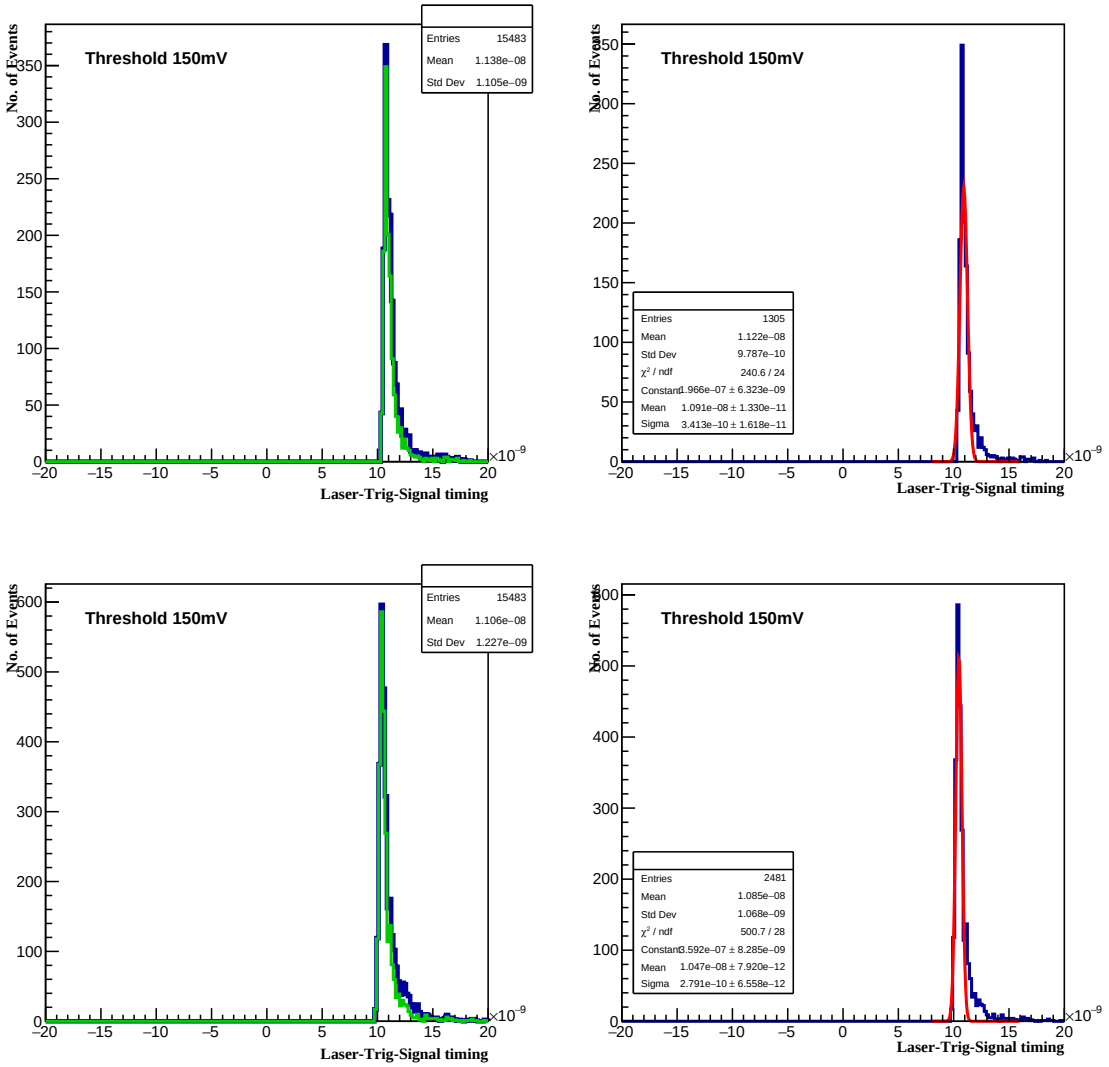

Figure 5.21: Leading edge time measurement for the threshold of 150 mV at minimum laser intensities (top) and maximum laser intensities (bottom). The left plots showing both signal and wiggle peaks with signal peak (green) after applying ToT cut of >3 ns plotted and fitted separately is shown on right hand side

From table 5.2.4.2 it is evident that for high intensities, there is a systematic degradation of the time resolution at any given value of the threshold, especially at low to medium thresholds. At a higher threshold, the degradation of time resolution for a low threshold is primarily due to the reduced statistics available.

Table 5.2.4.2 shows the comparison of time resolution for two different values of trigger frequency 1 kHz and 5 MHz. It can be concluded from Table 5.2.4.2 that the time resolution is not much affected by the change in frequency of the trigger.

Threshold in mV	Intensity (100)		Intensity (1000)	
	Timing(ps)	No. of Ent	Timing(ps)	No. of Ent
30	519	1787	1074	3336
40	477	1772	600	3237
50	455	1764	627	3180
60	no data	no data	613	3142
70	no data	no data	982	3105
80	no data	no data	707	3060
90	596	1641	677	3010
100	1205	1591	1070	2938
120	539	1500	938	2795
150	804	1305	657	2481

Table 5.3: Comparison of the time resolution for different laser intensity settings.

Threshold in mV	Frequency (1 kHz)		Frequency (5MHz)	
	Timing(ps)	No. of Ent	Timing(ps)	No. of Ent
30	822	2344	812	3051
40	1161	2311	1102	2950
50	539	2297	596	2913
60	531	2267	574	2880
70	537	2250	594	2863
80	971	2202	619	2811
90	584	2167	1089	2771
100	566	2108	926	2694
125	535	1978	633	2554
150	529	1731	669	2272

Table 5.4: Comparison of the time resolution for different frequency settings.

5.2.4.3 Channel -Channel Trigger

Test Parameters
Intensity: 100 (fixed)
Frequency: 10 kHz
Trigger: Channel vs Channel

Another way to measure the time resolution is by measuring the difference of time between individual channels. For this purpose, one channel acts like a trigger and the other as a channel under scrutiny.

This method is also used to measure time resolution during real beam conditions discussed in chapter 6. When a particle transverses through a medium producing Cherenkov ring in realistic conditions, the photons comprising the ring arrive simultaneously at the detector, albeit with some uncertainty. If the experiment uses an external trigger for measuring the time of arrival of the photon, then the uncertainty in the time resolution is folded with signal-timing and the uncertainty in the trigger. However, if the time resolution is measured by measuring the relative timing between two channels, then this systematic error of trigger uncertainty is removed.

Figure 5.22 shows the results of leading-edge time distribution relative to one other. It has a three-peak structure at low thresholds. The central peak at t= 0 belongs to the difference in the leading-edge time between simultaneous signal hits in both channels or simultaneous crosstalk hits in both channels. The first and the third peak at ±4 ns represents the leading-edge time between

the signal in one channel and crosstalk in the other. The oscilloscope measures the leading edge time from either of the channels when the signal crosses the threshold.

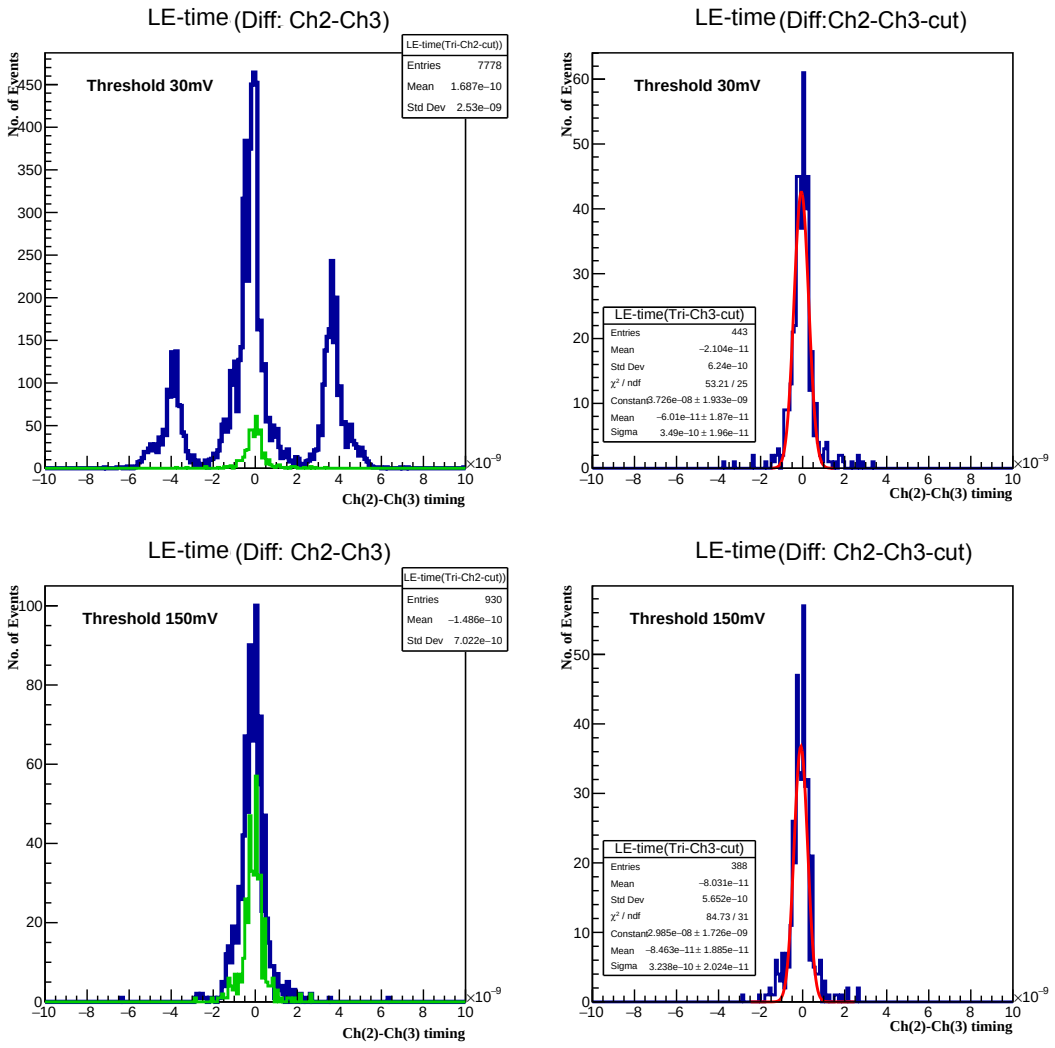

Figure 5.22: Leading edge time for the two thresholds 30 mV and 150 mV showing signal and crosstalk peaks for channel vs channel measurements. The left plot on the top and bottom represents the signal peak and the crosstalk peaks and the right plots represent the signal after applying ToT cuts.

If the signal from the 1st channel comes first and there is crosstalk in the second channel, then there is a positive difference in the leading edge time which creates a peak around 4ns. Since the threshold is low, there is a chance that even the wiggle signal crosses the threshold. Now, if there is a wiggle in the first channel and simultaneously there is a signal in the second channel, then the leading-edge time difference is negative, and hence the peak is created at -4 ns. The first TDC spectra measured with a fully operational DIRICH revealed a similar 3-peak structure, which came a bit as a surprising observation first. With the detailed measurements presented here, this mistery could be solved and the triple peak structure is fully understood.

It is noteworthy that the laser trigger produces a better time resolution than the relative time difference between the two hits. As discussed in the previous section, in the actual experiment, the Cherenkov photons arrive at the MAPMT simultaneously, and the timing measurement with the latter method is more efficient. While measuring timing in the HADES test box without a

Cherenkov source, the relative timing between the two channels is severely affected by various measurement parameters and other physical conditions. During the tests, only two channels were probed, and in addition to that, the source is a laser source that does not emit a Cherenkov ring but the stream of photons at a particular pulse frequency. Thus, it does not mimic an actual experimental condition. Nevertheless, it still gives reliable information about the behaviour of the DiRICH.

Time resolution is the essential aspect of the DiRICH, and these measurements proved that the DiRICH concept is a success. The readout performed as expected, and we learned a lot during these tests. The efficiency of the ToT cuts and the explanation of the three peak structure in TDC was a significant takeaway from these tests.

Table 5.5: Channel- Channel timing for all thresholds.

Threshold (mV)	Timing FWHM (ps)	Entries	Entries(fit)	%
30	821.895	7778	443	6
40	863.1075	2607	970	37
50	909.501	1413	1015	72
60	873.705	1185	1025	86
70	813.888	1133	943	83
80	889.9545	1076	910	85
90	843.561	1071	873	82
100	847.8	1023	785	77
125	836.967	1010	599	59
150	762.549	930	388	42

5.3 Power supply for the DiRICH

During these measurements, a critical aspect of the study was to check the feasibility of using onboard DCDC converters available on the DiRICH power module or using an external power supply. The idea behind two different power supply sets was to deal with the amount of noise introduced in the system due to the power supply since the signals from the sensor have small amplitudes. The power module supplies all the required voltages to MAPMTs and DiRICH and houses these components. For the optimal performance of a DiRICH we require four sets of power supply:

- 1.1 V for an analogue amplifier.
- 1.2 V for the Clock generators.
- 2.5 V for the Combiner board.
- 3.3 V for the FPGA.

With DCDC converters, all these requirements are met with just one cable with a 30 V supply, and the DCDC converters manage these voltages internally. If the power is supplied via an external LV source, then each of these voltages are supplied separately. Both of these systems come with their advantages and disadvantages.

5.3.0.1 DCDC

The main advantage of having a DCDC convertor is that only a single cable is required for supplying voltages to all the components. The upgraded HADES has 74 backplane modules and hence 74 ports for MAPMTs, and 74 ports for readout power supply are needed. It significantly reduces the costs of getting multiple voltage crates and managing the voltages externally manually. There is a significant gain in the space required for the cabling and placing the power supplies in the

detector cave. The problem with the DCDC converters is that they are significantly noisy due to the presence of active voltage elements on the DCDC converters. This noise interferes with the signal, and thus detector needs to be operated with higher thresholds as compensation.

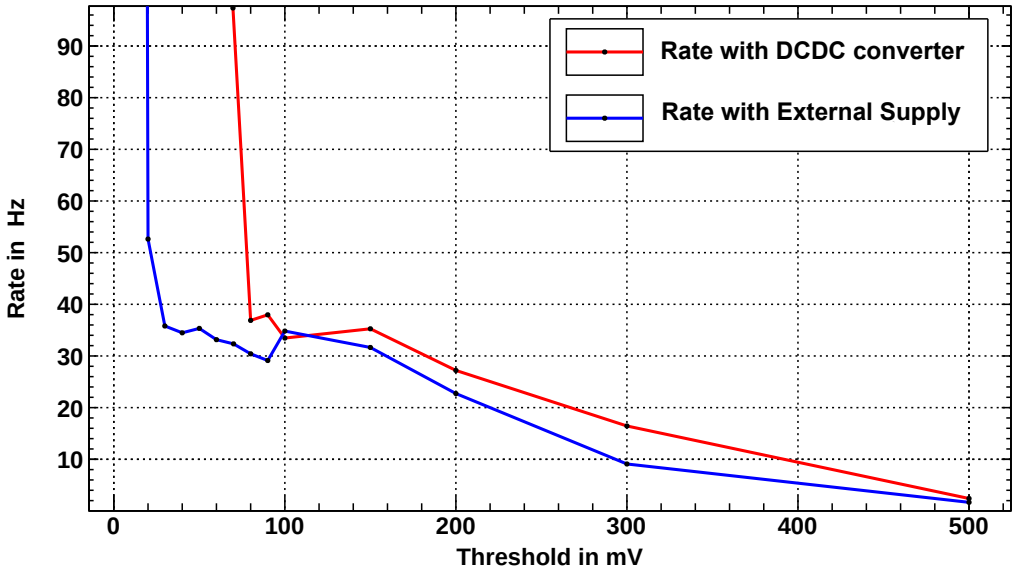

Figure 5.23: The dark rate measure with both DCDC converters and external supplies are shown in red and blue curves clearly indicating that DCDC converters are not performing as expected and adds a significant noise even at higher operating thresholds.

5.3.1 External supply

Multiple cables are required for each set of voltages discussed as shown in figure 5.23. Also, the cables need to be thick to manage the power requirement of 11 A @ 1.1 V. For HADES 74 modules with 888 DiRICH will be used which translates to almost 1000 A current. Each voltage has to be supplied individually with different voltage sources, which is expensive and requires space management in the experiment. Thus, there is a compromise with each of the supply method. A rate scan was performed with both the power supply methods to check which method is better for supplying the power to the DiRICH. For the first test, the power was supplied via DCDC convertors, and the dark rate was measured at different thresholds. For each threshold setting, the rate is measured for the same amount of time. The same process is repeated with the external supply with voltage values discussed previously.

Figure 5.23 shows the results of this rate scan. The red curve shows the rate with the DCDC converter, and the blue curve shows the rate with the external power supply. It is clear that the DCDC converter contributes to a large amount of noise in the DiRICH, even at a large threshold of 90 mV. Therefore, one cannot operate the detector below 60 mV, or the noise increases exponentially. It is crucial information since we already established in previous sections, that to have an efficient detector, it has to be either operated at a lower threshold in a combination of ToT cuts or should be operated below 100 mV in order to have a desirable efficiency.

This measurement proved that it was almost impossible to use the onboard DCDC converters in its current form. Many attempts were made to shield the components with copper shielding, but the noise problem persisted. In the end, it was decided to power the modules using an external supply. The HADES detector with upgraded RICH and the new readouts along with cabling is shown in figure 7.3

6 COSY Beam test

After obtaining promising outcomes from the HADES test box and the MAPMTS series testing, it was time to evaluate its performance under realistic beam conditions. For this purpose, the MAPMTS and DiRICH were exposed to a proton beam in the COSY accelerator at Jülich. The final chapter discusses the beam test results, which confirmed the DiRICH readout concept as the successor to the existing PADIWA-based detector system for lepton detection in all GSI experiments.

6.1 The COSY Accelerator

The Institute of Nuclear Physics in Julich, Germany, is home to the COoler SYnchrotron (COSY) (Fig. 6.1). Users can access polarized and unpolarized proton beams with energies ranging from as low as 45 MeV upto 2.7 GeV. A proton beam was utilized during the beam test of the MAPMT and DiRICHs. To produce a proton beam in the COSY accelerator, H^- ions are first generated from an ion source. Approximately 4000 V is used in order to separate these H^- ions from a hot plasma. The ions are then injected into a cyclotron, where their energy is increased from 4 keV to 45 MeV. At the point of injection, the ions are passed through a sheet of carbon foil, which strips away the electrons, and the beam then enters the COSY storage rings as protons [Mai97]. For one lap, the COSY takes about 2 μs, and within 1-2 seconds, the beam reaches the experimentally required energy. Depending on the beam properties for the given experiment, an additional facility for beam cooling is implemented [COS].

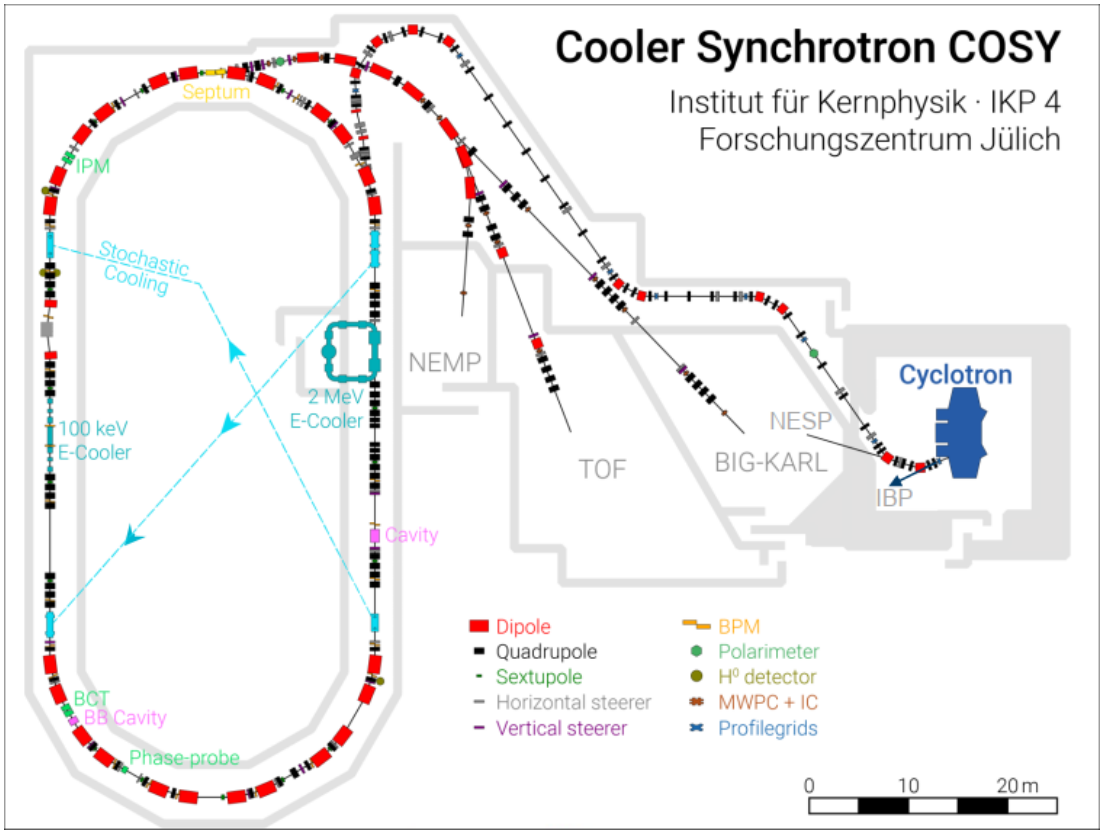

Figure 6.1: Schematic diagram showing the COSY accelerator facility - the injector cyclotron, the storage ring and the beamlines in the experimental area.

Once the required parameters are achieved, the beam is directed to the respective experiments for data collection. Typically, data collection takes between a few μs upto an hour. We utilized 2 GeV of polarized proton beam parameters for the beam test. The users can perform experiments internally within the storage ring where the target and the detector are placed in the storage ring, or one can use the external areas shown in the figure 6.1 where the beam is extracted, and the target is placed outside the storage ring. For our beam test, we used the Big Karl area, where beam time was allotted to other detector groups of the CBM-HADES collaboration and the RICH detector group [Appendix D.1].

6.2 COSY beam test setup

Positive results were obtained from the HADES test box; therefore, the subsequent step was to test the entire readout chain under actual beam conditions using an FPGA-TDC that was operational. The whole development of TDC took about a year; in the meantime, the DiRICH was constantly tested at GSI and Wuppertal to correct the issues that were present in the original prototypes and to optimize the design. Additionally, during this time period, groups at Wuppertal, GSI, and Gießen all began working together to initiate preparations for the beam test [AMAB+20]. The full development of the DiRICH was completed in November of 2017, at which point it was equipped with a functional FPGA-TDC and put to the test at the COSY accelerator in Julich, Germany. In order to accomplish this goal, a dedicated setup that was designed to the beamlines at COSY was developed. The apparatus is comprised of an aluminum box that has had the interior painted black in order to lessen the amount of stray light and various reflections that occur within the box. The central frame of the box houses two backplanes for the MAPMTs and the DiRICHs. The beam gap between the two backplanes was maintained at a distance of five centimeters. Each backplane has the capacity to store one power module, one combiner module, six MAPMTs, and twelve DiRICHs. The entire system included 12 MAPMTs, 24 DiRICHs, and the power and combiner modules that corresponded to each of these components. TRB-net was used to establish a connection between the entire system and a separate DAQ system. One may access the MAPMTs and the readouts separately as the box has independent aluminum covers that can be attached to either of its two sides. The main components of the beam tests were:

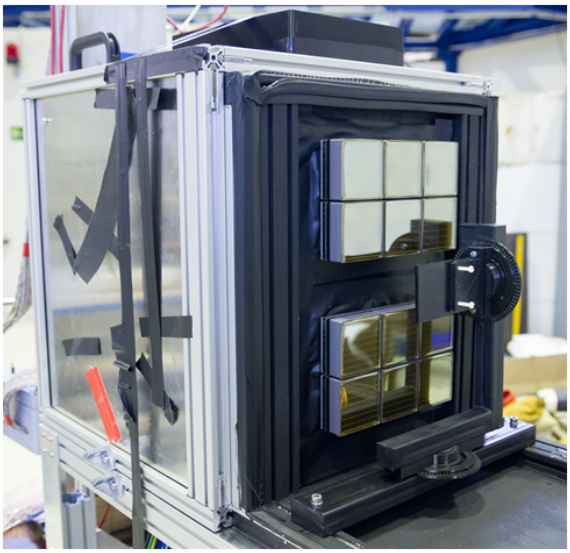

Figure 6.2: COSY beamtest setup showing 12 MAPMTs and a quartz glass plate for the proximity focusing setup in front of the MAPMTs.

Proton Beam: Proton beams of different energies up to $E = 2$ GeV (total energy, $E_{kin} \approx 1$ GeV) were used during the data taking over several days.

Radiator: Two types of the radiator were used in the beam test. One was a plano-concave lens. It was coated with a reflective coating of magnesium fluoride. This glass acted both as a solid-state radiator and as a focusing element for Cherenkov light emitted in the glass. The light will be reflected towards the MAPMT plane. The second was a quartz plate used as a proximity focusing detector. This was $1.5^{''} \times 1.5^{''}$ in plate placed very near to the photon detector plane. Since there was no focusing element present, the Cherenkov rings produced here were blurred. All the discussion in this thesis is based on the data obtained with the proximity focusing, i.e. with the data obtained from quartz plate radiator.

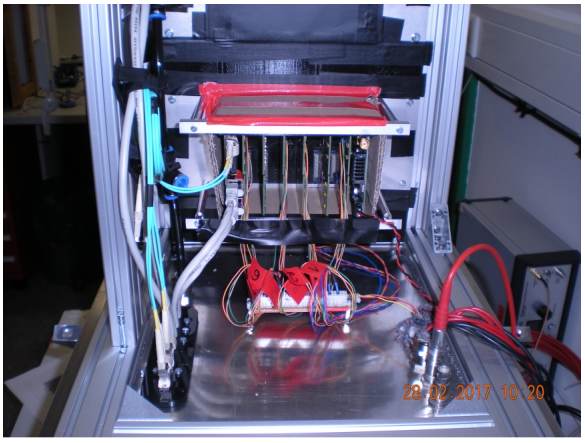

Front view of the test box

Figure 6.3: The DiRICH readout electronics mounted on the back of the beam test setup with all the cabling.

Photon detector plane: It consists of H12700 MAPMTs and the DiRICH based readout system for the MAPMTs in the arrangement described in the above paragraph.

Trigger and DAQ: Having a trigger detector before, and another trigger detector after our setup, with a coincidence trigger condition using both, allows to trigger only protons fully traversing the test setup on a straight, centered track. For suvh a track, the expected Cherenkov photon yield is well defined and well known from Monte Carlo simulations.The data acquisition system was based on DABC, which generated files from the data collected during the test.

Analysis Framework: The data collected during the beam test is studied using a framework called Go4 [AATB+05] which is based on ROOT.

A schematic diagram for the setup for COSY beam test is shown in figure 6.4 while the real pictures of the MAPMT and readout are shown in figure 6.2 & figure 6.3.

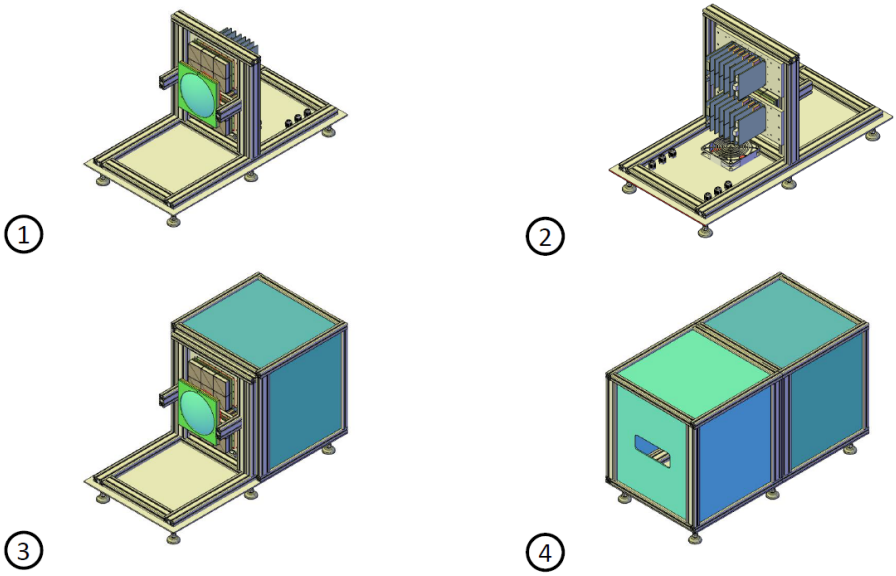

Figure 6.4: Schematic diagram showing different section of COSY beam test box and position and its construction details. (Courtesy: Dennis Pfeifer)

The proton beam for the beam test was provided by COSY accelerator situated in Julich, Germany. The main goal of this beam test was to check the completed system, i.e. MAPMT and the DiRICH based readout system in real beam conditions and to check the effect of wavelength shifting coating (WLS) on the efficiency of the detector. The parameters which were needed to verify the performance of the detector were:

- **Efficiency of the detector:** It is defined as the ratio of the number of Cherenkov photons

detected by the detector to the number of photons hitting the MAPMT plane. This can be measured by measuring the hit multiplicity of the detector.

- **Hit multiplicity:** It is the total number of Cherenkov photons (after removing noise and crosstalk) detected on the MAPMT plane.
- **Effect of WLS on efficiency:** It was seen in the laboratory tests that quantum efficiency of MAPMTs was increased in the UV region if the outer surface of the MAPMT was treated with WLS coating. During the beam test, the same effect had to be verified for real beam conditions.
- **Timing precision:** The main goal of the HADES-RICH upgrade was the timing precision of the newly developed readout electronics. The central idea of the whole project was to create a readout which can accurately measure the time resolution of the detector. During the analysis of the data, it was found that the time precision worsens for the MAPMTs coated with WLS coating.
- **Ring parameters:** The beam time was the first and the only time when the RICH detector with H12700 MAPMTs and DiRICH readouts saw the Cherenkov photons before the final installation in HADES-RICH. Hence it was very crucial to see how it performs in the real beam conditions. The ring quality, ring radius, and other parameter were tested during the beam test.

6.3 Cosy beam test results

The COSY test beam was a success. The data collected during the test was analysed using the Go4 framework. The Go4 is a root based framework specifically designed for low and medium energy nuclear physics experiments. Complete documentation for the Go4 and its installation details are in [AATB+05]. After installing Go4 correctly, the analysis of COSY data begun. The first step in this analysis was to implement fine time calibration. This fine time calibration was done to ensure that we have proper timestamps for trigger and corresponding hits, and that there is no effect of temperature or other factors on FPGA based TDC, more details are found at [Web18]. After ensuring that the proper fine time calibration is achieved, data were examined for proximity the focusing setup.

6.4 Implementation of Time over Threshold cuts

During HADES test box studies, it was found that one can separate the primary signal from the crosstalk by implementing cuts on time over the threshold. The same approach was implemented in the COSY beam test analysis. However, it was not as straightforward as during HADES test box measurements. In HADES test box measurements, since the fpga-tdc was not ready, the signals from two channels were digitized using a oscilloscope and picked up directly after the preamplification before they enter the FPGA-TDC. For COSY though, TDC chain was fully developed, and timing was measured using the FPGA-TDC thus, it was mandatory to align all 800 channels first and then define a ToT cut.

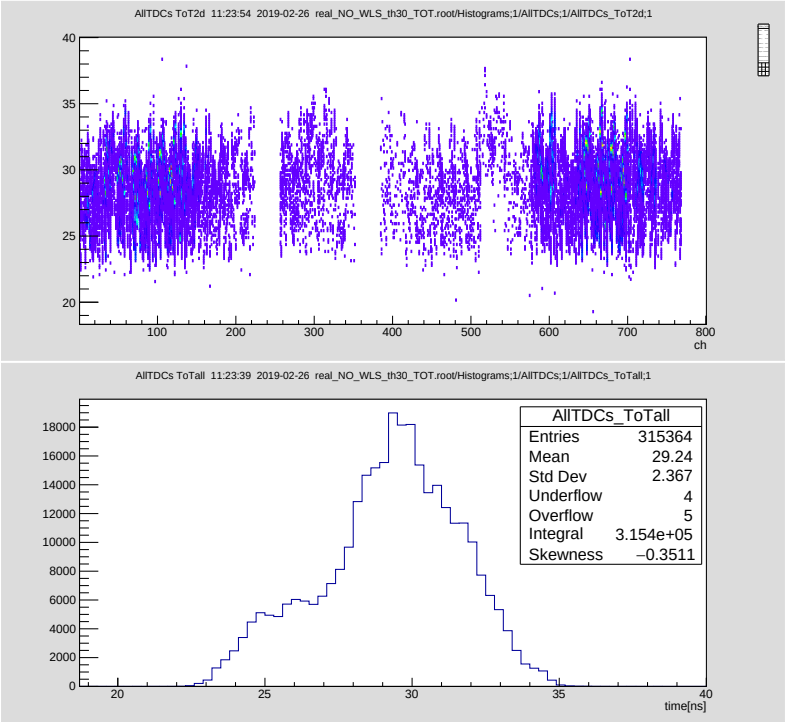

Figure 6.5: 2D distribution of ToT for all the channels at threshold of 30 mV before the alignment and its y-projection.

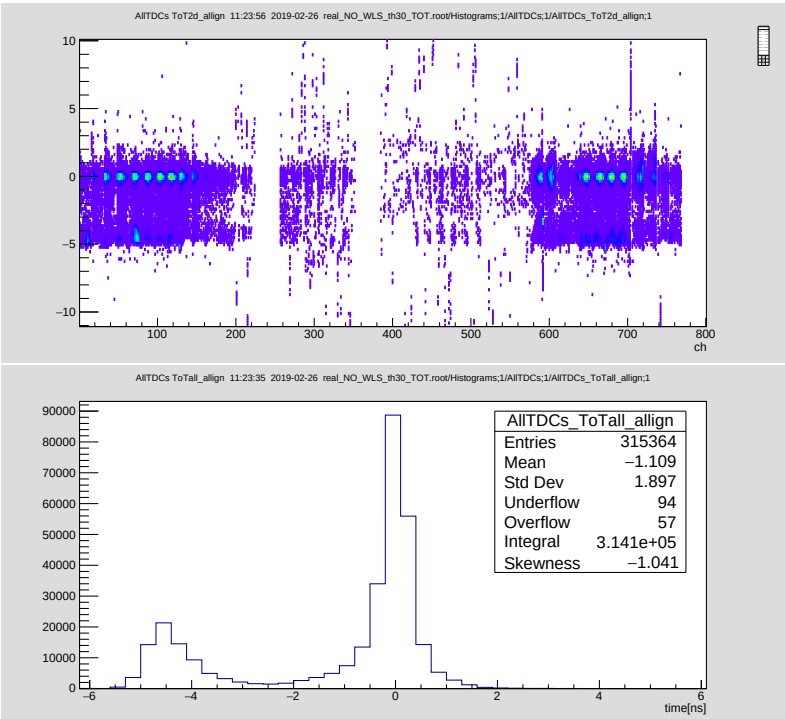

Figure 6.6: 2D distribution of ToT for all the channels at threshold of 30 mV after the alignment and its y-projection.

The plot in the figure 6.5 shows the Time over Threshold for all the channels with an operating threshold of 30 mV and the bottom plot shows the Y-projection of figure 6.5. It can be seen that Y-projection does not look like a two peak structure as expected. Individual ToT of a single channel is a two-peak structure where the first small peak represents the capacitive crosstalk in the adjacent channels and the more significant peak on the right side represents the primary signal (e.g. figure 6.7). Thus, one can easily see the requirement for alignment of channels.

The plot in the figure 6.6 shows the collective ToT spectrum of all 800 channels after alignment for the operating threshold of 30 mV. This plot resembles the single-channel ToT distribution. For each channel, the signal peak was gauss fitted and the parameters were stored in a text file for each channel individually. These parameters represent the offset in ToT for each channel. These offsets were corrected by taking the difference of the mean of individual signal-ToT for each channel calculated in Go4 and offset from the file for the same channel. After this stage for each channel, two approaches were tested:

Fix-width ToT cut: In this approach a fixed value of time cut was defined around the primary signal. For e.g., ±1 ns, ±2 ns, ±3 ns, around the signal peak. The events outside these limits were discarded. This way it gets rid of the capacitive crosstalk, and only actual single-photon events are accepted. The following plot shows the results of various fix time widths of ToT plot. The plot in figure 6.7 shows a sample of the ToT distribution of a single channel of a MAPMT. As expected from the previous test in the HADES test box, one can see that there is a two-peak structure in ToT distribution. The small peak on the left represents capacitive crosstalk which is also termed as "wiggle", and the large peak on the right represents the main signal from a Cherenkov photon. The X-axis represents the width of the signal over the applied threshold and Y-axis represents the number of entries in the histogram. One can easily see that the main signal has a more significant ToT than the wiggle peak and also that they can be separated easily by applying cut around the signal peak. In this case, the cut value was defined as the fixed value around the signal peak.

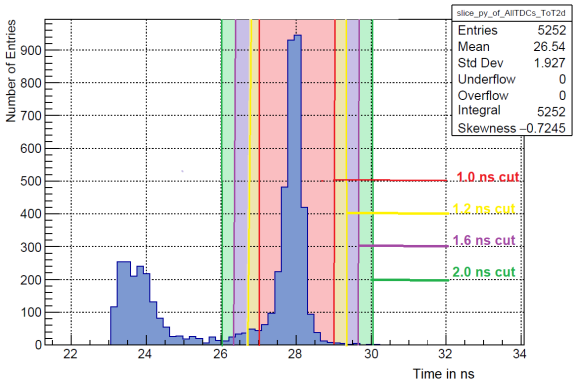

Figure 6.7: ToT distribution of a single channel showing two peak structure as expected from previous tests. Different color shade area representing different value of ToT cuts applied on either side of signal peak.

Sigma cut: In this approach instead of taking fix width around the signal peak, sigma of gauss fit of the signal peak was used as the cut parameter. For e.g., 1 sigma of all the events in signal peak, 2 sigma and so on.

6.5 Hit Multiplicity and the efficiency of the detector

A preliminary measure to check the effect of various cut, which is discussed in the following sections is the hit multiplicity. It is defined as the total number of hits detected by the complete MAPMT plane in one event. Thus it gives an idea of how many hits of Cherenkov photons were detected in one run. In case of COSY beam test, it was expected from simulations [LHO+10] that there would be roughly 16 photons per event. The validity of success during COSY beam test rests on one of the facts that how close we measure the hit multiplicity to simulated results (after applying proper cuts).

For the H12700 Multi-Anode Photomultiplier Tubes (MAPMTs), the recommended operating voltage is set at 1000 V. However, during the beam test, a critical assessment was conducted to as-

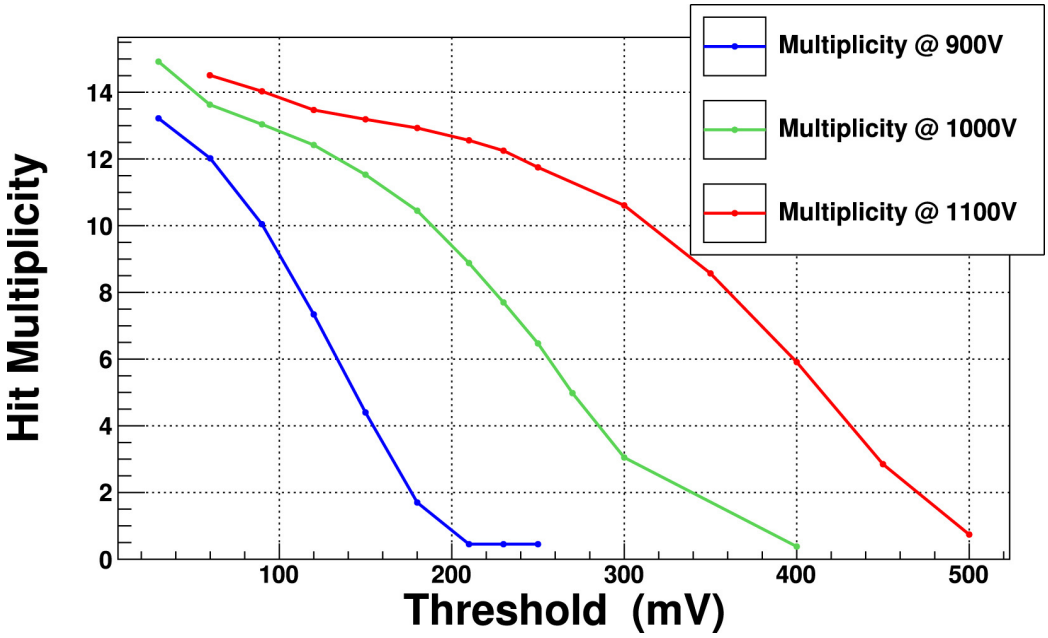

Figure 6.8: Hit multiplicity of the detector for different operating thresholds at three different values of MAPMT voltage.

certain the MAPMTs' functionality under non-standard voltage conditions during operation. Prior to data cleaning, raw values of hit multiplicities were plotted and are presented in Figure 6.8.

Throughout this examination, the PMT was subjected to both under-voltage (900 V) and over-voltage conditions, and the resulting hit multiplicities were recorded for each specific operating threshold.

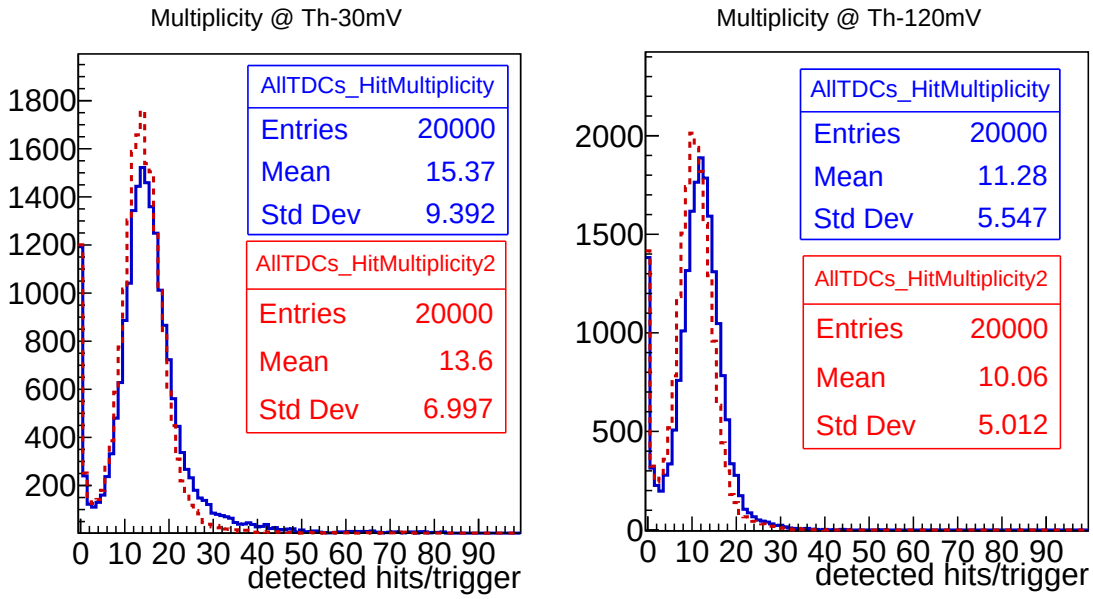

Figure 6.9: Hit multiplicity of the detector at two different operating thresholds of 30 mV (left) and 120 mV (right) before applying ToT cut.

It is noteworthy that the gain of the MAPMT (and, by extension, the detector's efficiency) ex-

hibits a direct correlation with the applied voltage to the MAPMT. Importantly, this variance in voltage does not appear to exert a significant impact on hit multiplicity. Nonetheless, it is imperative to stress that operating the MAPMTs at voltage levels other than the recommended settings is discouraged. Such deviations have the potential to compromise long-term performance and the overall lifespan of the MAPMTs, as highlighted by Muheim (2003) [Muh03]

Figure 6.9 illustrates the hit multiplicity at operating voltages of 30 mV and 120 mV after the application of a Time-over-Threshold (ToT) cut. It is evident that, even with the implementation of the ToT cut, there is no substantial reduction in multiplicity. The algorithm responsible for identifying Cherenkov rings, based on the number of hits on the PMT plane for each event, requires a minimum of four hits for ring reconstruction. In this scenario, even after the ToT cut is employed, there remains an ample surplus of hits available for the construction of Cherenkov rings. Consequently, the application of the ToT cut enhances signal quality without compromising detection efficiency.

This phenomenon becomes even more apparent in figure 6.10, where the hit multiplicity is plotted as a function of operating thresholds. The black curve represents multiplicities at various thresholds without any applied cuts. The solid blue lines depict the ToT cut based on fixed width, while the dashed red line represents the cut based on sigma values, as explained in the preceding section. Although both approaches yield comparable results, the sigma-based cuts were utilized throughout the analysis, as they offer the advantage of fine-tuning data selections, as opposed to relying on rigid cut values.

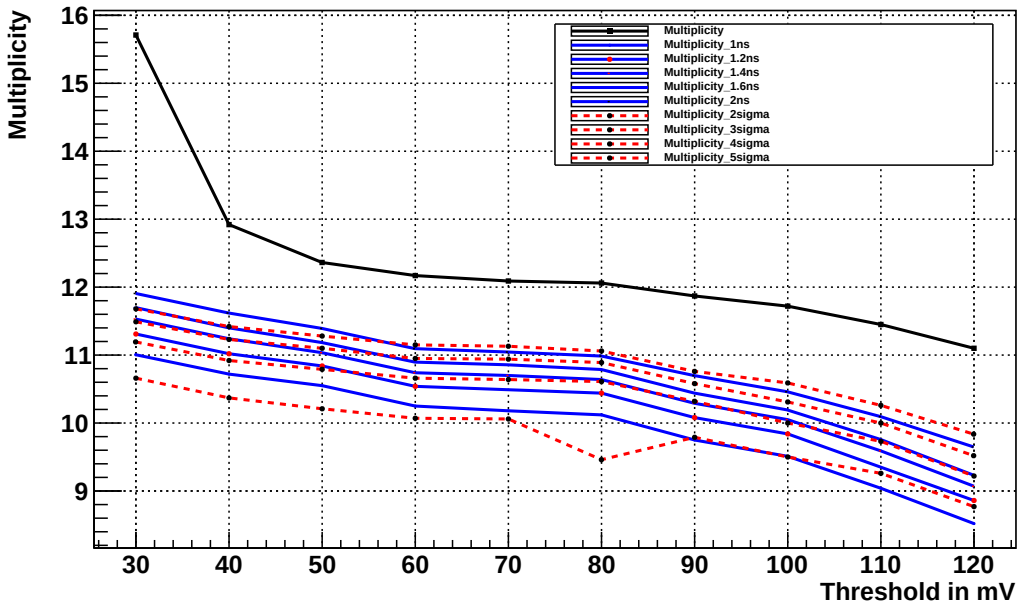

Figure 6.10: Hit multiplicity of the detector showing multiplicity as a function of thresholds for different values of ToT cuts shown in blue and red curves.

6.5.1 Hit Multiplicity and Wavlength shifting coating

The application of a Wavelength Shifting Coating (WLS) to the external surface of the Multi-Anode Photomultiplier Tube (MAPMT) was undertaken to enhance its performance in the ultraviolet (UV) region. The quantum efficiency investigations, discussed in the Section 4.3.1, reveal an increase of approximately 20% efficiency in the UV region, with a peak efficiency around 250 nm. During the beam test, data were collected using MAPMTs equipped with the WLS coating. The impact of the wavelength-shifting coating on hit multiplicity is graphically represented in figure 6.11.

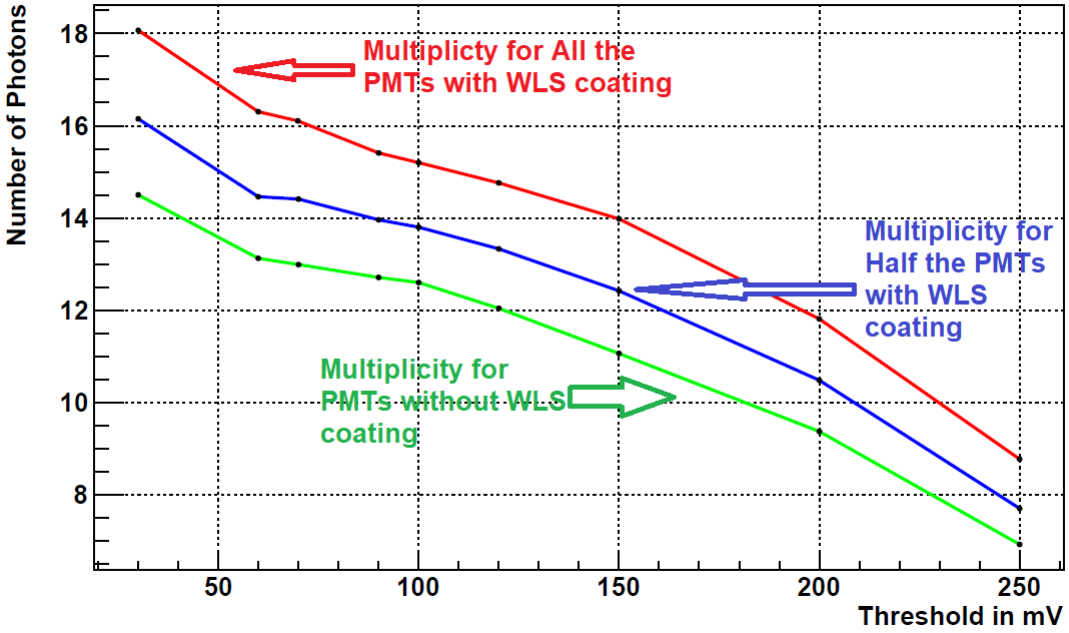

Figure 6.11: Hit Multiplicity as a function of thresholds for all MAPMTs (red) half of the MAPMTs (blue) and No coating on MAPMTs (green). **Note:** No ToT cuts were applied for this particular plot.

Figure 6.11 presents the hit multiplicity as a function of varying operating thresholds. The experimental procedure consisted of three distinct phases. Initially, Multi-Anode Photomultiplier Tubes (MAPMTs) coated with Wavelength Shifting Coating (WLS) were exposed to the particle beam, and data were recorded across a range of thresholds in 10 mV increments. Subsequently, the WLS coating was selectively removed from half of the MAPMTs, specifically those located in the lower module, and data collection was repeated under the same range of thresholds. Finally, all MAPMTs had their WLS coating removed, and data were once again recorded at various thresholds. This systematic and quantitative approach to data collection facilitated a comprehensive understanding of the effects of WLS.

At any given operating threshold, the multiplicity of hits recorded when all MAPMTs were coated with WLS exhibited an approximate 20% increase in comparison to the absence of coating (illustrated by the red curve). The multiplicity with half of the MAPMTs coated with WLS showed an approximately 10% increase, signifying the impact of the WLS coating (as represented by the blue curve). The green curve denotes hit multiplicity when none of the MAPMTs were coated with WLS.

In figure 6.12, a quantitative assessment of the effect of WLS is demonstrated. If the plots in figure 6.11 are normalized, we obtain Figure 6.12. The black curve in figure 6.12 represents the multiplicity of MAPMTs without any coating, normalized as a reference. The red curve in figure 6.12 portrays the ratio of multiplicity in MAPMTs with the WLS coating concerning the multiplicity of uncoated MAPMTs. The green curve shows the ratio of multiplicities of half of the MAPMTS and all the MAPMTs with WLS coating (red curve). The blue curve signify the ratios of multiplicities for half the MAPMTs coated with WLS coating compared to multiplicities of MAPMTs after removing WLS coating from all the MAPMT (black curve). This plot clearly underscores the substantial influence of WLS on hit contributions and the efficiency of the detector, which unquestionably improves with the implementation of the WLS coating, albeit with certain trade-offs to be discussed in subsequent sections.

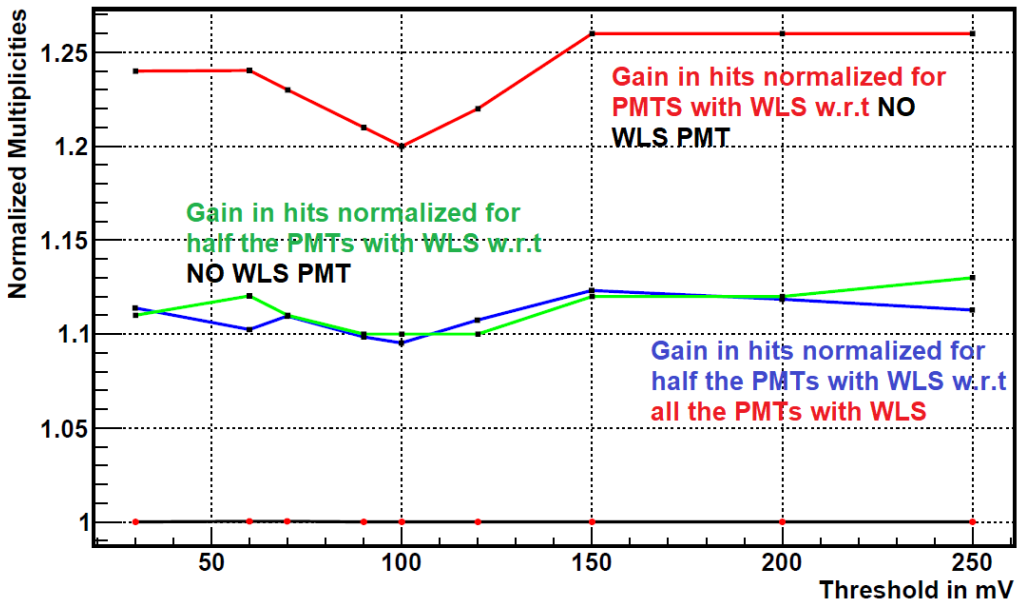

Figure 6.12: Normalized Hit Multiplicity for WLS coated MAPMTs as a function of thresholds. **Note:** No ToT cuts were applied for this particular plot.

6.6 Summary - Time over threshold cuts

6.6.1 ToT cut values

As discussed in the preceding section, the choice of the cut value plays a pivotal role in enhancing the signal-to-noise ratio. The efficacy of different cut values is substantiated by the empirical data presented in Table 6.1. It is important to underscore that the cut is individually defined and implemented for each channel as part of the analysis process. The table also provides insights into the hit losses resulting from the application of Time-over-Threshold (ToT) cuts of varying widths[1].

Table 6.1: Effect of ToT cuts on Hit multiplicity.

Nr	Threshold mV	No cuts	Sigma cut 1 sigma	Sigma cut 2 sigma	Sigma cut 3 sigma	Sigma cut 4 sigma	Sigma cut 5 sigma
1	30	15.74	9.191	10.54	11.08	11.37	11.58
2	40	12.94	9.007	10.39	10.96	11.25	11.44
3	50	12.38	8.836	10.22	10.81	11.11	11.3
4	60	12.18	8.697	10.09	10.68	10.97	11.17
5	70	12.12	8.707	10.11	10.69	10.98	11.16
6	80	12.05	9.654	10.06	10.81	10.88	11.06
7	90	11.9	8.485	9.879	10.41	10.66	10.85
8	100	11.76	8.327	9.688	10.19	10.43	10.65
9	110	11.48	7.992	9.277	9.72	9.99	10.28
10	120	11.12	7.592	8.797	9.24	9.521	9.84
11	150	10.05	6.338	7.388	7.81	8.237	8.66

[1] This table shows the number of hits discarded by the tot cut. It remained open at this stage, if it is only noise hits which are cut away, or maybe also signal hits. However, from HADES test box studies and COSY beam test results, it is safe to assume that a large contribution of hits discarded by ToT cut are crosstalk hits.

The effectiveness of ToT cuts can be understood through the findings presented in Table 6.1. Notably, at higher thresholds, the application of ToT cuts does not yield a discernible advantage and may, in fact, pose a risk of diminishing the detector's efficiency. Conversely, at lower thresholds, particularly at 30 mV, a notable level of noise coexists with the signal. In this scenario, ToT cuts prove highly effective in mitigating the noise.

Additionally, Table 6.1 provides further insights. Within a reasonable threshold range, typically 50 to 70 mV, the recorded number of hits on the detector plane closely aligns with the number of hits predicted by simulations (as detailed in Chapter 2). Notably, simulations assumed 100% collection efficiency of Multi-Anode Photomultiplier Tubes (MAPMTs), which does not align with real-world conditions. Thus, a yield of 12 hits is deemed sufficient for the ring finder to successfully locate and reconstruct the Cherenkov ring.

In all analyses, encompassing ring parameter determination and timing calculations, a ToT cut value of 2.5 sigmas was employed as a standardized benchmark.

6.6.2 Limitations of Time over Threshold (ToT) cuts

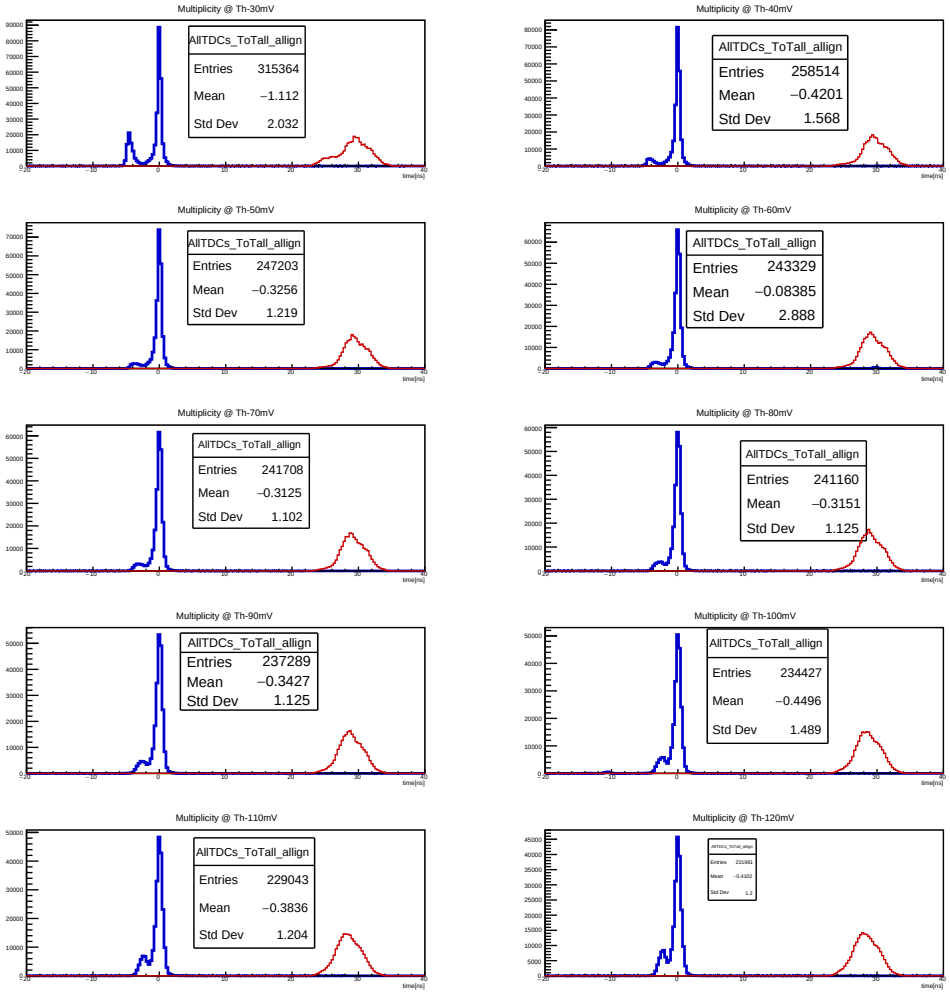

Figure 6.13: Combined time over threshold spectrum for all the channels at different threshold voltages before the alignment (red curve) and after the alignment (blue curve). The X-axis represents the ToT in nano seconds.

The plots depicted in figure 6.13 represent the Time-over-Threshold (ToT) spectra for all channels across a spectrum of operating thresholds. As elaborated in previous sections, it was anticipated that the ToT spectrum should exhibit a dual-peak structure, with one peak corresponding to the primary signal and the other to capacitive crosstalk, distinctively separated. This expectation is validated for low and medium thresholds but becomes less apparent for higher thresholds. A similar phenomenon was also observed during testing in the HADES test box. The capacitive crosstalk, which is notably visible as a distinct peak in the ToT spectrum at lower thresholds, can be effectively mitigated by elevating the operating threshold. However, this comes at the cost of detection efficiency. Therefore, a primary objective of this beam test was to identify the optimal threshold, allowing for crosstalk removal without undue compromise to efficiency.

At higher thresholds (>100 mV), ToT information exhibits signs of deterioration. The absence of significant crosstalk among channels at higher thresholds suggests that a second peak in the ToT spectrum is not anticipated. Nonetheless, as depicted in figure 6.13, a second peak is still evident at higher thresholds, raising questions about the utility of ToT cuts in such scenarios. This behavior poses a certain level of ambiguity, whether it pertains to a hardware feature or an anomaly in the analysis process, and consequently restricts the application of ToT cuts at higher thresholds. As depicted in Figure 6.10, at lower thresholds, multiplicities appear disproportionately high, indicating the presence of noise and crosstalk.

In conclusion, ToT cuts emerge as a highly effective tool for noise and crosstalk suppression when a detector operates at relatively low thresholds. This is particularly beneficial when the detector exhibits a high number of hits at low thresholds, potentially translating to superior efficiency contingent upon the effective suppression of noise. Conversely, at higher thresholds, multiplicities stabilize. Nonetheless, the application of cuts at these higher thresholds inevitably results in a reduction of detected hits, underscoring the compromise to detector efficiency. This highlights the need for careful consideration of the trade-off between noise suppression and detector efficiency when applying ToT cuts.

6.7 Ring parameters

After completing the initial tests, the incorporation of the ring fitting algorithm into the analytical framework commenced. This algorithm, as developed by Lebedev (2010) [LHO+10], is instrumental in the analysis of data. It systematically compiles timestamps associated with the recorded hits within a given event. Comprehensive data on these hits, encompassing their time of arrival at the trigger point (in this instance, the hodoscope), their X-Y positional coordinates, and the leading-trailing edge time for each individual hit, is meticulously preserved.

In conjunction with the algorithm, a dedicated geometry file featuring the X-Y coordinates of the pixels on the Multi-Anode Photomultiplier Tubes (MAPMTs) in the beam direction was integrated into the Go4 analysis tool. This supplementary dataset serves to precisely determine the position of each hit. By identifying the specific pixel that registered a hit and discerning its X-Y coordinates, the exact location of each hit on the 2D MAPMT map for a given event can be established.

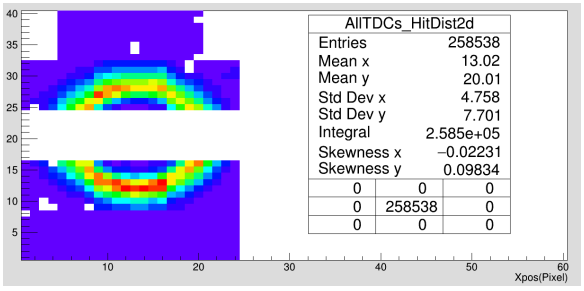

Figure 6.14: Reconstructed 2D ring image for all the events at operating threshold of 30 mV.

Figure 6.14 illustrates a 2D plot comprising 20,000 events that have undergone reconstruction within the Go4 framework. On this plot, the X-axis corresponds to the X-position of the recorded hits, while the Y-axis represents the Y-position. The units used here are pixel numbers, with each pixel approximately equivalent to 0.55 mm in metric terms.

The backplane configuration consists of 3×2 MAPMTs, resulting in an X-axis range spanning from 1 to 24 pixels (representing 3 MAPMTs of 8 pixels each) and a vertical height of 16 pixels (representing 2 MAPMTs of 8 pixels each). A 5 cm gap has been maintained between the two modules to allow for the passage of the particle beam. These dimensions are consistent for the upper module as well. Therefore, the Y-axis extends from 1 to 16 pixels, encompassing the gap (5 cm), and from 25 to 40 pixels. It is worth noting that the three distinct figures may not effectively demonstrate the influence of Time-over-Threshold (ToT) on the reconstructed ring. However, a single-event plot in figure 6.17 effectively exemplifies how the application of a ToT cut operation eliminates extra hits and minimizes crosstalk.

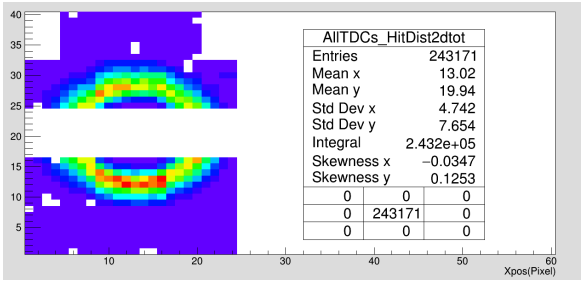

Figure 6.15: Reconstructed image of all the events at at 30 mV after applying ToT cuts.

Figure 6.15 shows the 2D plot of same events as shown in figure 6.14 after applying ToT cut. Once can see the effect by decrease in the number of entries. The ring characteristics significantly improves which can be seen by studying single event plots of each event, discussed in next section. A more interesting effect can be seen in figure 6.16 which shows the2D plot of hits rejected due to the implementation of the ToT cut. The rejected hits also resemble a ring as the probability of having a crosstalk is highest in the neighboring pixel.

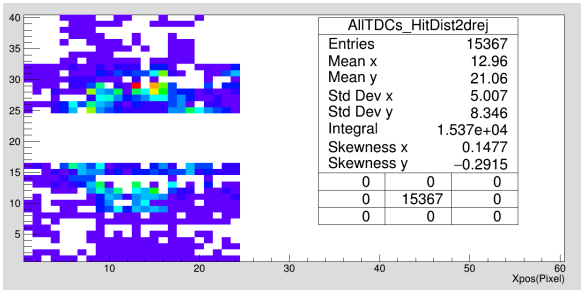

Figure 6.16: Reconstructed 2D ring image for all the events at operating threshold of 30 mV, rejected by ToT cuts.

Table 6.2: Effect of ToT cuts on Ring parameters.

	X-Center	Y-Center	Ring radius	No. of hits in ring
No ToT cut	8.8	13.7	6.48	23
With ToT cut	7.43	13.3	5.66	18

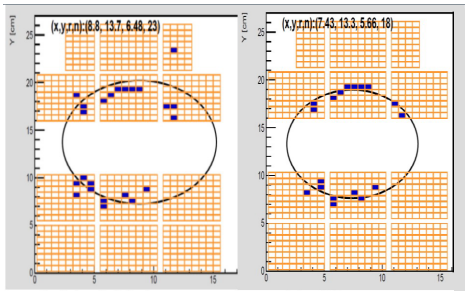

(a) Event display with and without ToT cut

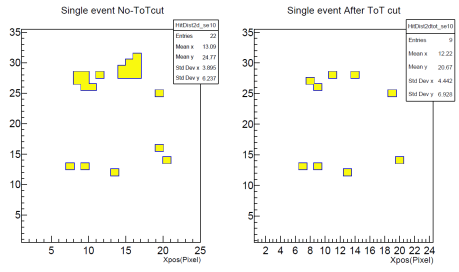

(b) Single event plot with and without ToT cut

Figure 6.17: (a) Go4 image of the event display showing ring finder fitting the ring over the hits without ToT cut (left) and with ToT cut (right) (b) Single event plot of one of the event showing the effectiveness of ToT cut. Operating threshold - 30 mV.

Figure 6.17 exemplifies the substantial impact of the ToT cut on the fitted ring. This is reflected in marked differences in the values for X-Y centers, radius, and the number of hits when comparing fitted rings with and without the ToT cut. Notably, even after the reduction in the number of hits following the ToT cuts, the ring fitter consistently achieves superior ring fitting results compared to scenarios without ToT cuts. For reference, the tabular representation of the values presented in Figure 6.17(a) is provided in Table 6.2 for comparative purposes.

A Cherenkov ring produced in this beam test is circular in shape. Based on simulations, it was known that there would be one ring covering the whole MAPMT plane. The quality of the ring can be estimated based on the following parameters of the ring.

X-Centre: As discussed earlier, the horizontal width of the MAPMT plane was 15 cm, and the height was 25 cm approx. Thus we expect the ring centre in a horizontal direction to be around 7.5 cm.

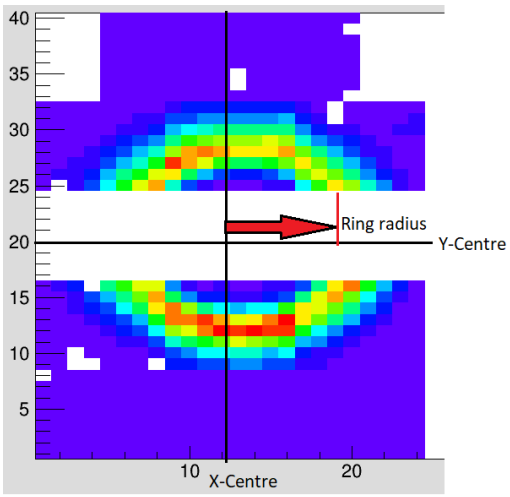

Figure 6.18: Schematic diagram showing ring position in XY-plane.

Y-Center: The Y-Centre of the MAPMT plane is around 12.5 cm.

Ring Radius: The ring produced using proximity focusing quartz ring is not a sharp ring, thus as per the simulations,th radius of the ring is calculated as the radius from the inner circle of the ring which is around 6 cm as per the simulations.

dR of ring: The efficiency of the ring-finding process is evaluated by considering the 'dR' parameter, which denotes the distance of hits that deviate from the fitted ring. In essence, it measures how well the ring fitter can accommodate hits that do not precisely align with the fitted ring. A smaller dR value indicates an effective ring fitting process. Additionally, it is pertinent to note that the presence of extra hits, such as noise, can detrimentally impact the dR parameter of the ring, as visualized in figure 6.17(a).

6.7.1 X-Center

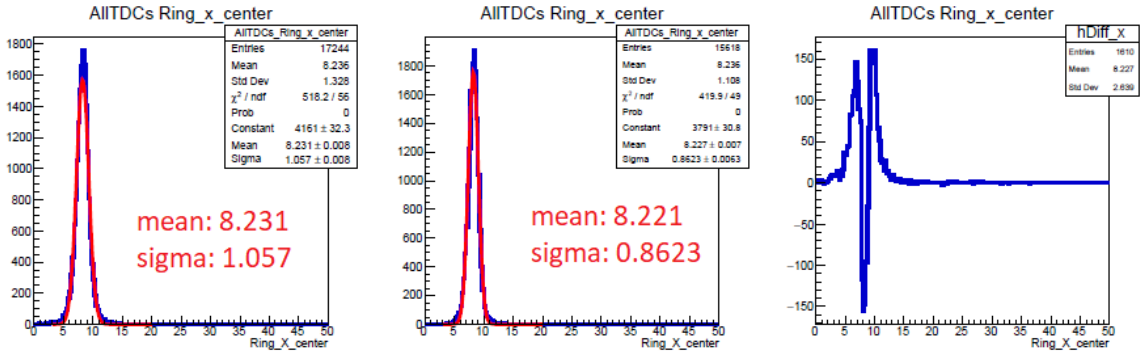

(a) Without ToT cut (b) With ToT cut (c) Rejected hits

Figure 6.19: **Operating Threshold: 30 mV**(a) X-Centre of ring without ToT cut (b) X-Center of ring after 2 sigma ToT cut (c) Difference of (a) and (b) showing rejected hits due to ToT cut.

A comparative analysis between figure 6.19 and figure 6.20 underscores the impact of the Time-over-Threshold (ToT) cut on X-center approximation. At a lower threshold of 30 mV, the ToT cut

leads to an enhancement in X-center accuracy, while at a higher threshold of 120 mV, it results in a deterioration of X-center accuracy.

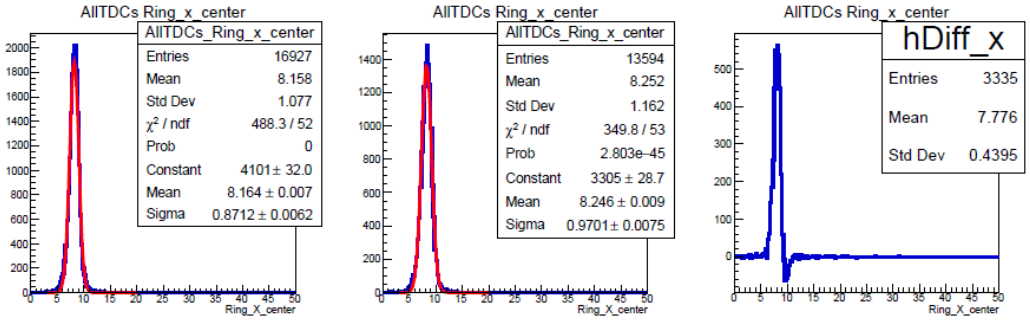

(a) without ToT cut (b) with ToT cut (c) rejected hits

Figure 6.20: **Operating Threshold: 120 mV**(a) X-Centre of ring without ToT cut (b) X-Center of ring after 2 sigma ToT cut (c) Difference of (a) and (b) showing rejected hits due to ToT cut.

This observation is further supported by the sigma values corresponding to the fitted peak of the X-center at 30 mV and 120 mV, as illustrated in figure 6.19 and figure 6.20, respectively. The sigma value at the lower threshold exhibits an improvement following the application of the ToT cut, whereas at the 120 mV threshold, the sigma deteriorates post-ToT cut. Notably, the difference plots in these scenarios reveal the presence of hits other than the central peak.

In the context of a 30 mV threshold, the ToT cut effectively eliminates unwanted hits, as evidenced by the difference plots. However, at the 120 mV threshold, a different narrative unfolds. Here, the sigma value experiences a decline post-ToT cut, and the difference plot aligns with the patterns observed in previous plots, strongly suggesting that the ToT cut effects on detection efficiency.

6.7.2 Y-centre

In case of Y-centre, it is similar result. When ToT cut is applied at low threshold Y-centre approximation improves (Fig. 6.21 (b)) and at a higher threshold, it worsens (Fig. 6.22 (b)). The difference plot also is similar in the sense that for low threshold (Fig. 6.21 (c)) it shows the rejected hits and for higher threshold (Fig. 6.22 (c)) it looks similar to the signal peaks.

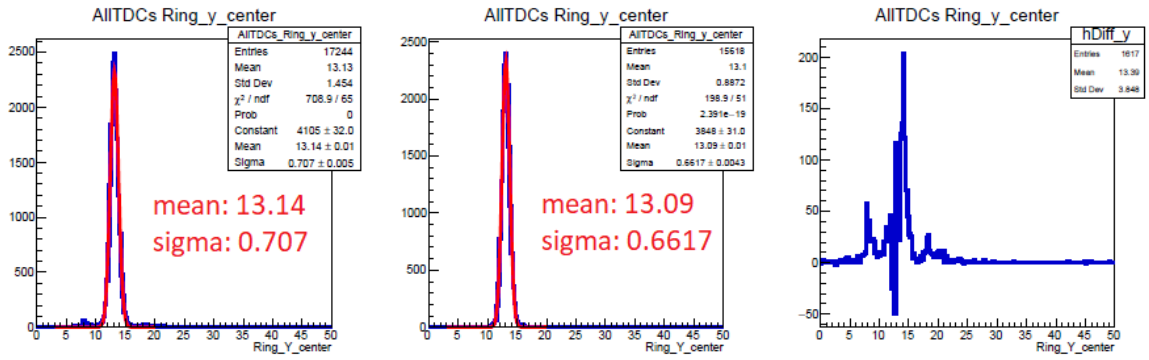

(a) Without ToT cut. (b) With ToT cut. (c) Rejected hits.

Figure 6.21: **Operating Threshold: 30 mV**(a) Y-centre of ring without ToT cut (b) Y-center of ring after 2 sigma ToT cut (c) Difference of (a) and (b) showing rejected hits due to ToT cut.

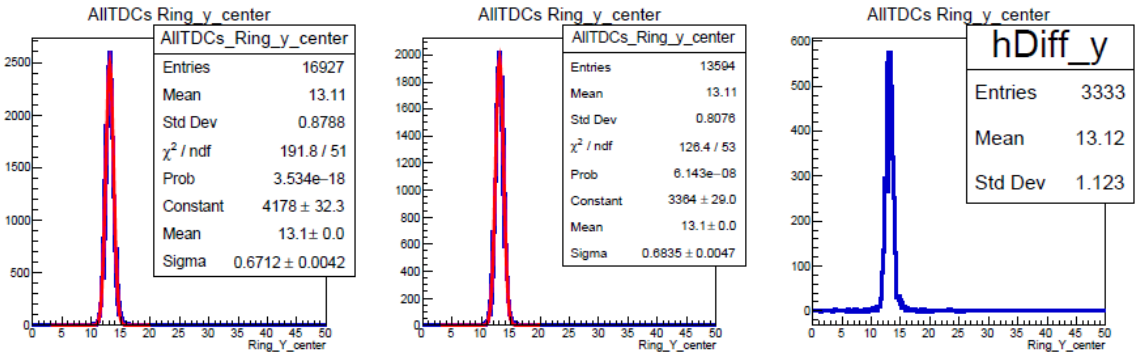

(a) Without ToT cut. (b) With ToT cut. (c) Rejected hits

Figure 6.22: **Operating Threshold: 120 mV** (a) Y-centre of ring without ToT cut (b) Y-center of ring after 2 sigma ToT cut (c) Difference of (a) and (b) showing rejected hits due to ToT cut.

6.7.3 Ring Radius

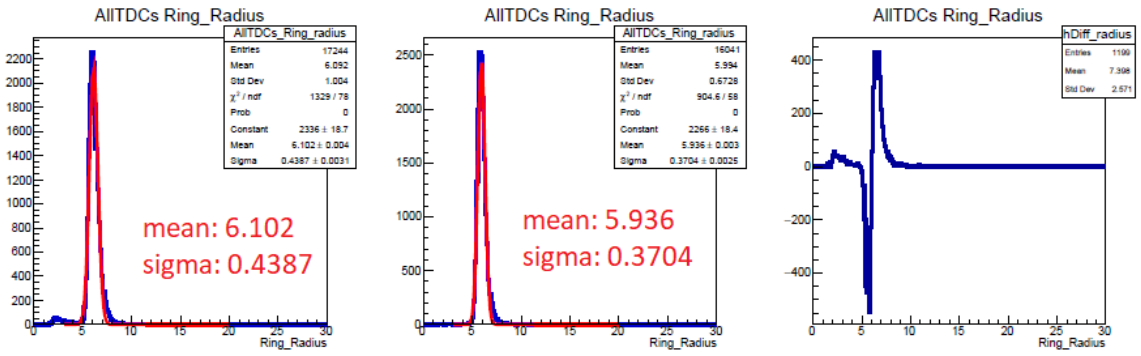

(a) Without ToT cut. (b) With ToT cut. (c) Rejected hits.

Figure 6.23: **Operating Threshold: 30 mV**(a) Radius of the ring without ToT cut (b) Radius of the ring after 2 sigma ToT cut (c) Difference of (a) and (b) showing rejected hits due to ToT cut.

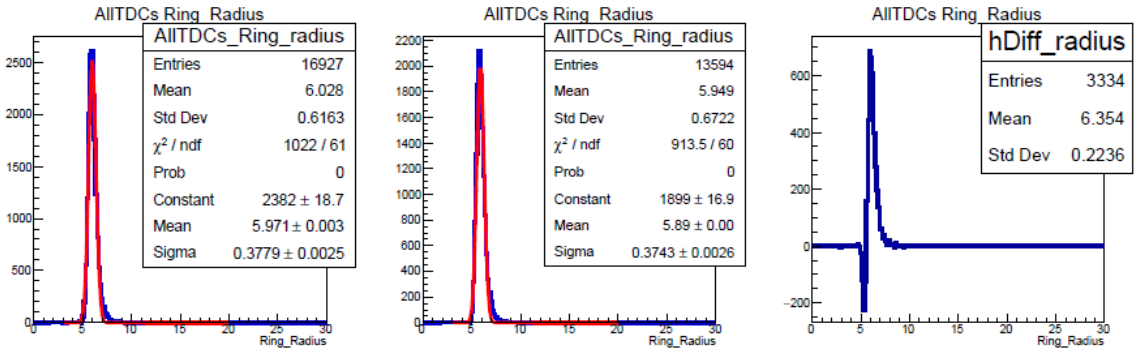

(a) Without ToT cut. (b) With ToT cut. (c) Rejected hits.

Figure 6.24: **Operating Threshold: 120 mV**(a) Radius of the ring without ToT cut (b) Radius of the ring after 2 sigma ToT cut (c) Difference of (a) and (b) showing rejected hits due to ToT cut.

According to the simulations, the anticipated value of the ring radius in the COSY beam test was 6 cm. As depicted in figure 6.23, this value was meticulously derived from the observed hit pattern. A similar methodology was employed for the application of a Time-over-Threshold (ToT) cut to the ring radius, akin to the treatment undertaken for the X- and Y-center parameters. The results indicate that the radius approximation exhibits notable improvement following the application of the ToT cut at lower thresholds. However, at higher thresholds, as illustrated in Figure 6.24, the gain in approximation is not as substantial.

6.7.4 dR of the Ring

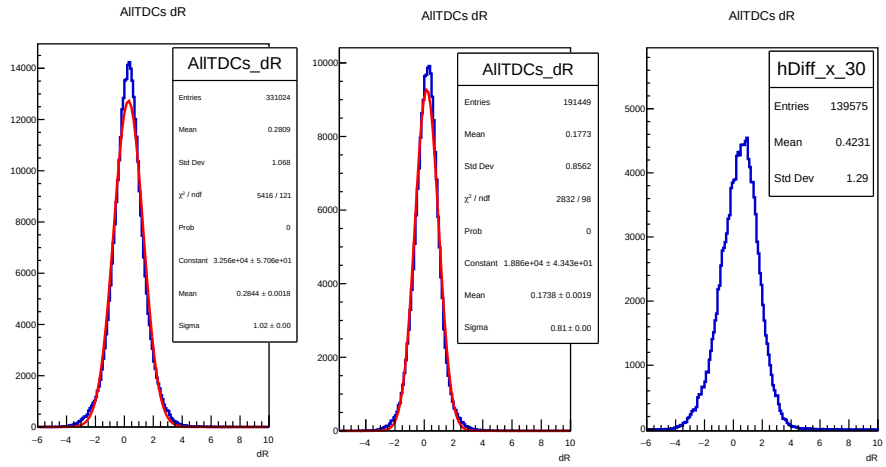

(a) Without ToT cut. (b) With ToT cut. (c) Rejected hits.

Figure 6.25: **Operating Threshold: 30 mV** (a) dR of the ring without ToT cut (b) dR of the ring after 2 sigma ToT cut (c) Difference of (a) and (b) showing rejected hits due to ToT cut.

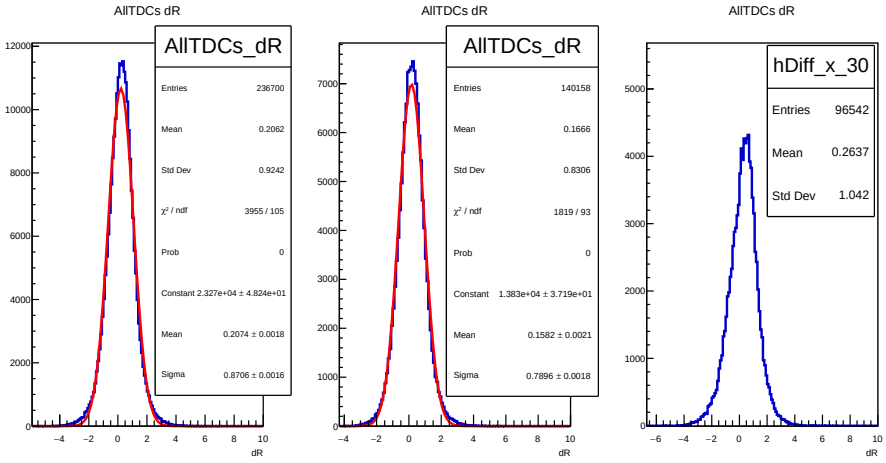

(a) Without ToT cut. (b) With ToT cut. (c) Rejected hits.

Figure 6.26: **Operating Threshold: 120 mV** (a) dR of the ring without ToT cut (b) dR of the ring after 2 sigma ToT cut (c) Difference of (a) and (b) showing rejected hits due to ToT cut.

The 'dR' value serves as a critical determinant in assessing the quality of the ring fit. It provides insight into the accuracy of the ring's alignment with respect to the hits detected on the Multi-

Anode Photomultiplier Tube (MAPMT) plane. The calculation of 'dR' involves determining the perpendicular distance of each hit from the fitted ring and subsequently calculating the difference between this distance and the ring radius. If a hit lies precisely on the fitted ring, this difference will equate to zero; however, in cases where the hit deviates from the fitted ring, the difference will be distributed around the zero position (as illustrated in Figure 6.25 and 6.26). The 'dR' value indirectly influences all the previously discussed ring parameters. Accurate determination of 'dR' is paramount, as any discrepancies will propagate errors in the calculation of other ring parameters.

Figure 6.25 & 6.26 represents the dR plot for two different threshold of 30 mV and 120 mV respectively. One can conclude from these plots that at a lower threshold the sigma value of dR is improved significantly after applying ToT cut. The same was not the case when ToT cut was applied at a higher threshold. Unlike other parameters such as X and Y centers dR sigma relatively remains constant once the excess noise hits are removed. This is also shown quantitatively in figure 6.27 in black curve.

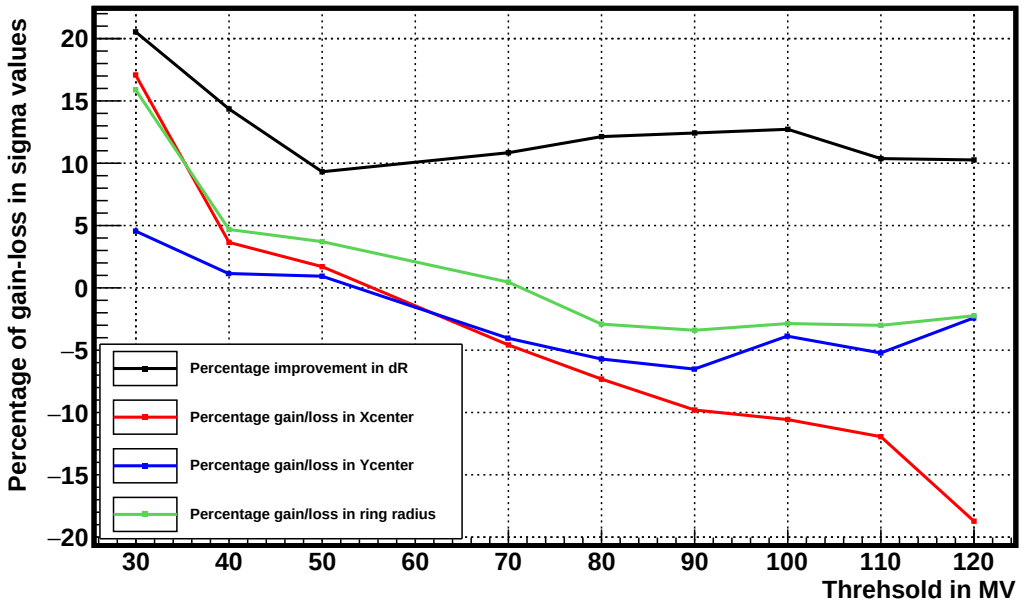

Figure 6.27: Gain and loss in calculating the ring parameter based on the sigma values due to implementation of ToT cut.

When we plot the sigma values for all the ring parameters, we obtain figure 6.27. This figure illustrates the percentage change in the sigma values concerning the operating threshold. A smaller sigma value signifies a better fit, resulting in a more accurate approximation of the respective ring parameter. For instance, the red curve in figure 6.27 represents the ratio of X-center without ToT cut to the X-center with ToT cut. Positive values in plot indicate an improvement in the sigma value, thereby enhancing the precision of the corresponding ring parameter, while negative values signify a decrease in the sigma value, implying a degradation in the fit quality following the implementation of the ToT cut. A similar methodology was applied in generating plots for the remaining ring parameters.

Figure 6.27 offers valuable insights, indicating that the effectiveness of the ToT cut is most pronounced up to an operating threshold of 70 mV. Beyond this threshold, there is limited discernible enhancement in signal quality.

6.8 Effect of Wavelength shifting coating (WLS)

In section 4.3.1 there was a short description of WLS coating and its effect on hit multiplicity 6.5.1. The main idea for using WLS coating was to improve the number of hits or in other words to increase the efficiency of the detector. WLS paint is a thin layer of paint which is coated externally on the external glass of MAPMT. This paint is an organic compound called p-terphenyl and has a unique property that it absorbs the UV light and emits again in the visible region. The reason to use this particular compound and its other properties can be referred at [Kop14].

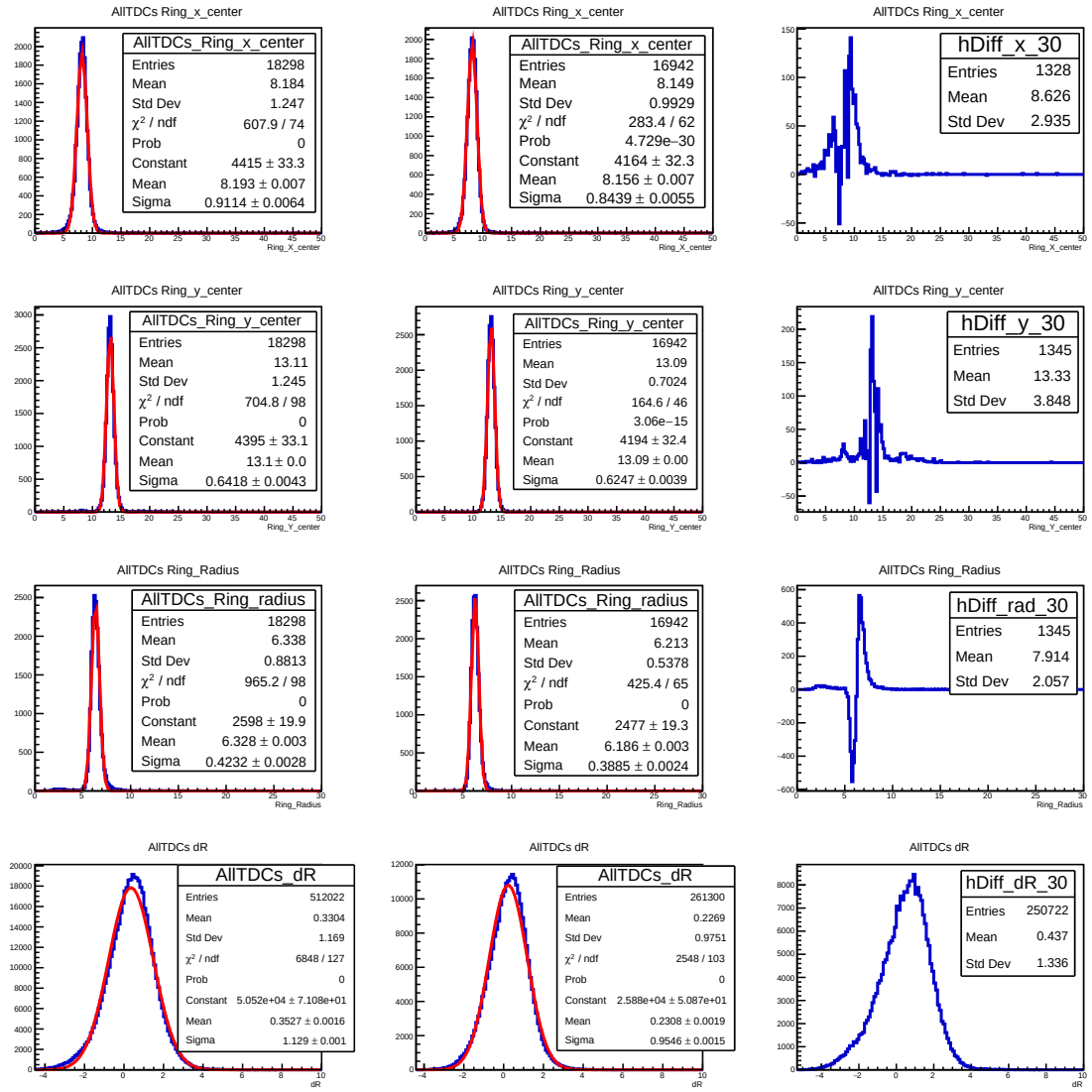

Figure 6.28: Ring parameters for MAPMTs with WLS coating at threshold of 30 mV. Each row in the figure represents one ring parameter and has three plots. The leftmost plot is without any ToT cut, middle one is with the ToT cut and the rightmost is difference first two plots showing the rejected hits. The first row is X-centre of the ring; second row is Y-centre, the third row shows ring radius and the last row shows dR values.

In this section, only the effects of WLS coating is discussed. For COSY beam test a 100 nm layer of WLS was coated on a MAPMT by dipping it in a solution of p-terphenyl via machine-controlled apparatus to get an optimum thickness [Web21] The effect discussed in section 4.3.1 shows that

Table 6.3: Effect of WLS coating on the ring parameters expressed in terms of sigma @ 30 mV.

Ring Parameters	WLS (sigma)		No-WLS (sigma)	
	No ToT Cuts	With ToT Cuts	No ToT Cuts	With ToT Cuts
X center	0.91	0.84	1.05	0.86
Y center	0.64	0.62	0.70	0.66
Ring Radius	0.42	0.38	0.43	0.37
dR	1.13	0.95	1.02	0.81

there is a gain of 20% of photons for the MAPMTs coated with WLS paint, but it does not define the ring quality. The effect of WLS coating on the ring parameters can be seen in the figure 6.28. It shows all the ring parameters for WLS coated MAPMTs at 30 mV threshold.

On inspecting figure 6.28, it gives an idea that ring parameters such as X-Y centre, and the ring radius has no effect of WLS coating. On the other hand, the dR value has a slight deterioration due to WLS. The sigma value of the fitted dR curve is slightly worse for WLS coated MAPMTs. It hints that the gain in hits due to WLS affects the ring fitting in the analysis. Table 6.3 refers to the sigma value of all the ring parameters for WLS and NO-WLS MAPMTs when operated at the threshold of 30 mV. This is similar pattern for all other thresholds since there is absolute gain of 20% of photons due to WLS. Apart from dR, WLS has a significant effect on a crucial parameter which will be discussed in the next section.

6.9 Time precision

As explained in Chapter 3, the fundamental objective in the development of DiRICH readout electronics was to create a readout device capable of precisely measuring leading and trailing edge times. In the context of DiRICH, timing is assessed through an onboard Field-Programmable Gate Array (FPGA) [BBD+23]. Consequently, one of the primary motivations behind conducting this comprehensive beam test was to evaluate the performance of DiRICH under real beam conditions. Preliminary tests carried out in the HADES test box had yielded promising results, wherein a time precision of 400 picoseconds (FWHM) was achieved using a laser source. It is noteworthy that, during these initial tests, the FPGA remained unprogrammed, and the timing measurements were made externally utilizing an oscilloscope. In the subsequent COSY beam test, the FPGA was fully operational, allowing for timing measurements to be executed in accordance with the FPGA-Time-to-Digital Converter (FPGA-TDC) methodology [T+14]. It is noteworthy that every dirich channel has a small, but individual time offset of few ns (due to internal fpga structures and delays). The goal of this whole procedure is to calibrate these individual time offsets, to achieve coincident time measurement for coincident hits over all channels in the setup.Thus, in this particular beam test, two distinct approaches were employed to determine time precision.

Average approach: For the this approach, the following steps were taken:

1. The implementation of a Time-over-Threshold (ToT) cut was a crucial step to ensure the integrity of the data by eliminating potential crosstalk and noise.
2. For each event, the ring-finding algorithm is utilized to identify the Cherenkov ring, and all relevant parameters are recorded, with particular emphasis on capturing the leading-edge timing information of the hits, which are subsequently saved in a text file.
3. Within each event, the average timing of all these hits is computed.
4. Subsequently, the timing of each hit within the ring is offset by subtracting the event's average timing. These differences are stored in a distinct text file, collecting for each channel individually the leading edge time difference of registered cherenkov photons in this particular channel with respect to the average time of all hits in the same ring. This offset represents the timing discrepancy, and its sigma value is used to quantify the precision of the timing information.

5. Step 4 is iteratively repeated in five cycles until further improvement in the sigma value is no longer attainable. This iterative approach ensures that the timing precision is optimized to its fullest extent.

The process mentioned above is explained with the following example. Figure 6.29(a) shows a 2D plot of leading-edge timing distribution without any offset correction, as mentioned in step 4. After five iterations of corrections by repeating the above steps, the same plot can be improved, as shown in figure 6.29 (b).

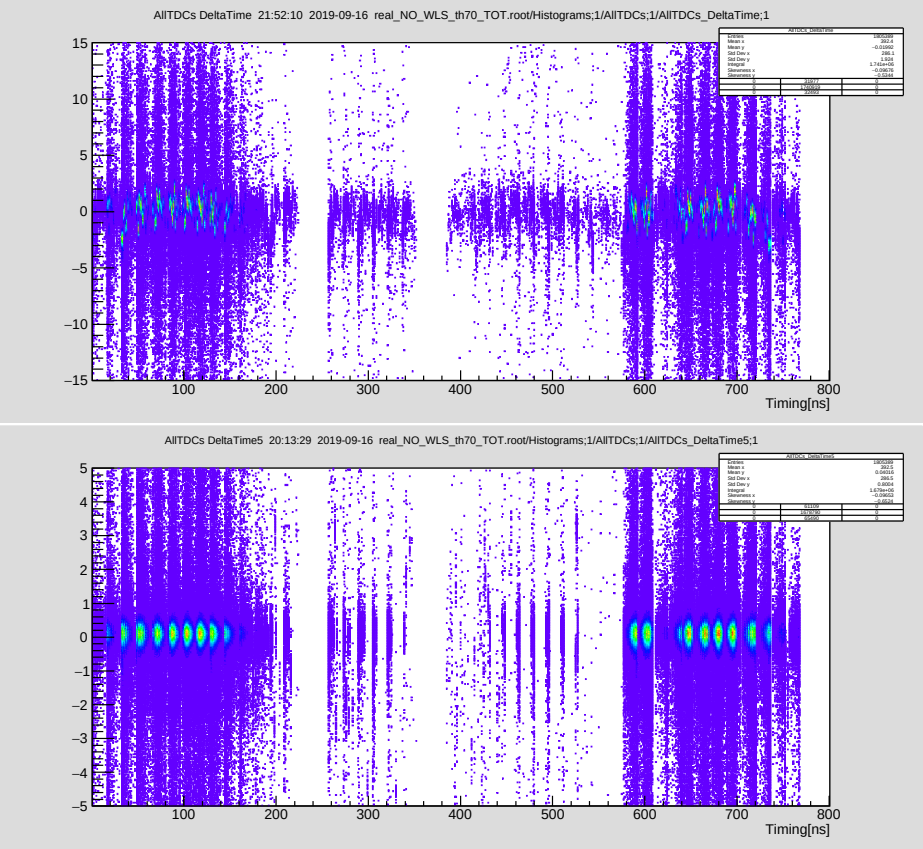

Figure 6.29: 2D image of leading edge timing relative to the average time of all hits within the Cherenkov ring,for a threshold of 70 mV, without correction (top plot) and correction after 5 iterations (bottom plot).

The Y-projection from each of these plots is harnessed to calculate the time precision of the detector. Illustrated in figure 6.30, the timing correction evolution is depicted. In the first plot, the timing offset for the initial iteration (zeroth iteration) is presented, representing the disparity between the average timing and the individual timing for each hit within the ring. The X-axis is a temporal scale centered around zero in nanoseconds (ns).

Upon fitting, the parameters of the fit are stored as offsets in a separate file. Subsequently, for each hit located within the ring, an associated offset value is applied, adjusting the timing. The mean of these corrected timing values is computed, constituting one iteration of correction. This iterative process is repeated five times, progressively eliminating offsets and fine-tuning timing. A comparison between the initial and fifth plots in figure 6.30 reveals a substantial improvement in timing, quantified by the sigma value, with an enhancement of approximately 25%.

In an ideal detector, it is expected that all the Cherenkov photons for a single Cherenkov ring arrive on MAPMT at the same time hence the time offset between each of the hits would be zero. However, in practical applications, several factors contribute to the time precision of the detec-

tor. These include the time required for the detector to process incoming signals, the subsequent signal transmission through the readout chain, and the processing time within the electronics to render the signal in a readable format. All these elements collectively influence the detector's time precision.

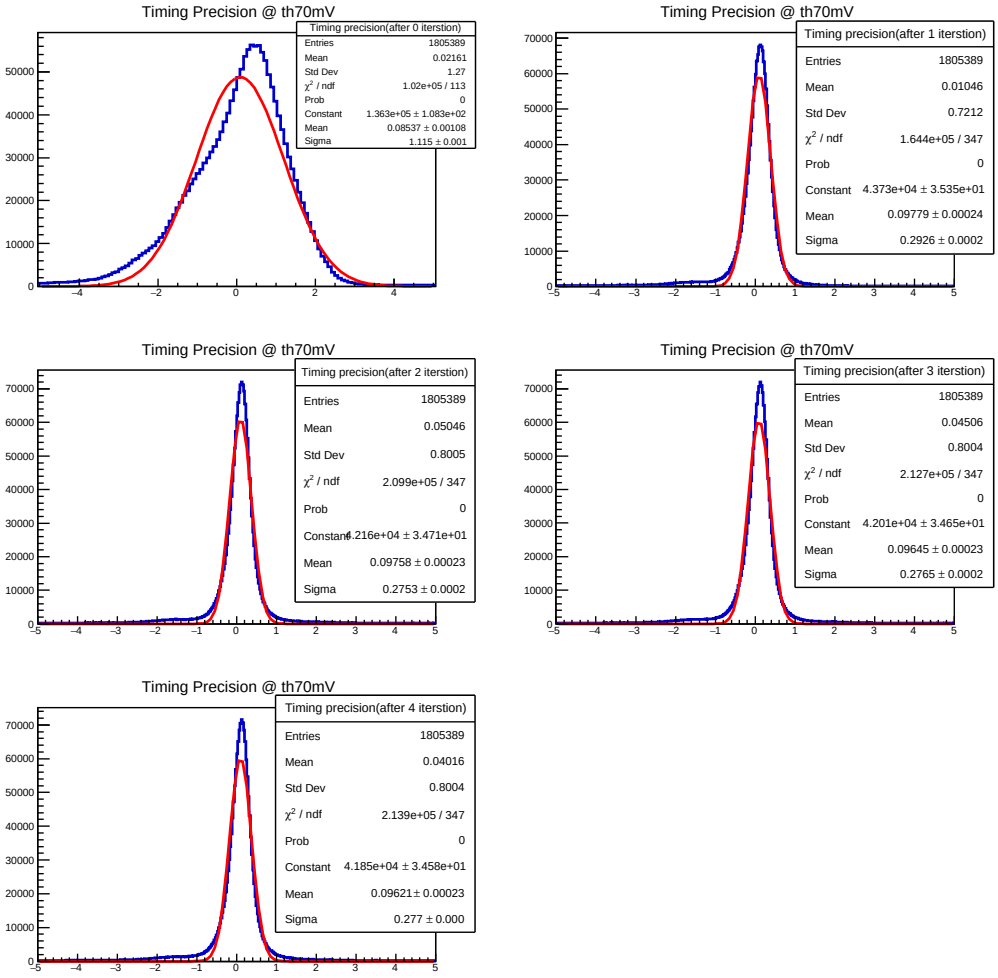

Figure 6.30: Evolution of improvement in time-precision measurment using the methodology described in above section **Average approach**. Each plot in the figure represents one iteration of all the steps mentioned above. The final plot represents the final iteration after which there is no further improvement of time-precision possible. The plots are for the data taken at 70 mV threshold voltage.

In our specific case, the Multi-Anode Photomultiplier Tubes (MAPMTs) exhibit a transit time spread (TTS) of 350 picoseconds (ps) (FWHM). TTS represents the inherent time response of the MAPMT, signifying the spread or variation in time it takes for the signal to traverse the MAPMT and reach the readout electronics. As a result, the time precision is inherently bounded by the detector's intrinsic time resolution and the TTS of the MAPMT.

Considering these factors, the expected time precision in our case should be greater than 350 ps (FWHM). As depicted in figure 6.30, after undergoing five iterative corrections, the sigma value of the time correction plot reaches 277 ps. Consequently, the Full Width at Half Maximum (FWHM) can be calculated as 2.303×277, resulting in a value of 637.931 ps. Here we measure individual hit times vs the average time of all hits. Depending on the total number of hits in the ring, the error

of this average time is reduced by a factor of sqrt(n) such that only the individual channel timing precision is the contributing factor.

Furthermore, by comparing these results with the data obtained from the HADES test box, it becomes evident that the timing outcomes from both tests are consistent with each other. This congruence underscores the effectiveness of the readout's design and its successful performance under real-world conditions, validating its intended functionality.

Table 6.4: Time precision at different thresholds.

Threshold	Sigma (ps)	Time precision - FWHM (ps)
30	277	637.93
40	265	610.29
50	299	688.59
60	293	674.77
70	272	626.41
90	273	628.71
100	297	683.99
120	311	716.23
150	330	759.99

The process discussed above represent only one threshold setting in which the time precision calculated by taking the average of all the hits in the ring and following the process mentioned above. Table 6.4 shows Time precision for each value of threshold and it lies between 600-700 ps which is acceptable for CBM and HADES experiments.

Median approach: The second approach involved employing the median as an alternative to the average. This approach is more suitable for the WLS coated MAPMTs. In WLS coated MAPMTs, for the same ring, the gain in the multiplicity due to extra conversions of UV-photons comes at the price of delay in their arrival at the DiRICH. This delay hence converts to worse time precision measurement. Thus, when calculating the average, the presence of delayed hits attributable to Wavelength Shifting Coating (WLS) introduces a timing delay that influences the computed average. To mitigate this effect to some extent, median of timing can be used instead of mean as median is inherently resistant to the outliers. As previously explained, the application of WLS coating yields an increase in hit efficiency by 18-20%. For instance, if the initial hit multiplicity is 12, the introduction of WLS raises it to 14 hits. This increase results in disparate average timings for the 12 hits, while the median remains more centered and less influenced by the effects of the two delayed hits caused by WLS.

Table 6.5: Time precision at different thresholds comparing the effect of average approach and meadian approach for the PMTS without WLS coating.

Ring Parameters	Average approach		Median approach	
	Sigma (ps)	FWHM (ps)	Sigma (ps)	FWHM (ps)
30	273	628	202	465
40	263	606	203	468
50	299	689	205	472
60	293	675	209	481
70	276	636	213	491
90	273	629	218	502
100	297	684	223	514
120	311	716	218	502

From figure 6.31 it is evident that the utilization of the median approach demonstrates a sig-

nificant improvement over the use of the average since the standard deviation and hence the time precision is better when considering median of the hit distribution.

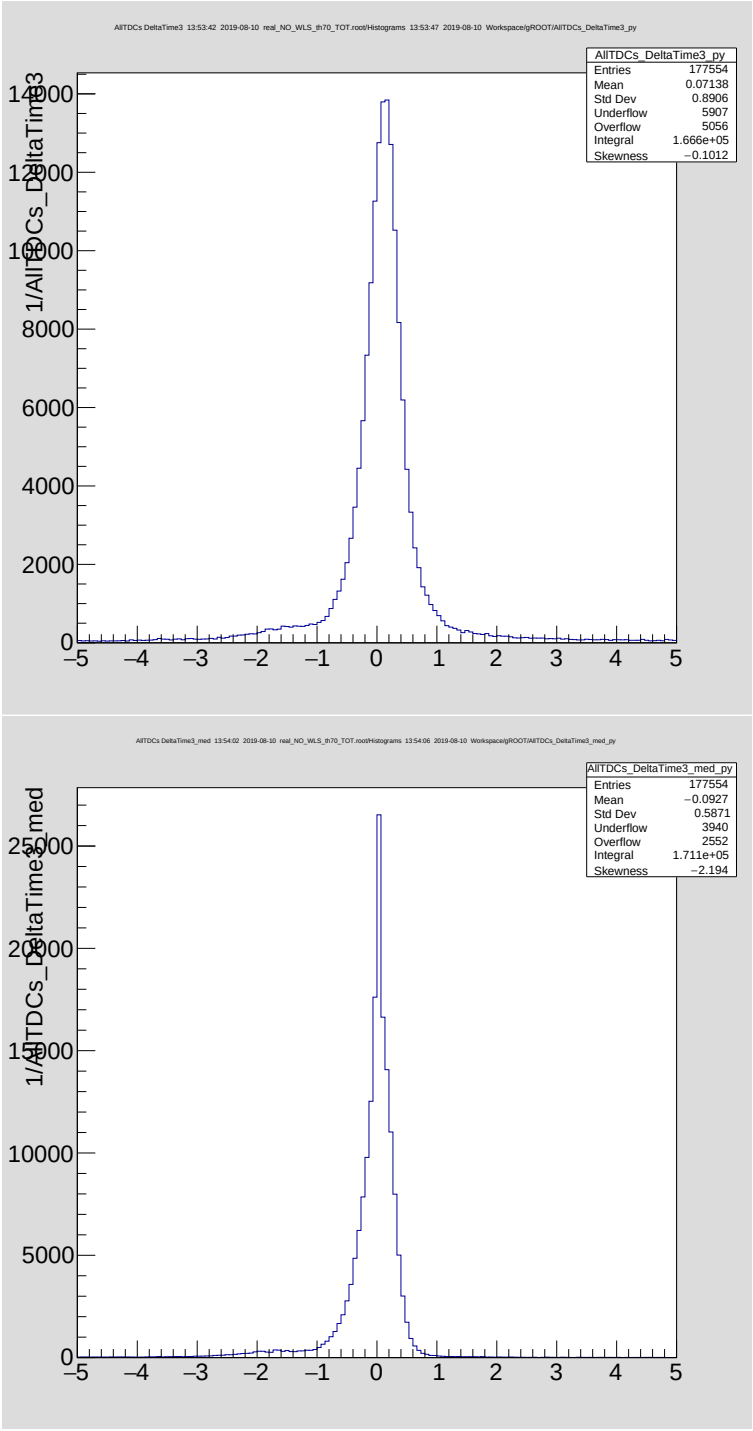

Figure 6.31: Comparison of average approach (top plot) with the median approach (bottom) to calculate time precision. Both plots represent the data for the threshold value of 70 mV with MAMPMTs with no WLS coating.

In figure 6.31 the top plot shows the statistics of average approach and the bottom plot shows

that of the median approach. As one can see, the amount of statistics is same for both the plot but median approach has better standard deviation of around 580 ps compared to 890 ps for the average approach. The methodology for computing timing using the median follows the same steps as the approach using the average, with the sole distinction being the application of the median to correct offsets instead of the average.It is noteworthy that these plots represent only two iteration of the the method discussed in above.

6.9.1 WLS & Time precision

Applying the same approach to WLS-coated MAPMTs, the calculated time precision was notably worse than that achieved with non-WLS MAPMTs.

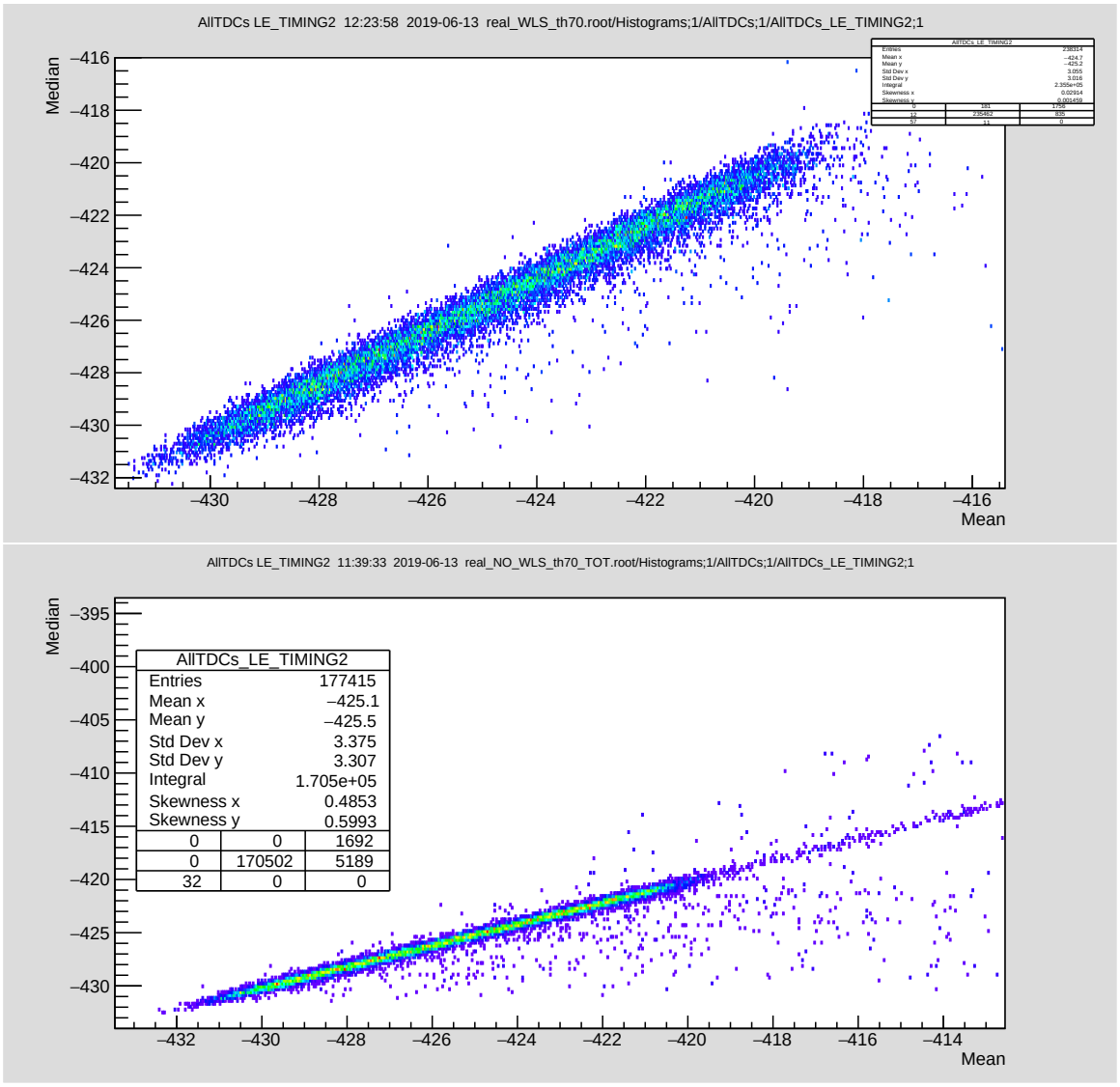

Figure 6.32: Comparison of using the ”mean” method to calculate the average time value (upper plot) and using the ”median” approach(lower plot) for data obtained with WLS-coated MAPMTs for the threshold of 70 mV.

One can see that from the figure 6.32 that for WLS mean median ratio is scattered broadly compared to non-WLS coated MAPMTs for the same value of threshold. This confirms the fact that

WLS affects the time precision severly.

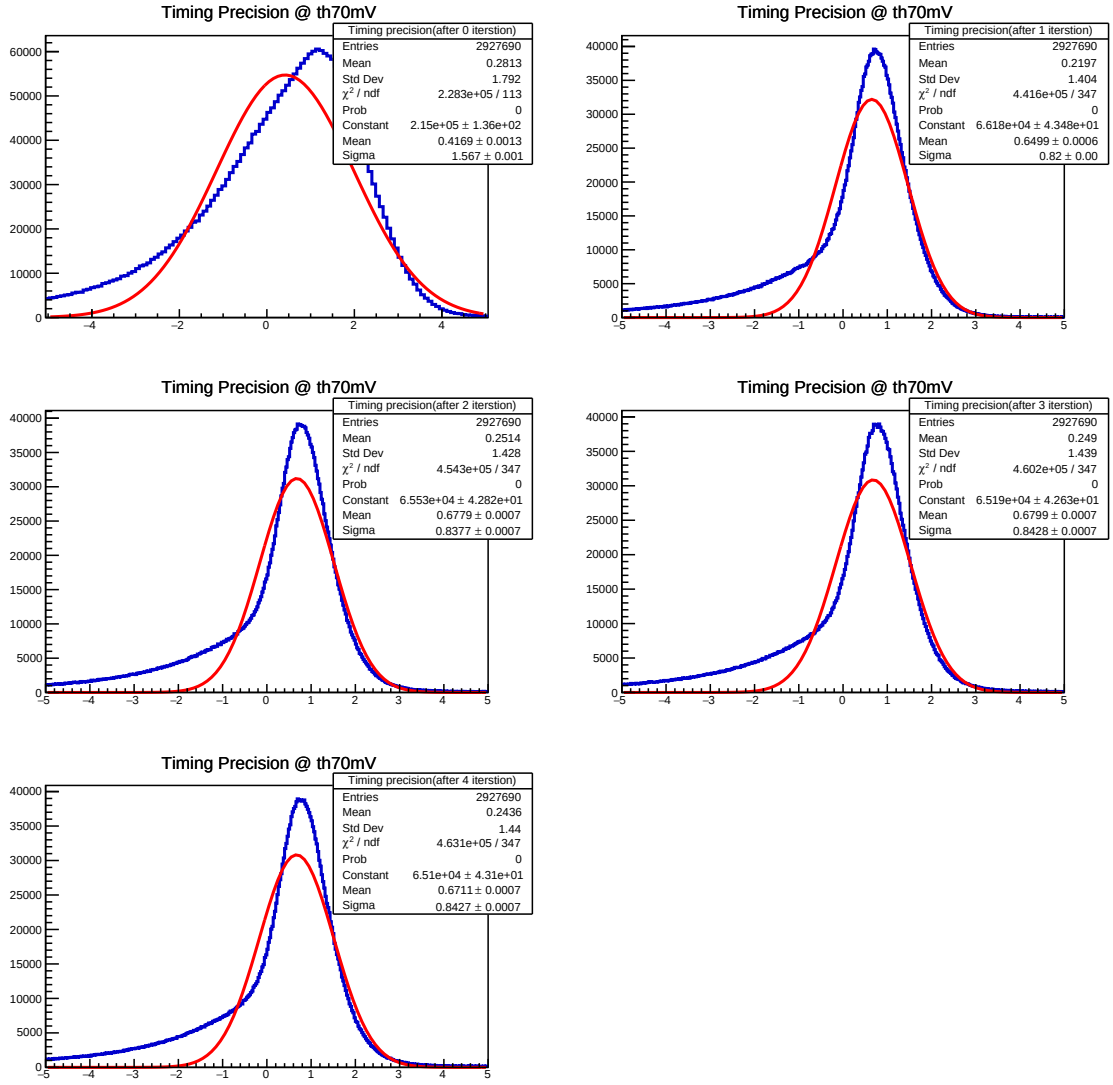

Figure 6.33: Evolution of improvement in time-precision measurment using the methodology described in above section. Each plot in the figure represents one iteration of all the steps mentioned above. The final plot represents the final iteration after which there is no further improvement of time-precision possible. The plots are for the data taken for WLS coated MAPMTS at 70 mV threshold voltage.

As evident in figure 6.33, after undergoing five iterative corrections, the timing correction curve assumes a distinct profile compared to that observed with non-WLS MAPMTs. Notably, the curve exhibits a deviation from the expected Gaussian distribution due to the presence of an antecedent exponential component. This deviation arises from the interaction of WLS paint with incident UV photons, leading to their absorption and subsequent emission in the visible region. This process, characterized by a finite time interval, results in delayed hit reception. This delay can be well over 1 ns [Web21]. As previously explained, the method involves computing the average timing of all hits and then subtracting the timing of each individual hit from this average.

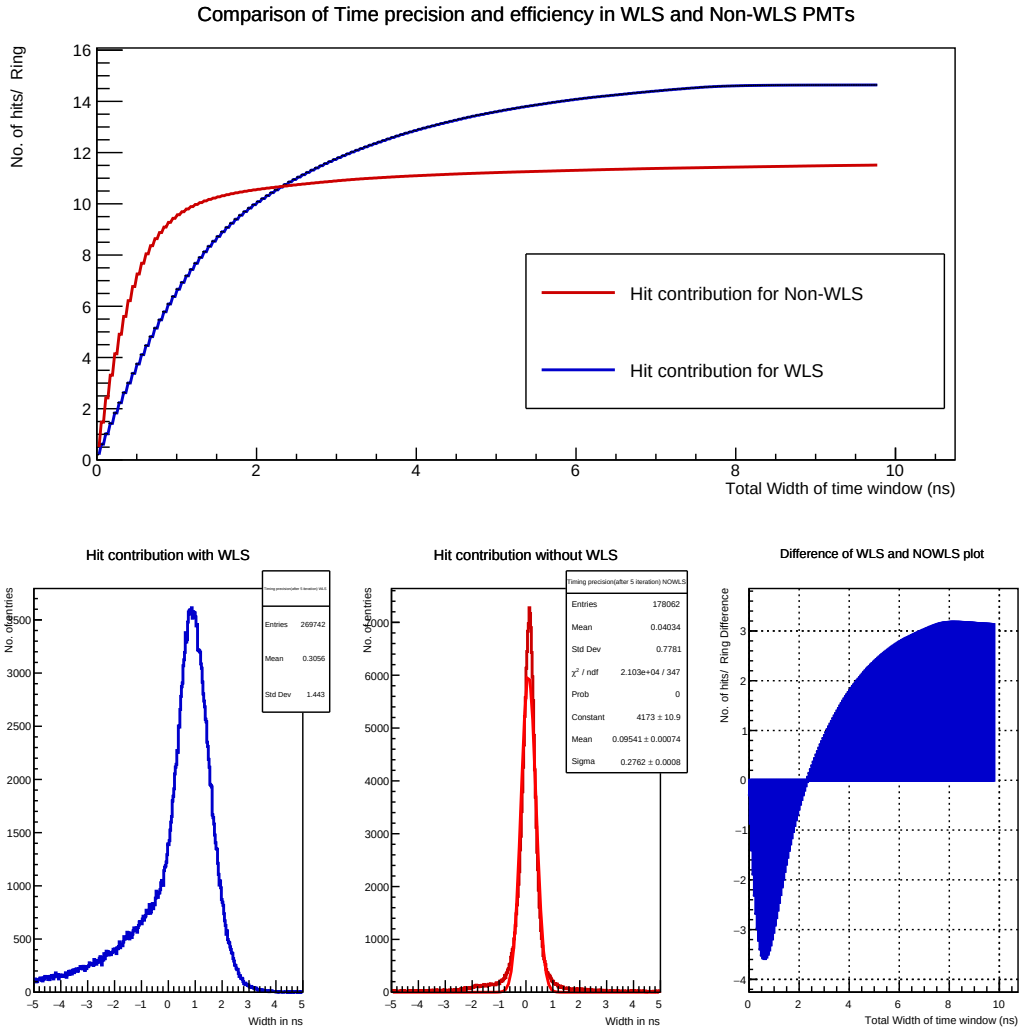

Figure 6.34: **Average Approach:** Comparison of hit contribution (top) in a given time window for WLS coated MAPMTs (bottom left blue) and non - WLS MAPMTs (bottom central red) difference plot (bottom right) . Operating threshold 70 mV.

Consequently, the differences for the delayed hits manifest as negative values, giving rise to a characteristic tail at the initial section of the curve. Moreover, these delayed hits impact the overall average timing, leading to the broadening of the timing spectrum and, consequently, a deterioration in timing precision.

Hence, while the utilization of WLS coating offers certain advantages, it necessitates the acceptance of a trade-off in the form of diminished time precision for the detector.

A quantitative assessment of the impact of utilizing WLS- MAPMTs is presented in figure 6.34. This figure facilitates a comparison between the timing correction curves obtained using the average approach for MAPMTs with and without WLS coating. Given that WLS contributes to the average (or median) timing, it is of interest to quantify its influence on both timing precision and efficiency. To conduct this comparison, timing plots for WLS-coated MAPMTs (depicted by the blue curve) and non-WLS MAPMTs (illustrated by the red curve) were meticulously scrutinized on a bin-by-bin basis. Within each bin width, the number of recorded entries were documented.

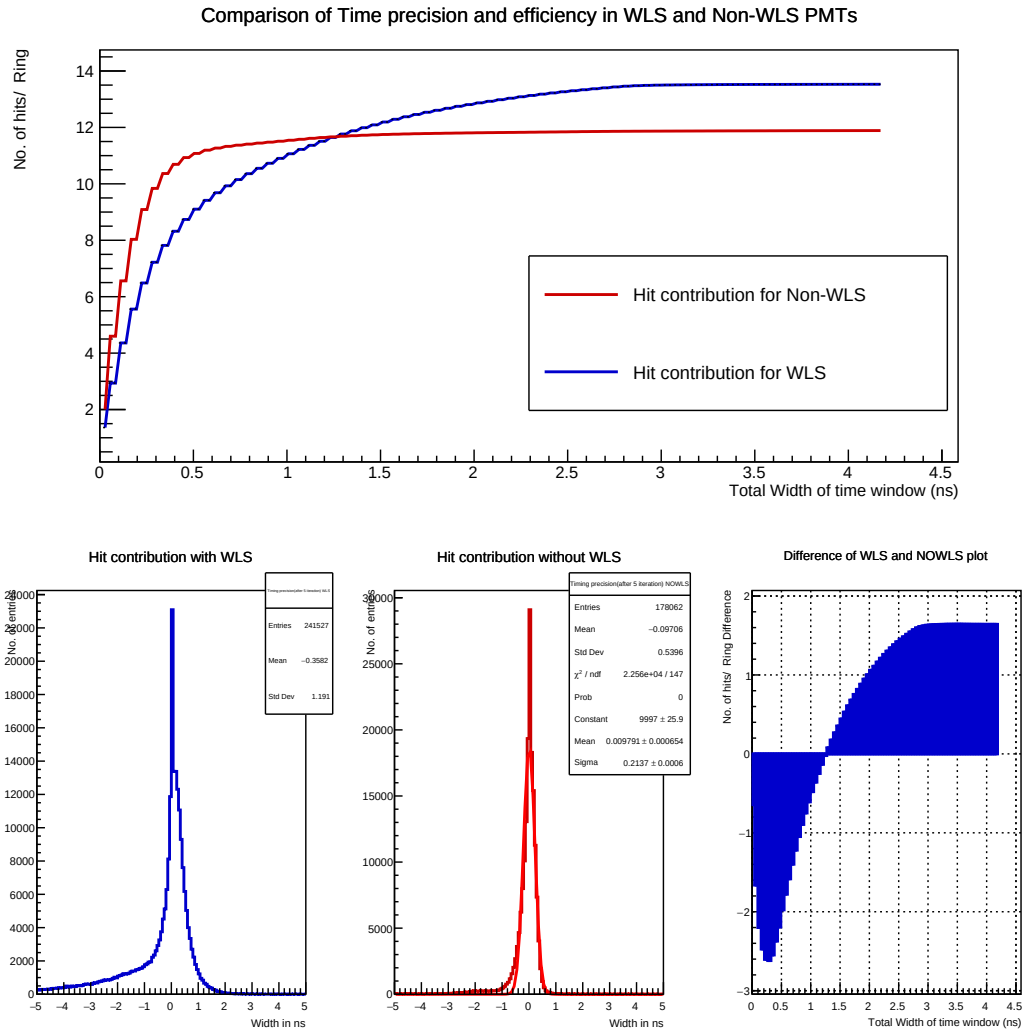

Figure 6.35: **Median Approach:** Comparison of hit contribution (top) in a given time window for WLS coated MAPMTs (bottom left blue) and non - WLS MAPMTs (bottom central red) difference plot (bottom right) . Operating threshold 70 mV.

These entries were then subjected to a division by the number of identified Cherenkov rings, leading to the computation of the event multiplicity. This analysis, as represented in figure 6.34, was executed under an operating threshold of 70 mV, providing a direct contrast between WLS and non-WLS MAPMTs.

Upon scrutinizing the blue and red plots, a conspicuous distinction emerged. For the non-WLS MAPMTs, the average Cherenkov photon hit multiplicity per Cherenkov ring attains its maximum value when time window is opened for more than 700 ps. Conversely, WLS MAPMTs necessitated a time window exceeding 3.5 ns to achieve a comparable level of efficiency per ring. To exceed the efficiency exhibited by non-WLS MAPMTs and harness the full 20% benefit, a time window of approximately 6 ns was required. However, the extension of time windows to such durations introduced additional sources of background into the data.

Figure 6.35 portrays marginal enhancements when the median is employed. Nevertheless, the overarching message remains unwavering: the integration of WLS coating engenders a discernible deterioration in timing precision. This increase in efficiency materializes at the expense of timing precision, emerging as the principal conclusion derived from this analysis."

7 Summary & Outlook

All tests required for the RICH detectors for the HADES upgrade and upcoming CBM experiments were satisfactorily completed. The performance of the readout electronics was as anticipated, and the results are encouraging. In all GSI experiments, the DiRICH readout system is a promising technology for lepton detection. These results provided an excellent opportunity to comprehend the DiRICH concept, and the lessons learned from these tests established the groundwork for further development of the DiRICH FEE board. In this chapter, a summary of this thesis and a glimpse into the future of DiRICH is discussed.

7.1 Summary

7.1.1 Quality assurance tests for MAPMTs

The Wuppertal lab provides an extraordinary facility for systematic testing of PMT-like detectors. The Quantum efficiency test setup is a reliable test setup used to mass-test Hamamatsu's claimed quantum efficiency of the MAPMTs. The tests provided an important quantitative insight into the surface profile of the photo cathode distribution. QE tests were also valuable in checking the spectral sensitivity of the MAPMTs over a range of wavelengths. These tests helped to maintain the quality control of all the MAPMTs deliveries from Hamamatsu. The tests also helped check the quality assurance of the MAPMTs used during the beam or iso-butane tests. The quantum efficiency of H12700 was measured to be 25-30% peaking at 400 nm which agrees with the specsheet provided by Hamamatsu.

7.1.2 Effect of the temperature on the dark rate

The dark rate of PMTs has a positive correlation with temperature, which is a well-known fact. In the case of H12700 MAPMTs, however, a quantitative aspect of this effect remained to be determined. Temperature dependence tests discussed in Chapter 2 provided a comprehensive understanding of this effect. The rate constant deduced from these experiments was incorporated into all dark rate calculations. Additionally, the HADES-RICH's cooling system was modified to maintain an ambient temperature below 40°C. These tests constituted one of the most important MAPMTS quality assurance tests. Using a 3D printer, special components that could be directly fixed on the DiRICH backplane were developed. As depicted in the figure 7.1, these mounts were then used to direct cool air at a single DiRICH level, preventing heat transfer from densely packed electronics traveling through the PMT-backplane to MAPMTs.

7.1.3 Effect of Wavelength Shifting coating (WLS) on the quantum efficiency of the MAPMTs

Coating the exterior window of MAPMT with a WLS coating increases its UV efficiency. Using WLS-coated MAPMTs in low photon yield regions of HADES and CBM RICH in an effort to increase the detector's efficiency and collect as many photons as feasible. As discussed in Chapter 3, the maximum quantum efficiency of MAPMTs is approximately 25% at 400 nm. There is a notable enhancement in the 200 nm region after WLS coating is applied. In WLS coated MAPMTS, the QE of the MAPMT was 10% more than those without WLS coating at 200 nm wavelength. Currently, 48 HADES RICH MPAMTS are WLS-coated MAPMTs.

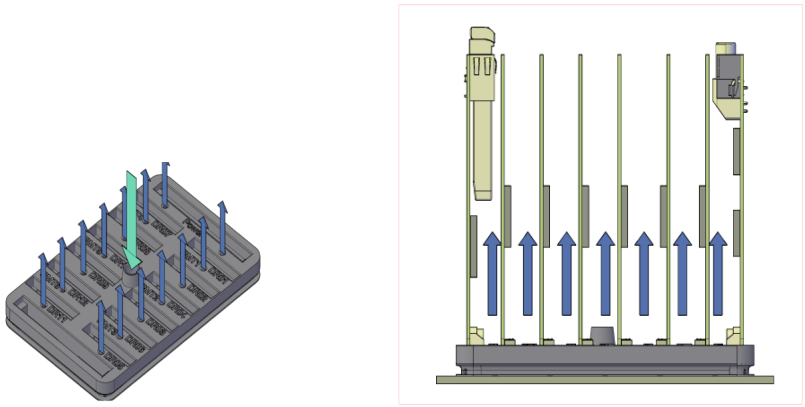

Figure 7.1: A 3D printed mask that can be directly mounted on the backplane. The arrows shows the direction of the air flow (left). The dark blue arrows shows the exiting air from the vents striping the heat with it as it flows between each DiRICH (right).

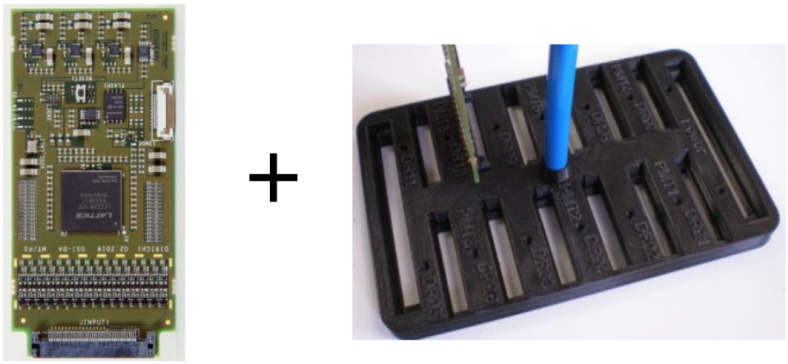

Figure 7.2: Actual photograph of the DiRICH module and a cooling mask with a sample DiRICH module and inlet pipe for the air.

7.2 DiRICH readout electronics

7.2.1 Performance of the analog amplifier of the DiRICH

The DiRICH FEE board includes two components: an analog amplifier and a TDC based on an FPGA. Efforts were made to evaluate the performance of the analog amplifier at Wuppertal and GSI. The outcomes of these tests are discussed in detail in Chapters 4 and 5, respectively. These experiments proved useful for measuring the various electronic aspects of the DiRICH readout. These evaluations yielded some of the most significant findings regarding DiRICH. One of the primary takeaways from these experiments is the crosstalk profile and its influence on the detector. To eliminate cross-talk, the Time over threshold cuts (ToT) method was implemented. These measurements revealed that DiRICH was capable of measuring timing precision with sigma as low as 270 ps (limited by PMT's TTS) which translates in to 500 ps FWHM. The primary objective of these experiments was to compare the speed of this readout to that of its Padiwa-based predecessor. Apart from that it was also found that one can easily suppress the cross-talks just using ToT cuts and can maintain almost 100% efficiency of the detector. The success of these tests made it possible to evaluate the entire readout under real beam conditions in conjunction with DAQ.

7.2.2 Beam test at COSY accelerator

Once the laboratory tests were completed, the complete test module i.e. MAPMT, DiRICH readout chain were tested in a real beam enviroment at COSY accelerator Jülich. During these tests, the timing information was collected using on-board FPGA which was now available for testing. Chapter 6 describes all the details of the these tests and summary of each is discussed as follows.

7.2.2.1 MAPMT crosstalks and ToT cuts

From the learning of the laboratory tests in the HADES - test box, it was known that one can easily suppress the cross-talks in the neighboring channels by applying ToT cuts. It was possible because DiRICH can measure the leading and trailing edge time with extreme precision and the difference of these two values give a precise value of Time over threshold. It was also known that the cross-talks has an opposite polarity and a significantly low value of time over threshold since it is an induce current in the neighboring channel due to capatitive coupling from the channel with the signal. One can easily see from figure 6.7 that the signal and the crosstalk peak are very well separated in time. Thus it was possible to extract all the signal information and eliminate noise without loosing the efficiency. However, ToT cuts become irrelevant if the detector is operated at higher threshold voltages and during tests it found to add unknown artifacts in the ToT. For an optimal performance of detector one of the two strategies can be implemented:

1) *To operate the detector at significantly higher thresholds (>70 mV).* For thresholds larger than 70 mV, the noise is suppressed and there is no need of ToT cuts. However, only large amplitude signals can be measured. In this scenario there is a risk of loosing detector efficiency as many low amplitude signal hits will be lost.

2) *To operate the detector at lower threshold (<70 mV).* Use ToT cuts to suppress the noise and the cross-talks and hence can achieve the higher efficiency of the detector. From tests it was found that the optimal compromise of efficiency and noise suppression can be achieved by operating the detector at 70 mV.

7.2.2.2 Timing precision

The photon hits were measured with the reference to a hodoscope trigger. For the data analysis during the beam test, two methods were used to calculate the time precision. The details of these methods are discussed in Chapter 6. Both methods yield great results. The overall time precision during the beam test was around 500 ps (FWHM). This is exceptional since the transit time factor for the MAPMT is 350 ps (FWHM) as per its spec-sheet. The time resolution is affected by the threshold settings and the noise in the detector. Thus, an efficient noise suppression is mandatory for better results. This also advocates the use of ToT cuts. Time resolution for the ring can be calculated as: Time resolution(FWHM) = 2.355 $\times\sigma$

The table 6.4 shows the time resolution calculated based on the method discussed above. It shows the results of timing for each threshold value. For MAPMT+DiRICH the time precision value is $\approx$ 600 ps (FWHM) which is well withing the expectation limits.

7.2.2.3 Ring Parameters

The Cherenkov ring produced in the beam test covers the entire PMT plane of 12 MAPMTS as shown in the figure 6.17. The main aspects of this ring are:

- **X-Centre:** The horizontal width of the MAPMT plane was 15 cm, and the height was 25 cm approx. Thus we expect the ring centre in a horizontal direction to be around 7.5 cm.

- **Y-Centre:** The Y-Centre of the MAPMT plane is around 12.5 cm.

- **Ring Radius:** The radius of the ring is around 6 cm as per the simulations.

- **dR of the ring:** When a ring finding algorithm finds and fits the ring, not all the hits need to fall on the fitted ring. There will be some hits which will be away from the fitted ring. The distance of these hits from the fitted ring is called the dR value of the ring. Thus, if dR is small it means that ring fitter can fit rings better. It can also be deduced that having extra hits in the form of noise can spoil the dR parameter of the ring, as shown in figure 6.17.

It was observed during the tests that ring quality was significantly improved after applying ToT cuts which proves the worth of ToT cuts in improving ring quality. ToT cuts can be crucial in case where there are multiple rings located closely to each other and a lot of stray hits from the cross-talks makes it difficult for the ring fitting algorithm to find the correct ring (Table. 6.2).

7.2.2.4 Effect of using Wavelength Shifting Coating (WLS) on MAPMTs

The application of Wavelength Shifting Coating (WLS) to the detectors has a notable impact on hit multiplicity; however, it significantly affects time resolution. As ddiscussed in section 6.9.1, a 15% gain in hit multiplicity can be achieved, but it necessitates keeping the time window open for nearly 10 ns. Prolonged time window duration introduces higher levels of electronic noise into the system, demanding additional efforts for noise suppression. Such measures may result in the exclusion of low-amplitude signals, counteracting the primary motive for employing WLS coating. Conversely, strategically incorporating WLS-coated MAPMTs into the regions of the detector characterized by low acceptance can substantially enhance efficiency by increasing photon numbers. It is however an open question at the time of this thesis about how many and which portions of CBM-RICH detector will be equipped with WLS coated MAPMTS. For instance, in the case of the HADES-RICH, WLS coating was applied to 48 MAPMTs at the center. Following an upgrade, the HADES RICH conducted its inaugural beam experiment in 2019, yielding preliminary results. However, the discussion of these results falls beyond the scope of this thesis.

7.2.2.5 Summary

The main outcomes of COSY beam-time were:

1. The MAPMTs were able to resolve the Cherenkov rings, however the photons do induce crosstalk in neighboring pixels as expected. To counter this problem, only applying ToT cuts was enough and was efficient to maintain good signal to noise ratio.

2. For ring fitting algorithm to verify rings, it was necessary to have at least four hits registered on MAPMT. During beam test, the mean hit multiplicity registered was 11 hits per ring after applying ToT cuts, well above expected value. This confirms that during actual experiment, there will be almost no data loss.

3. The readouts were able to perform the expected value of time resolution. During the tests the FWHM value of time resolution measured was in the order of 600 ps.

4. Overall, the DiRICH readout electronics is now a tested concept for its use in all the future experiments at GSI.

7.3 Outlook

The DiRICH has a foreseen future in several of the current and future GSI-FAIR experiments. At present, three experiments are planning to use DiRICH readout as the electronics for their photon sensors, of which HADES will have 28000 channels in their RICH detector. Figure 7.3 shows the upgraded HADES-RICH with all MAPMTS and readout system with cabling and cooling system. Presently it had its first run with Ag-Ag collisions and data is being studied by respective detector groups.

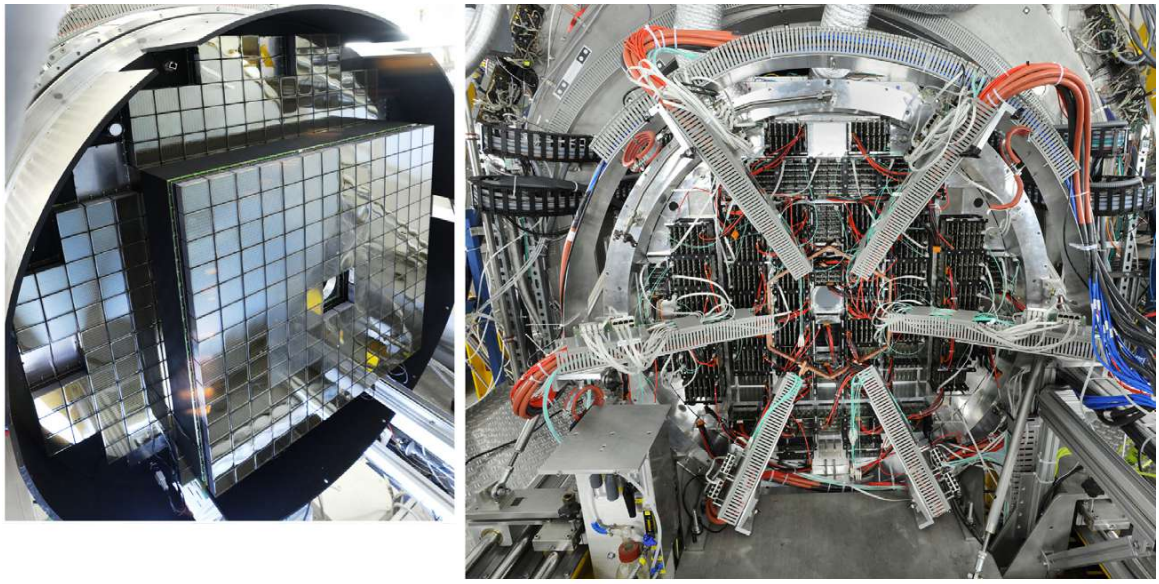

Figure 7.3: Upgraded HADES with metal shielding and installed MAPMTs (left) and the DiRICH readouts with all the cabling and the support structures for thick (orange) cables in the back (right).

The CBM will need readouts for 55000 channels of their RICH detector. The figure 7.5 shows the picture of a camera module currently in the Wuppertal laboratory.

The module is equipped with the backplanes which will hold the MAPMTs and the DiRICHs. At present, it is used to test the cooling system that will keep the temperature of the camera module below 40°C. To test this, one column of the camera module is equipped with dummy DiRICHs which when powered on, produces similar heating profile as actual DiRICHs. Two of such camera modules will be used in CBM RICH detector.

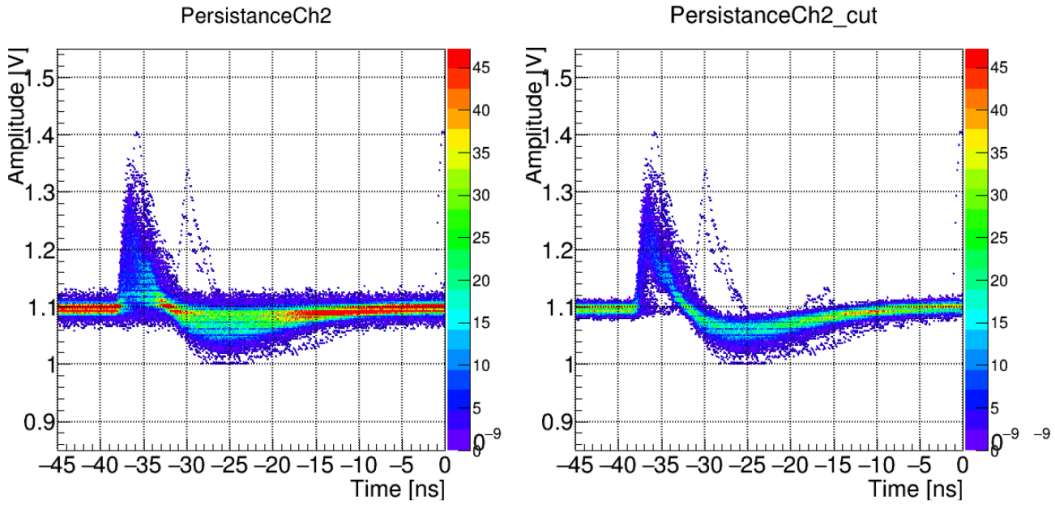

Figure 7.4: Signal from MCP showing similar characteristics like that of a MAPMT signal.

The DiRICH readout development is developed to be used for many experiments. It is a flexible concept which can be adapted for many other candidates. For example, PANDA-DIRC is considering using DiRICH as an option for their Micro-Channel plate (MCP) with a total readout of 11000 channels. To check if DiRICH can support the MCPs some tests were performed at the laboratory

in Wuppertal. Intial tests did show promising results and compatibility of DiRICH with the MCPs. Detail studies using MCP was not in the scope of this thesis

Figure 7.4 shows the signal image taken from oscilloscope showing similar signal characteristics as obtained from a MAPMT. The signal on the left is without ToT cut and hence has some noise in the center of the signal which after applying a ToT cut is removed and pure MCP response can be seen.

The research and analysis presented in this thesis were conducted during the initial iteration of the DiRICH Readout chain. Subsequently, this readout chain has undergone continuous testing and refinement to better align with the experimental requirements of GSI for various research endeavors. This thesis serves as a foundational exploration of the newly developed readout chain, striving to illuminate its significance and applicability within the context of these experiments.

Figure 7.5: The front view of the CBM camera module with all the installed backplanes to hold MAPMTs and DiRICHs (left). The rear view of the camera showing one column of DiRICHs installed to test the cooling system and the section of pipes which will use cool air from a air blower to cool the detector area. The module currently is under tests at Wuppertal.

A Tender details for MAPMTs

1. **Introduction**

   The following subchapter summarizes the tender specifications issued to potential manufacturers in the mapmt tendering process from GSI.

2. **Detailed Specification**

   (a) **Size, outer dimensions:** Outer dimensions: ~ 2×2 in^2, low size tolerance ≤ ±0.3 mm.

   (b) **Effective area:** Effective sensitive area ≥80% w.r.t. outer dimensions.

   (c) **Quantum efficiency:**
   Peak quantum efficiency at 350-400 nm ≥25% (std. BA-cathode)
   Peak quantum efficiency at 350-400 nm ≥30% (high-q.e. cathode)
   Homogeneous quantum efficiency over surface
   If quantum efficiency curve / peak quantum efficiency cannot be provided by manufacturer, then alternative measures like "Blue-Sensitivity-Index" or "luminous sensitivity" shall be used as criterion with corresponding values. The variation of the cathode uniformity should be smaller than 25% (maximum difference between 100% and relative minimum).

   (d) **Gain:** Typical gain ≥ 0.8 × 10^6 at nominal high voltage We plan to have individual HV supply for small groups of photodetectors, such that gain variations between different photodetectors can be compensated using individual HV.

   (e) **Anode uniformity:** Maximum uniformity ratio between anodes: < 1:3 Anode uniformity shall be based on the anode current per pixel for homogeneous DC illumination of the full PMT surface. It is a measure of quantum efficiency times pixel gain for individual pixels.

   (f) **ADC spectrum:** Clear single-photon peak visible in each individual pixel The manufacturer should provide ADC spectra for each pixel of each delivered tube, together with numerical evaluation in terms of average / minimum peak-valley ratio as quality criterion. If individual ADC spectra cannot be provided by the manufacturer, then we would like to measure ADC spectra in our lab upon arrival of delivered tubes, and have possibility to reject tubes not full- filling a well-defined quality criterion on peak-valley ratio.
   A minimum Peak/Valley ratio the value of 1.2 is requested for the ADC spectrum in each channel. Not more than 3 pixel per MAPMT are allowed to miss this requirements.

   (g) **Dark current:** Idark<5 nA nominal voltage.

   (h) **Dark rate:** Average dark noise at a threshold set to 20% of the single-photon amplitude: <100 Hz/pixel and < 1 kHz/single pixel. The CBM RICH detector will be read out by a fully self-triggered readout system, so a low noise performance of the sensors is important to minimize the data rate due to dark noise. Therefore the average single-photon amplitude (at 20% of the single-photon amplitude) should be <100 Hz/pixel and maximum single pixel dark rate should be < 1kHz.

   (i) **Maximum hit rate:** Guaranteed continuous operation at maximum single photon hit rate of 700 kHz/pixel This is the maximum single photon hit rate we expect according to simulations. Assuming a gain of 1.0×10^6, this corresponds to an average anode signal current of 0.10 μ A/pixel, or 7 μA for a full sensor.

   (j) **Lifetime / total accumulated anode charge:** Minimum guaranteed lifetime of >10 C/cm^2 collected anode charge Proper performance of the photo sensors without significant performance loss or failure rate after 10 C/cm^2 collected anode charge must be guaranteed.

(k) **Radiation hardness:** Sufficient transmittance of the window (80%) after accumulated dose of 200 Gy ionizing dose. To our knowledge, the front window can be considered as the most radiation-sensitive part of a sensor, it must be capable of standing above dose rates without serious loss of transmission.Therefore a drop of the transmittance of the window should be <20% up to an ionizing radiation dose of 200 Gy.

(l) **Magnetic field resistance:** Operation of the photon sensor in magnetic stray field of 20 mT without significant performance loss (2 mT if external shielding box is to be used) The photon sensors will be operated in close vicinity to a superconducting dipole magnet, causing magnetic stray fields in the region of photon sensors of 20-50 mT. Preferably, the sensors should operate under these conditions without further measures. Alternatively we consider external iron shielding to reduce stray fields in the sensor area to values <2 mT if sensors cannot operate at higher field values.Therefore the sensor should be operational without performance loss in a magnetic field of up to 2mT.

(m) **Time resolution for single photon hits:** Good time resolution below 1ns TTS (Transit Time Spread) is required in order to have possibility to separate Cherenkov photon hits belonging to overlapping events under high rate conditions.

(n) **After pulsing:** $<5\times10^{-2}$ The probability of an additional delayed signal within a time span of 2 μs after the prompt photon response should be low. Therefore the probability of after pulsing within the time window 70 ns to 1.7 μs after the main pulse should be <5%.

(o) **Matureness and experience with long term operation and reliability of detector type:** The photon sensor with these technical specifications should be a mature product of the company. There should be also sufficient confidence and experience from the operation of the detector type that the photon detectors can be operated at least 20 years. The delivery of sensors should be evenly spread over a period of not more than 2 to 3 years.

B Additional plots - Chapter 4

B.1 XY scan of faulty MAPMTs

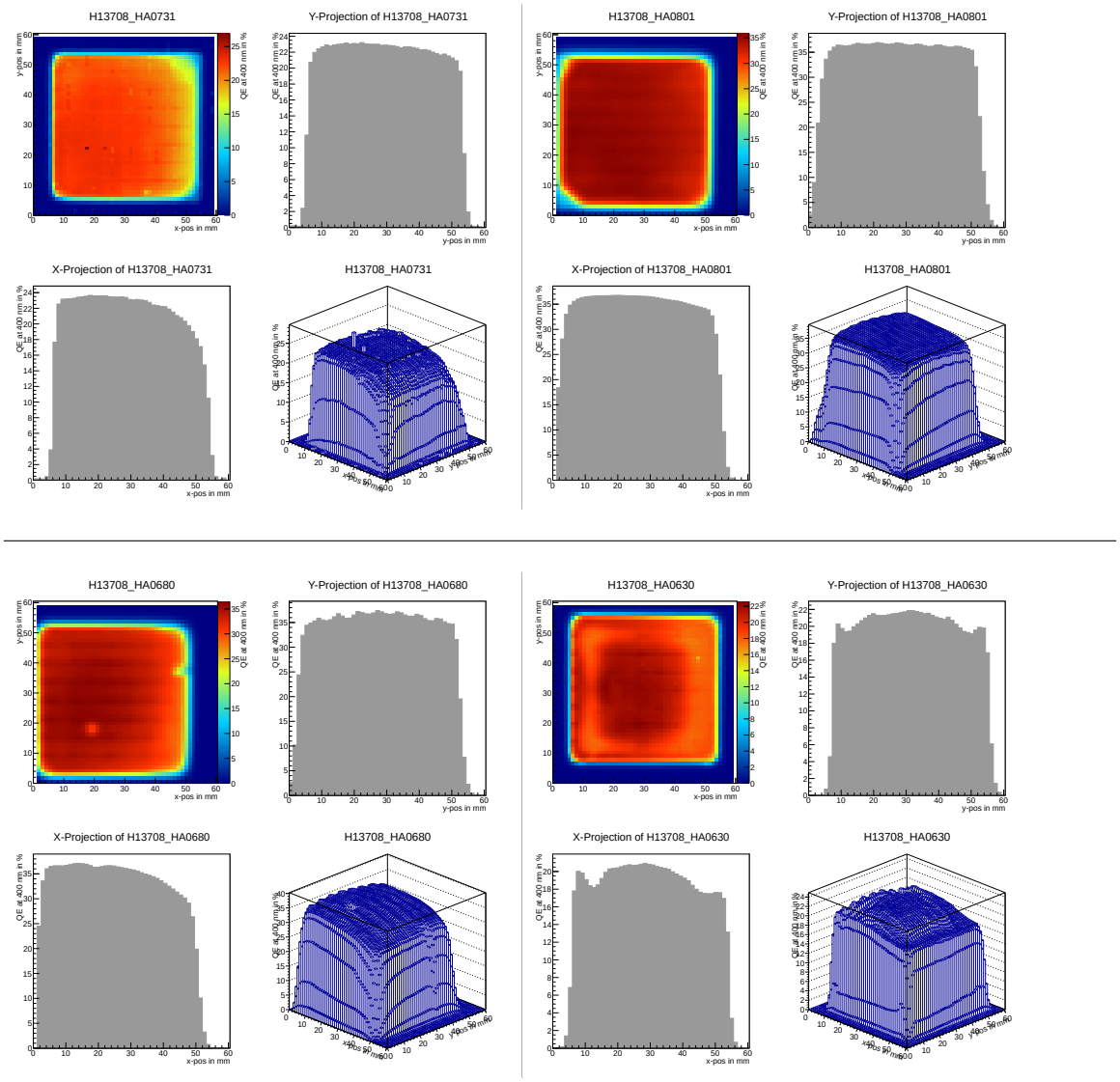

The figures show the QE plots of the faulty MAPMTs delivered during procurement process. Some of them had missing pixels in the corners, some had skewness in the distribution of QE profile, and some had damaged edges as shown in pictures above. These MAPMTs had a variety of artifacts that made them unsuitable for their use in HADES or CBM experiments; hence, they were returned to Hamamatsu and replaced subsequently.

B.2 XY scan of WLS coated MAPMTs

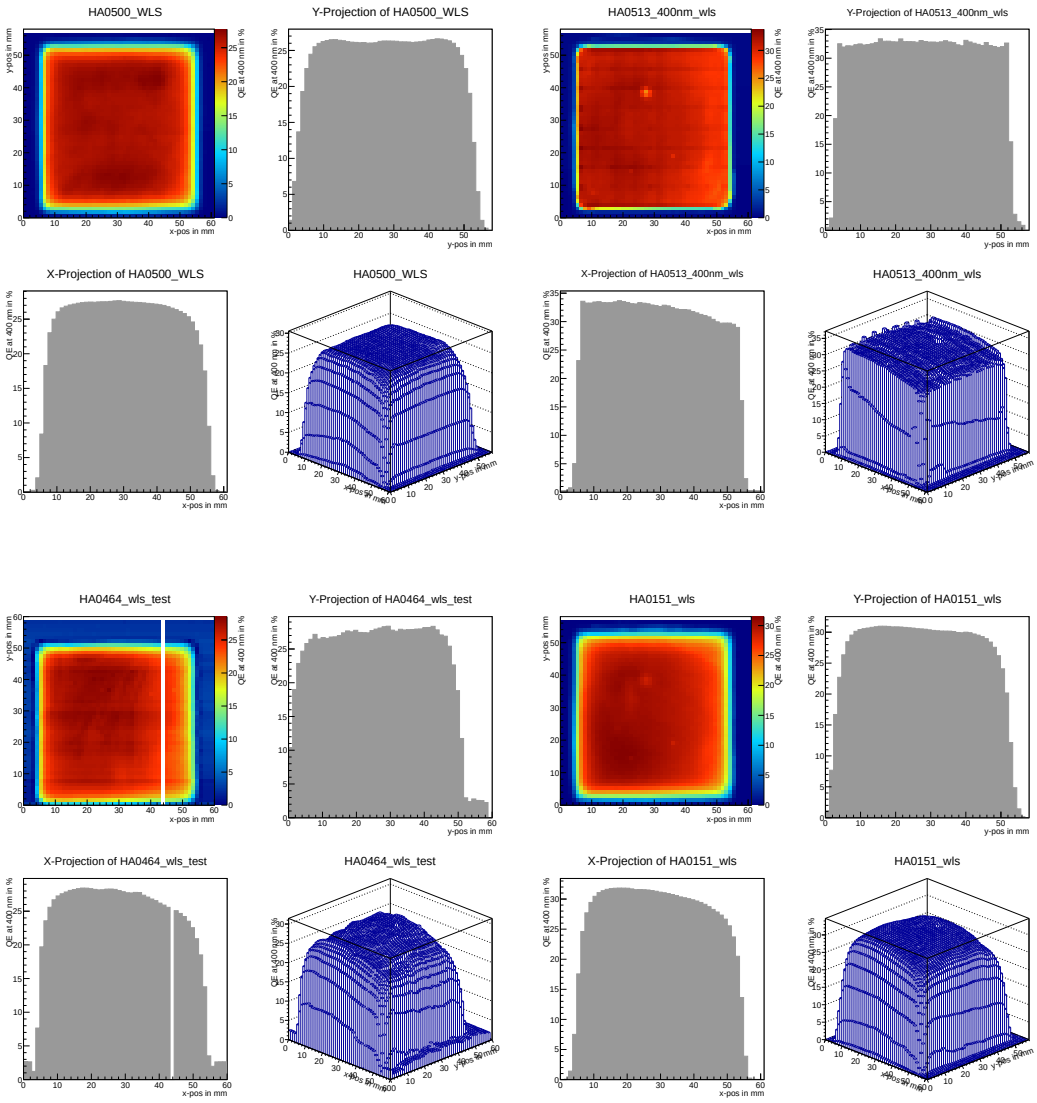

The figures show the additional QE plots of the MAPMTs delivered during procurement process which are having the QE profile within the acceptance criteria as per the tender discussed in Appendix A. The QE tests were performed during entire procurement process regularly checking random number of MAPMTs from each delivery batch making sure of quality control.

C Additional plots - Chapter 5

C.1 ToT plots

C.2 Leading edge time (Laser trigger)

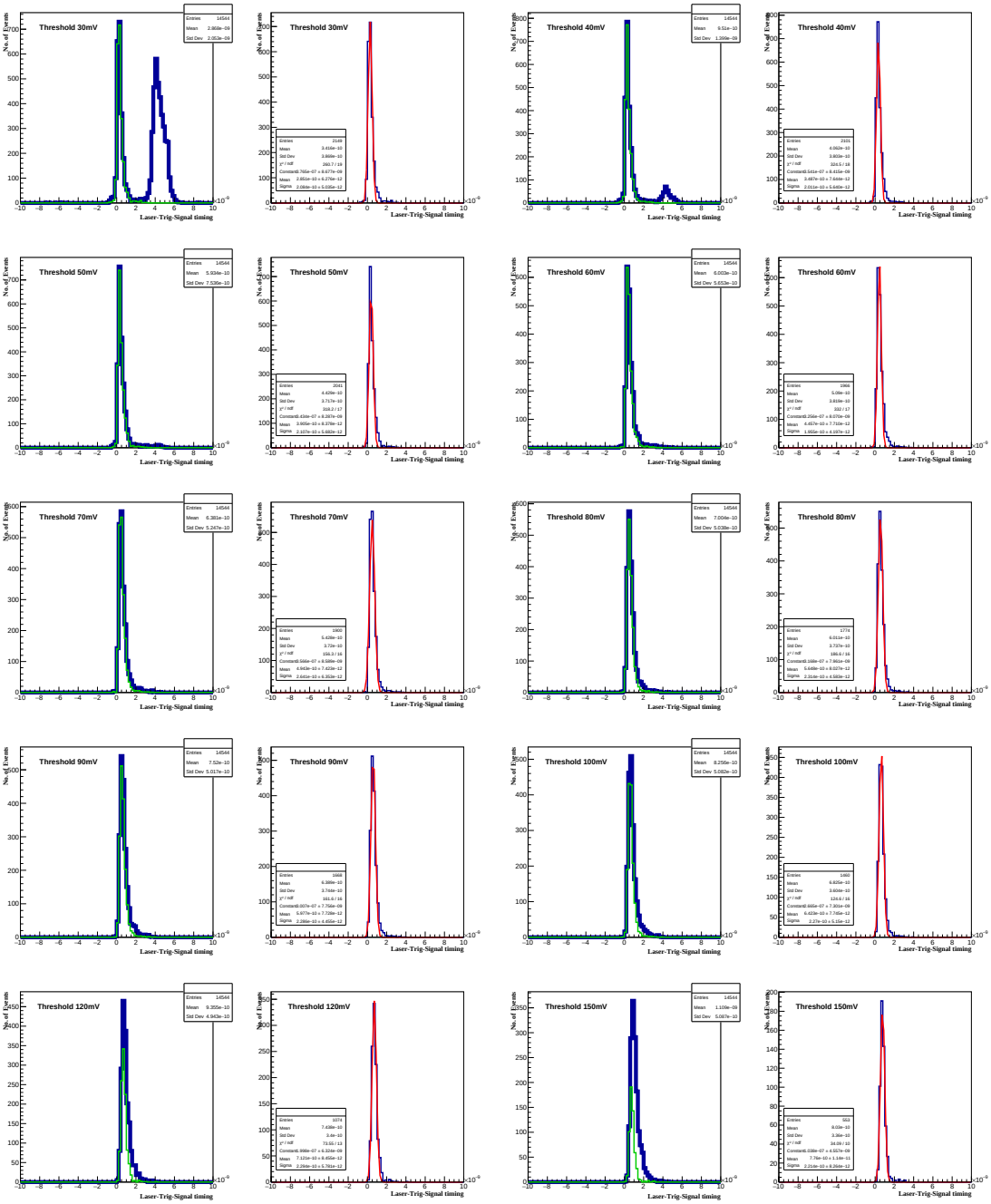

Additional plots showing the Leading edge time during HADES test box measurements. As discussed in Chapter 5, these plots represent the measurement using laser as a trigger and corre-

sponding leading edge time measured for different threshold values. These values are used in table 5.5

C.3 Leading edge time (Channel trigger)

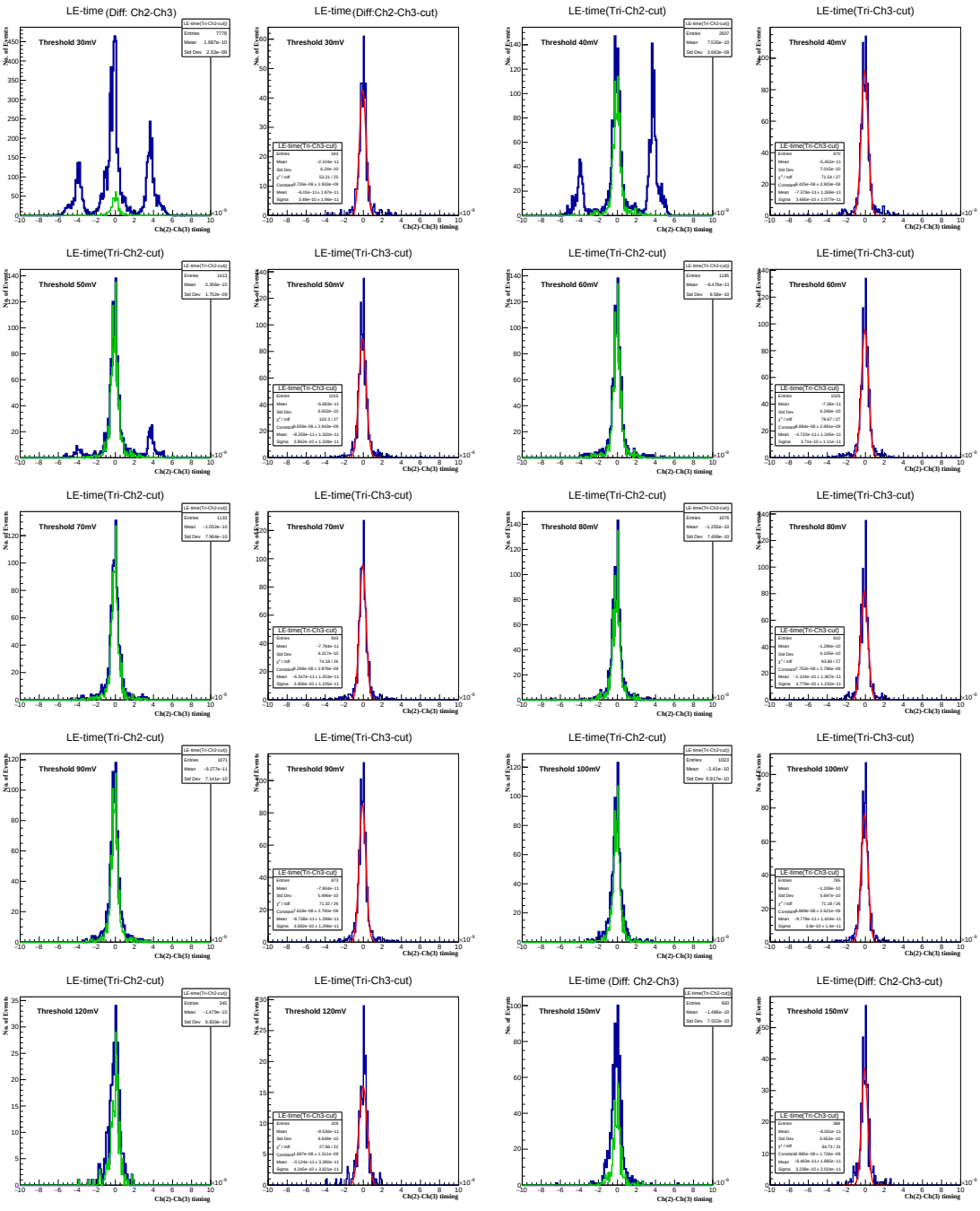

Additional plots showing the Leading edge time during HADES test box measurements. As discussed in Chapter 5, these plots represent the measurement using one channel as a trigger and measuring leading edge time in other channel for different threshold values. These values are used in table 5.2.4.2

D Additional Details - Chapter 6

D.1 COSY Beamtime setup details

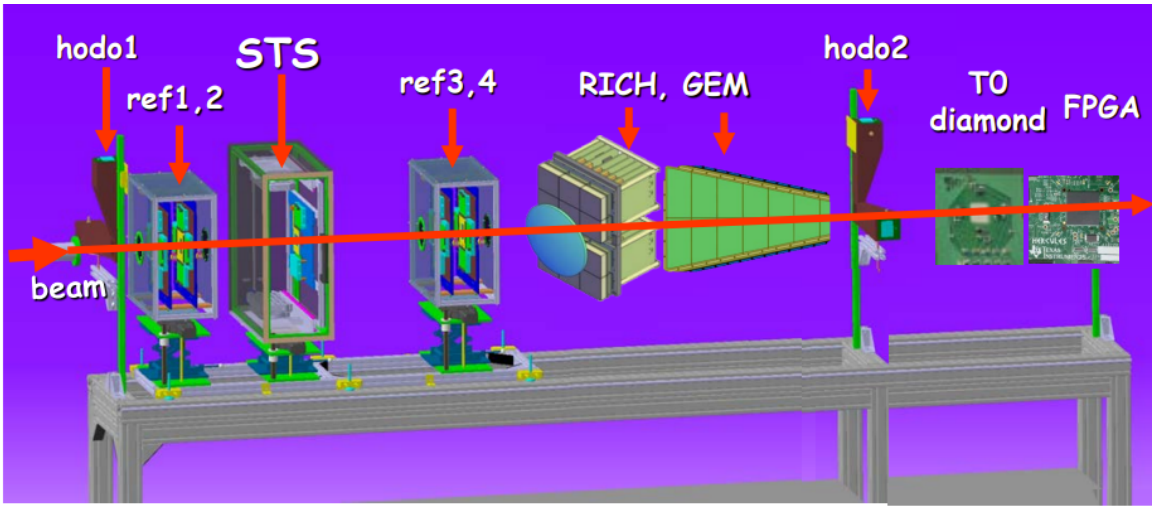

Figure D.1: COSY beamtime setup with all the experimental groups. The center line shows the beam direction passing through each detector. All the setups were mounted on a stable test bench and data taking was done remotely. The positing of the RICH detector is fourth from left following the STS setup.

The COSY beam test setup is depicted in figure D.2. RICH was situated at fourth position in forward beam direction. The beam enters the experimental setup from left as shown in figure. It first passes through Hodoscope-1 then passes through Silicon Tracking System (STS) test setup after which, enters in RICH test box. As mentioned in the setup details of COSY test box. There is a gap of 5 cm left between the MAPMTs to facilitate the beam to pass through. After passing through RICH the beam exits to second hodoscope called Hodoscope -2 and goes to other experiments.

Hodoscopes are special type of detectors which are characterized by their segmented sections. Typically the segmented sections are scintillating fibers which when exposed to radiation produces light. The light is then guided to a PMT where it is converted in to electrical signals. Further information about hodoscopes is available at [sci]&[KYS+16]. For RICH, the signal is confirmed when beam is detected in all three of detectors i.e. Hodoscope -1, RICH, Hodoscope - 2, making an AND-gate configuration as shown in figure below. Such an arrangement ensures that the signal receive at the DAQ are real signals coming from the Cherenkov radiation and not some randomly generated noise event.

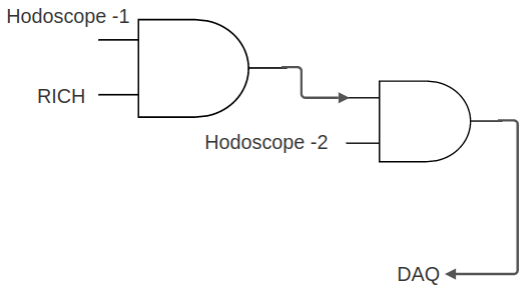

Figure D.2: Schematic diagram showing the flow of signal through COSY test box setup.

D.2 Additional plots for the Ring Parameters

D.2.1 X-Center of the Ring

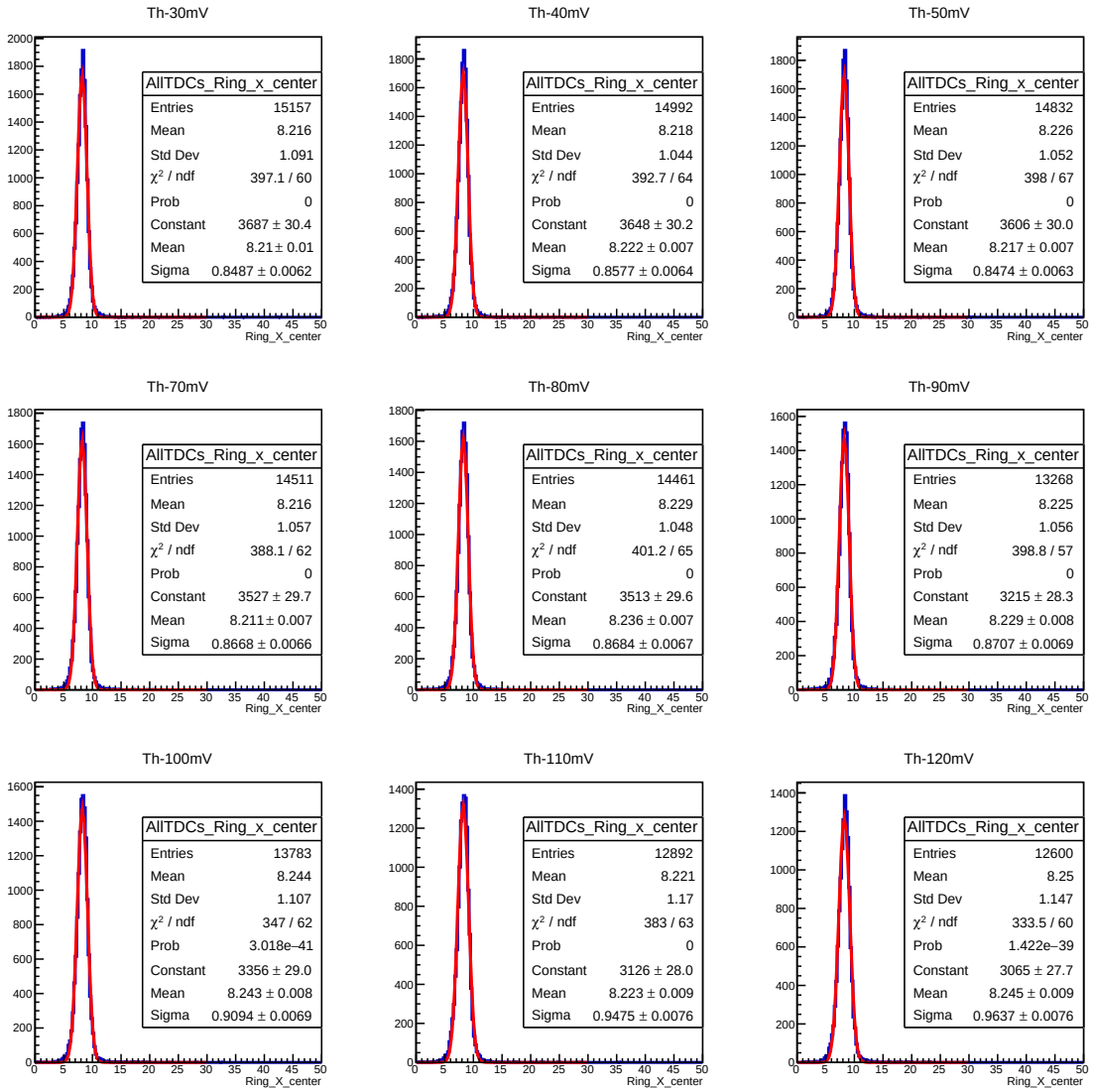

Figure D.3: X-Center of the ring after applying ToT cuts for the threshold value of 30, 40, 50,70,80, 90, 100,110 and 120 mV.

D.2.2 Y-Center of the Ring

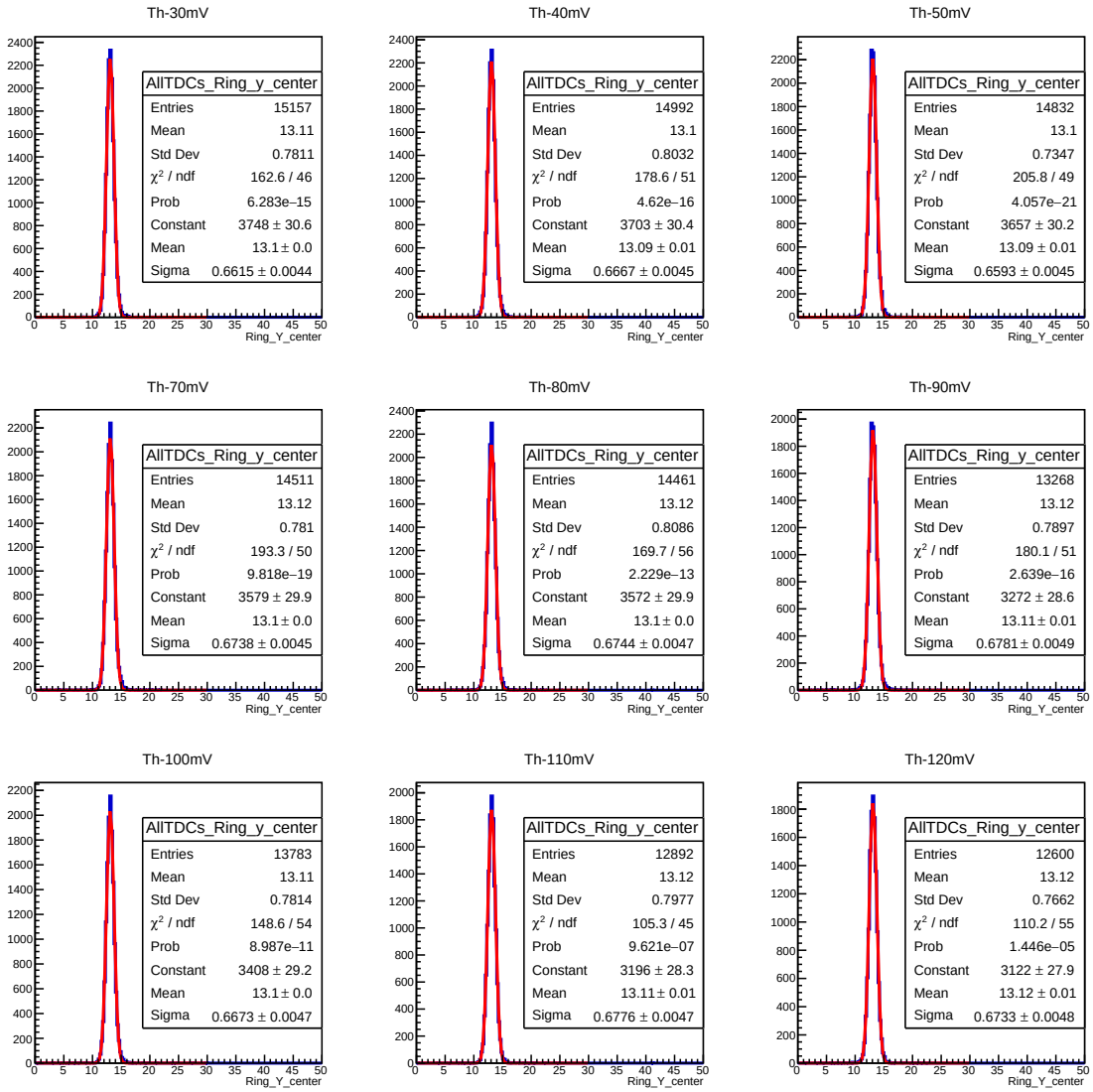

Figure D.4: Y-Center of the ring after applying ToT cuts for the threshold value of 30, 40, 50,70,80, 90, 100,110 and 120 mV.

D.2.3 Radius of the Ring

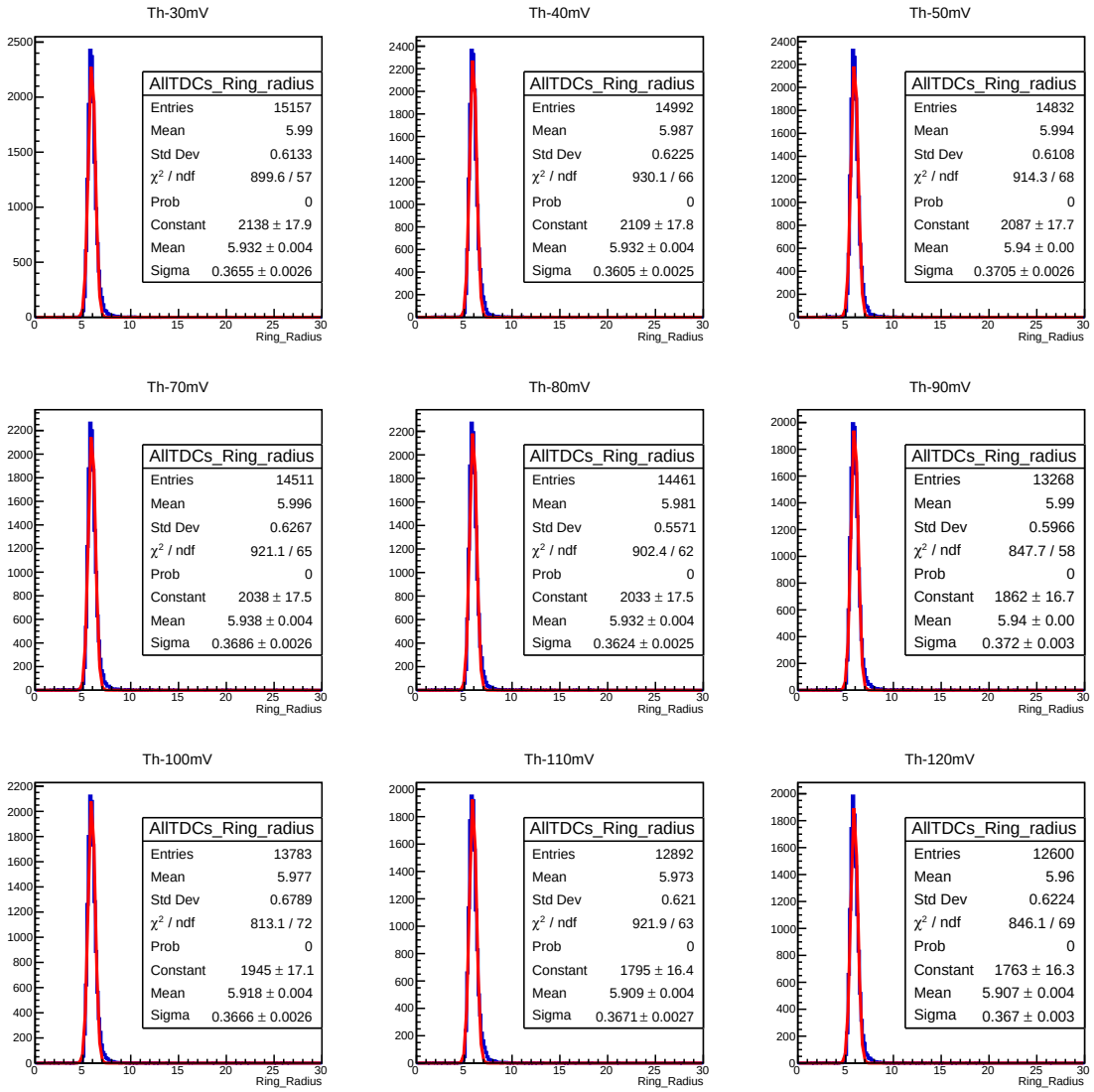

Figure D.5: Ring radius of the ring after applying ToT cuts for the threshold value of 30, 40, 50,70,80, 90, 100,110 and 120 mV.

D.2.4 dR of the Ring

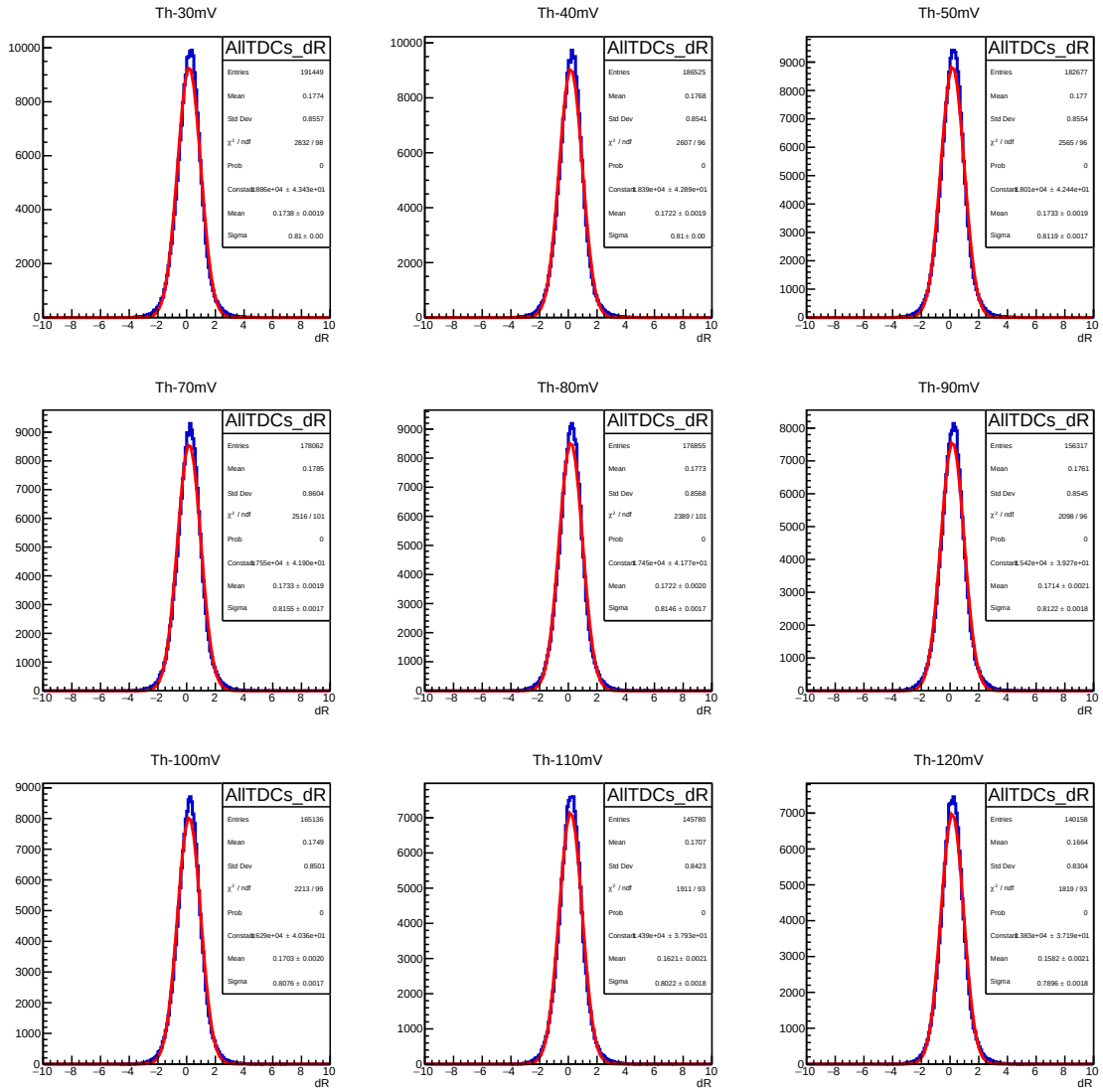

Figure D.6: dR value of the ring after applying ToT cuts for the threshold value of 30, 40, 50,70,80, 90, 100,110 and 120 mV.

D.3 Effect on Time precision due to WLS coating using Average Approach

The subsequent plots illustrate the duration required for the time window to achieve saturation in hit multiplicity. The lower set of plots provides insights into the time resolution of Multi-Anode Photomultiplier Tubes (MAPMTs) at different discrimination thresholds, with the standard deviation serving as a measure of time resolution. The final plot highlights the disparities between the time resolution plots. The positive segment of the plot signifies an increase in hit count as the time window is extended by a specific duration. Prior to this point, the utilization of Wavelength Shifting Coating (WLS) on a MAPMT offers no discernible advantages. Furthermore, his continuous support and guidance were indispensable throughout the course of this thesis.

The following plots show the contribution of WLS coating on Time precision of MAPMT. Top plot shows the time for which data should be taken for both WLS coated MAPMTs (blue curve) and the MAPMTs with no WLS coating. The bottom plots show the time resolution plots both for WLS MAPMTs (blue curve) , Non WLS MAPMTs (red curve) and the difference of these two plots showing precisely when the number of entries in WLS MAPMTs outperform Non WLS MAPMTs (shown as positive gain in photons.

D.3.1 Effect of WLS on Time Precision using Average Approach

Effect of WLS on time resolution for the MAPMT measured at the threshold of 30, 80,100 and 120 mV. Detail explanation of these plots is discussed in figure 6.34.

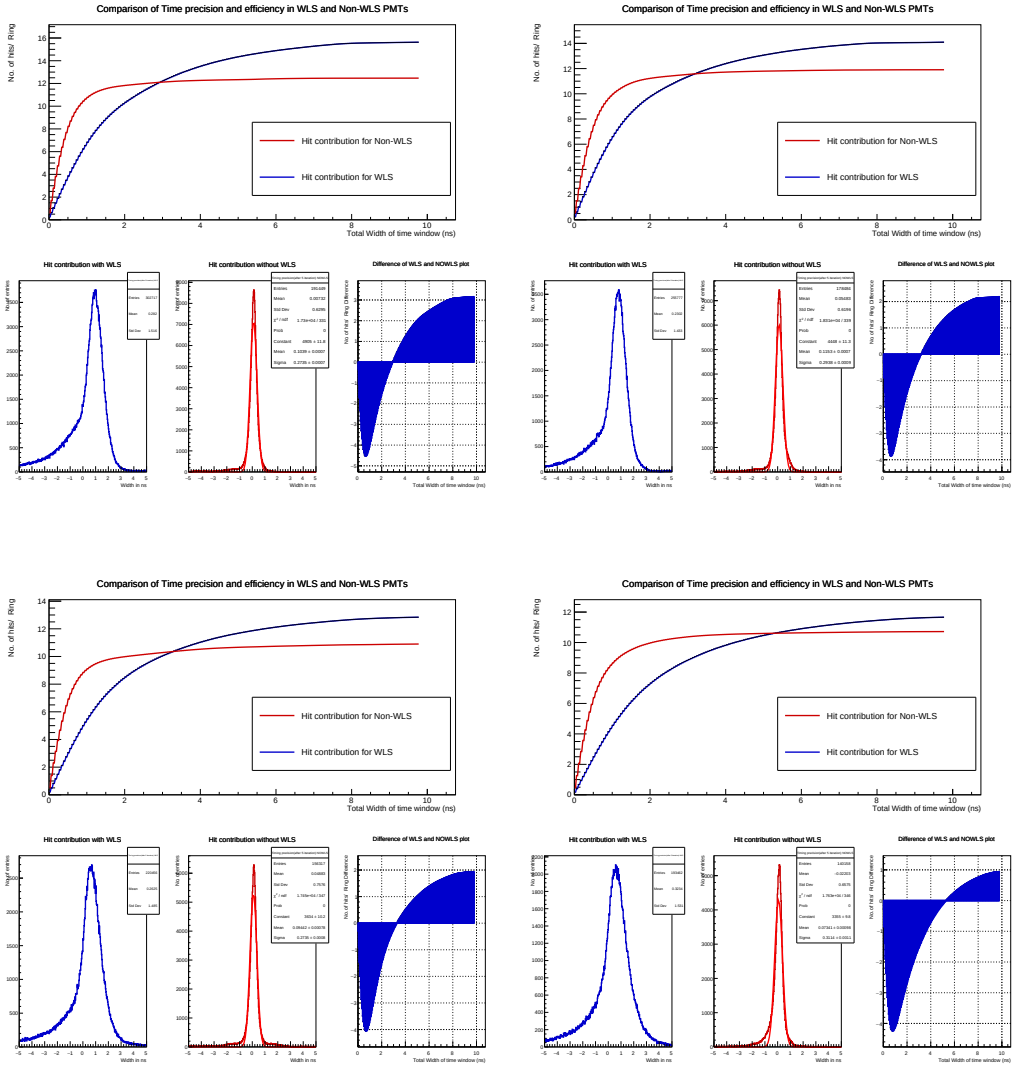

D.4 Effect on Time precision due to WLS coating using median approach

Effect of WLS on time resolution for the MAPMT measured at the threshold of 30, 60, 90 and 120 mV. Detail explanation of these plots is discussed in figure 6.35.

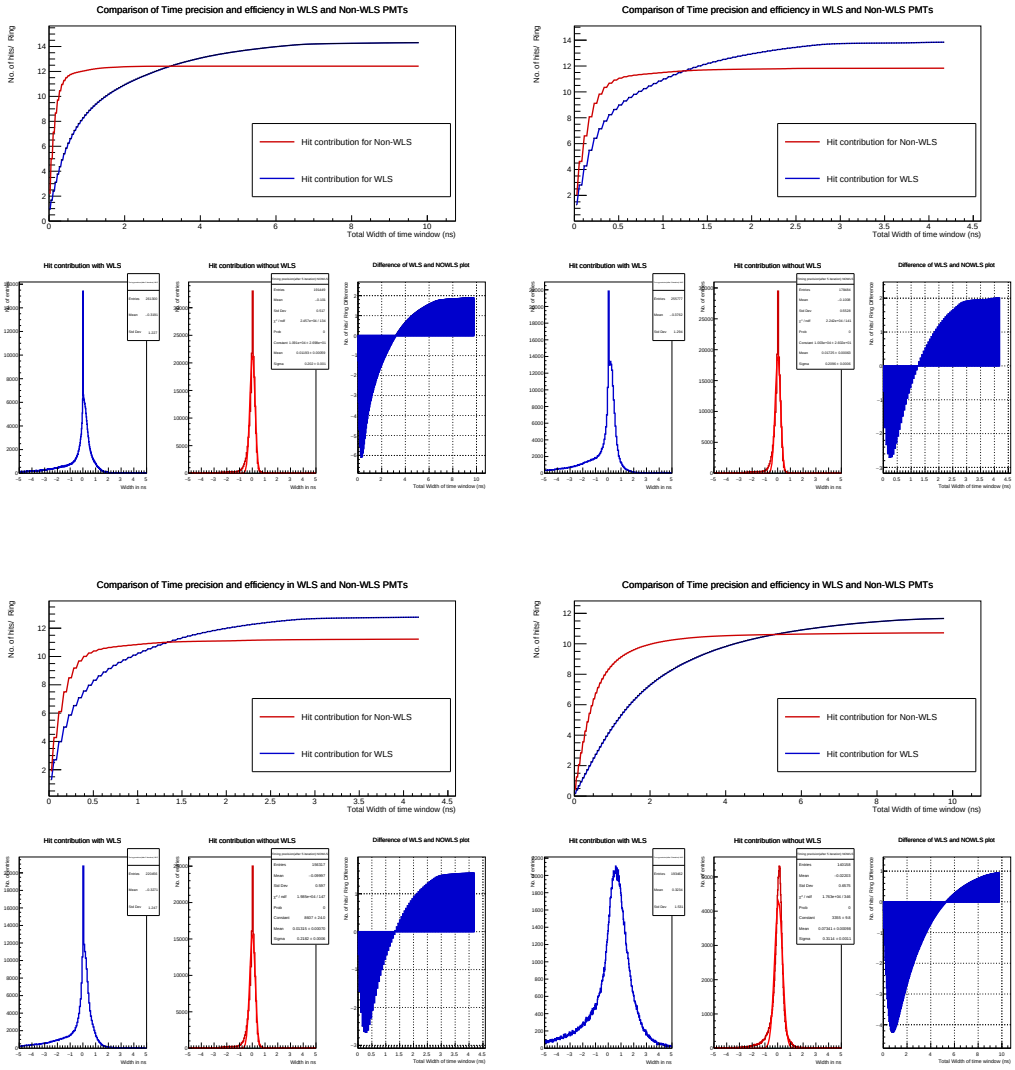

References

[AATB+05] J Adamczewski, M Al-Turany, D Bertini, HG Essel, and S Linev. The go4 analysis framework reference manual v2. 10. 2005.

[ABB+14] G Agakishiev, A Balanda, D Belver, A Belyaev, JC Berger-Chen, A Blanco, M Böhmer, JL Boyard, P Cabanelas, S Chernenko, et al. Searching a dark photon with hades. *Physics Letters B*, 731:265–271, 2014.

[AMAB+19] J Adamczewski-Musch, O Arnold, C Behnke, A Belounnas, A Belyaev, JC Berger-Chen, Jacek Biernat, A Blanco, C Blume, M Böhmer, et al. Probing dense baryon-rich matter with virtual photons. *Nature Physics*, 15(10):1040–1045, 2019.

[AMAB+20] J Adamczewski-Musch, P Akishin, J Bendarouach, C Deveaux, M Dürr, J Eschke, M Faul, J Förtsch, J Friese, J Heep, et al. Status of the cbm and hades rich projects at fair. *Nuclear Instruments and Methods in Physics Research Section A: Accelerators, Spectrometers, Detectors and Associated Equipment*, 952:161970, 2020.

[APP22] APPA research. https://www.gsi.de/work/forschung/appamml, 2022.

[BBC+09] D Belver, A Blanco, P Cabanelas, N Carolino, E Castro, J Diaz, P Fonte, JA Garzón, D Gonzalez-Diaz, A Gil, et al. The hades rpc inner tof wall. *Nuclear Instruments and Methods in Physics Research Section A: Accelerators, Spectrometers, Detectors and Associated Equipment*, 602(3):687–690, 2009.

[BBD+23] M Becker, M Beyer, M Dürr, C Feier-Riesen, J Förtsch, T Gessler, R Haas, C Höhne, K-H Kampert, S Lebedev, et al. Qualification of dirich readout chain. *Nuclear Instruments and Methods in Physics Research Section A: Accelerators, Spectrometers, Detectors and Associated Equipment*, 1056:168570, 2023.

[BHM98] Wolfgang Bauer, Kevin Haglin, and Joelle Murray. Di-leptons at cern. https://link.springer.com/chapter/10.1007/978-1-4757-9089-4_3, Jan 1998.

[cAA+09] HADES collaboration, G Agakichiev, C Agodi, H Alvarez-Pol, E Atkin, E Badura, A Balanda, A Bassi, R Bassini, G Bellia, et al. The high-acceptance dielectron spectrometer hades. *The European Physical Journal A*, 41:243–277, 2009.

[CB99] Wolfgang Cassing and Elena Leontievna Bratkovskaya. Hadronic and electromagnetic probes of hot and dense nuclear matter. *Physics Reports*, 308(2-3):65–233, 1999.

[COS] Cooler synchrotron (COSY), jülich, germany. https://www.fz-juelich.de/en/ikp/research/accelerators/cosy.

[ECP] Lattice lfe5um-85f-8bg381c fpga. https://www.mouser.de/ProductDetail/Lattice/LFE5UM-85F-8BG381C?qs=S1t%252B5bt1ScQAaUQKs0yW5g%3D%3D.

[EL79] G Eigen and E Lorenz. A method of coating photomultipliers with wavelength shifters. *Nucl. Instrum. Methods*, 166(CERN-EP-79-17):165–168, 1979.

[enc] Quark-Gluon Plasma — Encyclopedia.com — encyclopedia.com. https://www.encyclopedia.com/science/encyclopedias-almanacs-transcripts-and-maps/quark-gluon-plasma. [Accessed 25-07-2023].

[FAI] Research at FAIR — fair-center.eu. https://fair-center.eu/overview/research.

[FBV+17] Egbert Fischer, Alexander Bleile, Jorge Ceballos Velasco, Vladimir Datskov, Florian Kaether, Jan Patrick Meier, Anna Mierau, Hans Mueller, Christian Roux, Peter J Spiller, et al. Superconducting magnets at fair. In *Proc. 8th Int. Particle Accelerator Conf.(IPAC'17)*, pages 2546–2549, 2017.

[FC+99] J Friese, Hades Collaboration, et al. Studying in-medium hadron properties with hades. *Progress in Particle and Nuclear Physics*, 42:235–245, 1999.

[FSS+08] I Fröhlich, C Schrader, H Stroeble, J Stroth, A Tarantrola, M Kajetanowicz, K Korcyl, W Krzemień, M Palka, P Salabura, et al. Trb for hades and fair experiments at gsi. In *Astroparticle, Particle And Space Physics, Detectors And Medical Physics Applications*, pages 973–977. World Scientific, 2008.

[GSI] Proposals for experiments at SIS18 during FAIR Phase-0 - GSI Repository — repository.gsi.de. https://repository.gsi.de/record/220071/files/.

[Gyu04] Miklos Gyulassy. The qgp discovered at rhic. In *Structure and dynamics of elementary matter*, pages 159–182. Springer, 2004.

[HC+21] Szymon Harabasz, Hades Collaboration, et al. Characterizing baryon dominated matter with hades measurements. *Nuclear Physics A*, 1005:121886, 2021.

[Hor17] Stephen Horvat. Exploring the nuclear phase diagram with beam energy scans. In *Journal of Physics: Conference Series*, volume 832, page 012039. IOP Publishing, 2017.

[Kop14] Jan Kopfer. Development of a prototype camera and Monte Carlo studies for the optimisation of the CBM-RICH detector / vorgelegt von Jan Martin Kopfer — elekpub.bib.uni-wuppertal.de. https://elekpub.bib.uni-wuppertal.de/urn/urn:nbn:de:hbz:468-20140515-122625-5, 2014.

[KSTO85] H Kume, S Suzuki, Junichi Takeuchi, and Koichiro Oba. Newly developed photomultiplier tubes with position sensitivity capability. *IEEE Transactions on Nuclear Science*, 32(1):448–452, 1985.

[KYS+16] VKS Kashyap, C Yadav, ST Sehgal, R Sehgal, RG Thomas, LM Pant, and AK Mohanty. Plastic scintillator-based hodoscope for the characterization of large-area resistive plate chambers. *Pramana*, 87:1–7, 2016.

[lbl] Phases of Nuclear Matter — www2.lbl.gov. https://www2.lbl.gov/abc/wallchart/chapters/09/0.html. [Accessed 25-07-2023].

[LFKH17] Semen Lebedev, Juergen Friese, Tobias Kunz, and Claudia Hoehne. Simulation results for the upgraded rich detector in the hades experiment. *Verhandlungen der Deutschen Physikalischen Gesellschaft*, 2017.

[LHO+10] Semeon Lebedev, Claudia Hoehne, Gennady Ososkov, forthe Cbm Collaboration, et al. Ring recognition and electron identification in the rich detector of the cbm experiment at fair. In *Journal of Physics: Conference Series*, volume 219, page 032015. IOP Publishing, 2010.

[Mag] Superconducting magnet for HADES. https://hades.gsi.de/?q=node%2F17.

[Mai97] Rudolf Maier. Cooler synchrotron cosy. *Nuclear Physics News*, 7(4):5–13, 1997.

[MC+99] C Müntz, Hades Collaboration, et al. The di-electron spectrometer HADES at gsi: a status report. *Nuclear Physics B-Proceedings Supplements*, 78(1-3):139–144, 1999.

[MCH+12] RA Montgomery, EN Cowie, M Hoek, T Keri, and B Seitz. Multianode photomultiplier tube studies for imaging applications. *Nuclear Instruments and Methods in Physics Research Section A: Accelerators, Spectrometers, Detectors and Associated Equipment*, 695:326–329, 2012.

[MFF+17] J Michel, M Faul, J Friese, C Höhne, K-H Kampert, V Patel, C Pauly, D Pfeifer, P Skott, M Traxler, et al. Electronics for the rich detectors of the hades and cbm experiments. *Journal of Instrumentation*, 12(01):C01072, 2017.

[Muh03] F Muheim. Multianode photo multiplier tubes as photo detectors for ring imaging cherenkov detectors. *Nuclear Instruments and Methods in Physics Research Section A: Accelerators, Spectrometers, Detectors and Associated Equipment*, 502(1):52–56, 2003.

[Mün07] Christian Müntz. Dilepton measurements with hades. *arXiv preprint arXiv:0710.3274*, 2007.

[NAMH+13] Andreas Neiser, Jörn Adamczewski-Musch, Matthias Hoek, Wolfgang Koenig, Grzegorz Korcyl, Sergey Linev, Ludwig Maier, Jan Michel, Marek Palka, Manuel Penschuck, et al. Trb3: a 264 channel high precision tdc platform and its applications. *Journal of Instrumentation*, 8(12):C12043, 2013.

[NHIM10] Kimitsugu Nakamura, Yasumasa Hamana, Yoshihiro Ishigami, and Toshikazu Matsui. Latest bialkali photocathode with ultra high sensitivity. *Nuclear Instruments and Methods in Physics Research Section A: Accelerators, Spectrometers, Detectors and Associated Equipment*, 623(1):276–278, 2010.

[NUS22] Nustar. https://www.gsi.de/work/forschung/nustarenna, 2022.

[PAN23] The panda experiment at fair. https://panda.gsi.de/, 2023.

[PEF+17] C Pauly, J Eschke, M Faul, J Friese, C Höhne, K-H Kampert, T Kunz, S Lebedev, J Michel, W Niebur, et al. Upgrade of the hades rich photon detector with h12700 mapmts. *Nuclear Instruments and Methods in Physics Research Section A: Accelerators, Spectrometers, Detectors and Associated Equipment*, 876:164–167, 2017.

[PMT] https://www.hamamatsu.com/content/dam/hamamatsu-photonics/sites/documents/99_SALES_LIBRARY/etd/PMT_handbook_v4E.pdf.

[Pol13] Sergey V Polyakov. Photomultiplier tubes. In *Experimental methods in the physical Sciences*, volume 45, pages 69–82. Elsevier, 2013.

[PT18] V. Patel and M. Traxler. The hades-rich upgrade using hamamatsu h12700 mapmts with dirich fee + readout. *Journal of Instrumentation*, 13(03):C03038, mar 2018.

[Ram09] B Ramstein. Study of elementary reactions with the hades dielectron spectrometer. *arXiv preprint arXiv:0912.2677*, 2009.

[RB14] Johann Rafelski and Jeremiah Birrell. Traveling through the universe: Back in time to the quark-gluon plasma era. In *Journal of Physics: Conference Series*, volume 509, page 012014. IOP Publishing, 2014.

[Rei16] Sascha Reinecke. Characterisation of photon sensors for the CBM-RICH and its use for the reconstruction of neutral mesons via conversion - GSI Repository — repository.gsi.de. https://repository.gsi.de/record/206473/export/he?ln=en, 2016.

[RW00] R Rapp and J IIEur Wambach. Phys. ja 1999. v. 6. *Adv. Nucl. Phys*, 25:1, 2000.

[SAA+04] P Salabura, G Agakichiev, C Agodi, H Alvarez-Pol, A Balanda, G Bellia, D Belver, J Bielcik, M Böhmer, H Bokemeyer, et al. Study of e+, e- production in elementary and nuclear collisions near the production threshold with hades. *Progress in Particle and Nuclear Physics*, 53(1):49–58, 2004.

[SAB+18] J Schwiening, A Ali, A Belias, R Dzhygadlo, A Gerhardt, K Götzen, G Kalicy, M Krebs, D Lehmann, F Nerling, et al. The panda barrel dirc. *Journal of Instrumentation*, 13(03):C03004, 2018.

[SBB+20] P Spiller, R Balss, P Bartolome, J Blaurock, U Blell, O Boine-Frankenheim, L Bozyk, M Chorowski, T Eisel, M Frey, et al. The fair heavy ion synchrotron sis100. *Journal of Instrumentation*, 15(12):T12013, 2020.

[SBC+14] O Svoboda, C Blume, W Czyżycki, E Epple, L Fabbietti, T Galatyuk, M Golubeva, F Guber, S Hlaváč, A Ivashkin, et al. Electromagnetic calorimeter for the hades@ fair experiment. *Journal of Instrumentation*, 9(05):C05002, 2014.

[SBG+96] R Schicker, A Brenschede, K Garrow, H Schön, A Balanda, H Bokemeyer, J Friese, W Karig, P Kienle, W Koenig, et al. Acceptance and resolution simulation studies for the dielectron spectrometer hades at gsi. *Nuclear Instruments and Methods in Physics Research Section A: Accelerators, Spectrometers, Detectors and Associated Equipment*, 380(3):586–596, 1996.

[sci] Peter Reid scifun@ed.ac.uk. Hodoscops. http://www.scifun.ed.ac.uk/pages/pp4ss/pp4ss-hodoscope.html.

[Sen20] Peter Senger. Astrophysics in the laboratory—the cbm experiment at fair. *Particles*, 3(2):320–335, 2020.

[Sin13] Bikash Sinha. The mini bang and the big bang: From collider to cosmology. In *Exciting Interdisciplinary Physics: Quarks and Gluons/Atomic Nuclei/Relativity and Cosmology/Biological Systems*, pages 261–273. Springer, 2013.

[SN09] Motohiro Suyama and Kimitsugu Nakamura. Recent progress of photocathodes for pmts. In *Proceedings of the International Workshop on New Photon Detectors, Japan*, 2009.

[Sta] Start detector for hades. https://hades.gsi.de/node/32.

[T+14] M Traxler et al. Applications of the trb3 and associated front end electronics in recent beam times. *Scientific Report 2014*, 2015:1, 2014.

[TFK+08] Attilio Tarantola, I Frohlich, BW Kolb, J Michel, C Muntz, M Palka, H Strobele, J Stroth, M Traxler, and J Wustenfeld. The upgrade of the multiwire drift chamber readout of the hades experiment at gsi. In *2008 IEEE Nuclear Science Symposium Conference Record*, pages 2146–2149. IEEE, 2008.

[Web18] Adrian Amatus Weber. Time resolution of the dirich mapmt readout with and without wls coverage. *Verhandlungen der Deutschen Physikalischen Gesellschaft*, 2018.

[Web21] Adrian Amatus Weber. Development of readout electronics for the rich detector in the hades and cbm experiments-hades rich upgrade, mrich detector construction and analysis. Technical report, HADES, 2021.

[Wik23] Wikipedia contributors. Timeline of particle physics — Wikipedia, the free encyclopedia. https://en.wikipedia.org/w/index.php?title=Timeline_of_particle_physics&oldid=1165586609, 2023. [Online; accessed 24-July-2023].

[YBB+90] A Yegneswaran, S Beedoe, J Bystricky, J Carroll, S Christo, G Claesson, P Force, R Fulton, JF Gilot, J Gordon, et al. The dilepton spectrometer. *Nuclear Instruments and Methods in Physics Research Section A: Accelerators, Spectrometers, Detectors and Associated Equipment*, 290(1):61–75, 1990.

[ZEF+99] Karl Zeitelhack, A Elhardt, J Friese, R Gernhäuser, J Homolka, A Kastenmüller, P Kienle, H-J Körner, P Maier-Komor, M Münch, et al. The hades rich detector. *Nuclear Instruments and Methods in Physics Research Section A: Accelerators, Spectrometers, Detectors and Associated Equipment*, 433(1-2):201–206, 1999.

Acknowledgments

A doctoral dissertation is a lengthy and often challenging endeavor with many highs and lows. Throughout this demanding path, there were countless individuals whose unwavering support, motivation, and guidance played a pivotal role in helping me reach my fullest potential. It is with deep gratitude that I dedicate this thesis to these exceptional people, as it is a testament to the collective efforts that have contributed to its creation. Infact, this thesis represents the "superposition of efforts" of those who assisted me throughout my journey.

I owe an immense debt of gratitude to Professor Karl-Heinz Kampert for providing me with the opportunity to work within the esteemed RICH group at Bergische Universität Wuppertal. His mentorship, both professionally and personally, has been instrumental in shaping my growth as a researcher. Furthermore, his continuous support and guidance were indispensable throughout the course of this thesis.

I am profoundly indebted to Christian Pauly, whose encouragement, training, and unwavering assistance were instrumental in bringing this PhD journey to fruition. His meticulous proofreading of my thesis and motivation during its most challenging phases were invaluable. My heartfelt gratitude goes to Joerg Fortsch, who consistently stood by me, providing support and helping me navigate various administrative challenges arising from my limited proficiency in the German language. Special thanks are also extended to Dennis Pfeifer for his essential contributions to the design of critical components used in the various tests and investigations conducted for this thesis. I would like to acknowledge Ievgenii Kress for our enlightening conversations and for being the undisputed champion of our room's dart competitions. Karl Heinz Becker's invaluable advice and the intellectual exchange during Friday evening group discussions were essential to my growth as a researcher. Ingrid Scharwächter's assistance in facilitating my integration within the group, managing administrative procedures, and rectifying any inaccuracies in my German forms is deeply appreciated. Last but not least, my sincere thanks to Claudia Höhne, who served as a member of my PhD committee, and to the other members of the RICH working group at Gießen, Jan Otto, Adrian Weber, and Jordan, for their unwavering support throughout this thesis.

I am fortunate and grateful to work at the Astroparticle group at Wuppertal, as my journey would have been incomplete without their extraordinary team spirit and support. The enriching working environment in this group fostered lifelong friendships and countless memorable moments, whether during coffee room discussions, summer events, or Christmas parties. It is a tremendous privilege to have had the opportunity to work with such an exceptional group during this thesis. I extend my deepest appreciation to Eric Mayotte, whose unwavering motivation played a pivotal role in helping me persevere during the most challenging phases. I am also thankful to the other members of the Astro group, including Sven, Ruth, Stephanie, Sonja, Michael, Pia, Alex, Ioana, Leo, Shivani, Pavish, and Fedrick, who provided unwavering motivation and encouragement throughout the journey. ***"It was not possible without you guys, thank you for everything".***

The support for this thesis extends back to India. My sincere thanks to Dr. Tapan Kumar Nayak and Dr. Subhashish Chattopadhyay for their valuable guidance during my stay at VECC. My colleagues there, Rajesh, Arindham, Shaifali and Khsitij, also have their share of contribution to help me get this opportunity. I will also thank all the teachers in my life because of whom I developed an interest in physics in the first place and chose it as a career path. I want to express my deepest gratitude to Lt. Sirish Desai, Dr. Jignesh Pandya, Dr. Arun Anand, Dr. Vipul Kheraj, Dr. A.K. Rai, Dr. Kamlesh Pathak, Dr. Pruthul Desai and Mr. Viresh Thakkar to shape my career. I would also thank my colleagues from SVNIT, some of whom also joined me here in Germany to make this journey even more memorable: Viren, Harsh, Vivek, Gaddu, Akashroop, Dhaval, Aditya, and the most important person among all, Charitarth.

No journey is complete without a contribution from friends and family. They are both motivation and reason for your success. I could not have undertaken this journey without the support of my college gang: Maharshi, Bhavesh, Prabhu, Lt. Sanjay, Chintan, Prem, Jigar and Crocodile. I will also extend my thanks to Bhavin, Vishal, Darshana and most importantly, Biju Joseph. I am incredibly grateful to Akhila, Vandana and Mansi for all the motivation and support over all these

years. I will also thank my friends here in Germany: Karthik, Anitha (I was forced to write her name), Kiki, Pedro, Katerina & Greg played a vital role in being a family away from family.

I would also thank my family, without whose support this journey would not have been possible in the first place. I wish I could have my father Kiritbhai Patel, see me taking a degree, and I wish I could have got this opportunity earlier. I am also grateful to my mother, Gitaben, for her constant support throughout my life. Along with them, I will also like to thank my maternal uncle Rajesh and aunt Pratiksha who brought me up into the individual I am today. I would also like to thank Chiragbhai and Minu Bhabhi, my father-in-law, my mother-in-law and most importantly, my whiskey partner Vijay uncle, for their trust and support.

This gratitude is only completed by mentioning the most special people in my life. Kishore with whom I grew up and has been on my side since my childhood in all my ups and downs. Ajesh Desai, Bhadresh Patel, Daxesh Jariwala, and Jigar Vyas, are the four pillars of my life. Ajesh and Bhadresh I still remember that Diwali night when we went for my passport fomalities and where this journey actually started. Daxesh, I remember you gave me your own jacket when I was coming to the CERN school and Jigar, thank you for all the intellectual conversations where you claim things with over confidence and then fall flat on the face.

Mansi, I extend my heartfelt gratitude to you for consistently reminding me of my strengths and capabilities and for always believing in my potential. You often expressed your desire to see Dr. Vivek Patel, and today, I stand before you as Dr. Vivek Patel.

I could never achieve anything if I had to fight all this alone. It was never possible without you guys.

Lastly, Sweta, thanks for being on my side all these years. Thank you for placing your trust in me and believing in my abilities. Your motivation, hope, and love were the driving force behind the successful completion of this thesis, even during the most challenging moments. Thank you for standing beside me even in the hardest of my time when I was at my lowest.

I dedicate my thesis to all of you.

Declaration of Authorship

English

I hereby declare that the thesis submitted is my own unaided work. All direct or indirect sources used are acknowledged as references.
This thesis was not previously presented to another examination board and has not been published.

Deutsch

Hiermit versichere ich, die vorliegende Arbeit selbstständig und unter ausschließlicher Verwendung der angegebenen Literatur und Hilfsmittel erstellt zu haben.
Die Arbeit wurde bisher in gleicher oder ähnlicher Form keiner anderen Prüfungsbehörde vorgelegt und auch nicht veröffentlicht.

Wuppertal, den _____ _____

(Vivek Patel)